Study of novel gaseous photomultipliers for UV and visible light

Thesis for the degree of Ph. D. in physics
presented to the Scientific Council
of the Weizmann Institute of Science, Rehovot, Israel

by
Dirk Mörmann

Supervisor: Prof. Amos Breskin

5th June 2005

CONTENTS

NOTATIONS

- **APD:** Avalanche Photodiode
- **CB:** Conduction Band
- **CCD:** Charge Coupled Device
- **CFD:** Constant Fraction Discriminator
- **GEM:** Gas Electron Multiplier
- **GPM:** Gas Avalanche Photomultiplier
- **HPD:** Hybrid Photodiode
- **LAAPD:** Large Area Avalanche Photodiode
- **MCA:** Multi-Channel Analyzer
- **MCP:** Microchannel plate
- **MHSP:** Microhole and Strip Plate
- **MICORMEGAS:** Micromesh Gaseous Detector
- **MSGC:** Microstrip Gas Counter
- **MWPC:** Multiwire Proportional Chamber
- **NEA:** Negative Electron Affinity
- **PC:** Photocathode
- **PES:** Photoemission Spectroscopy
- **PET:** Positron Emission Tomography
- **PMT:** Photomultiplier Tube
- **QE:** Quantum Efficiency
- **RICH:** Ring Imaging Cherenkov Detector
- **SiPMT:** Silicon Photomultiplier
- **TAC:** Time-to-Analog converter

- **TEA:** Triethylamine
- **TFA:** Timing Filter Amplifier
- **TMAE:** Tetrakis(dimethylamine)ethylene
- **TPC:** Time Projection Chamber
- **VB:** Valence Band
- **VLPC:** Visible Light Photon Counter
- **WSA:** Wedge and Strip Anode

Part I

INTRODUCTION

1. INTRODUCTION

Progress in science is driven not just by the interplay of theory and experiment, but also by breakthroughs in instrumentation. Only the invention and continuous improvement of specialized sensing instrumentation allows us to record and study processes in nature that would lay hidden from our limited "natural instruments", like the eye, ear etc.

The discovery of radioactivity by Henry Becquerel with the help of photographic paper initiated the new fields of nuclear and later particle physics. For a long time, photographic methods based on chemical changes in light-sensitive layers were the only method to study radiation processes in nature. They were more and more replaced by detectors recording radiation as electronic pulses, e.g. Geiger-Müller counters, proportional counters and photomultipliers coupled to scintillating material, allowing the fast accumulation of huge amounts of data; essential for the study of rare events.

Detection of low intensity light down to the single-photon levels plays a key role in modern research and applications: chemi- and bioluminescence measurements in biology, particle detection in high energy physics, modern X-ray or Positron Emission Tomography (PET) in medical diagnosis, material and composition analysis in chemistry and engineering and sky observation in astronomy to name just a few.

In these fields there is a growing demand for photodetectors covering large areas with position-resolved fast detection of low light levels at moderate cost. Vacuum devices like photomultipliers tubes (PMTs) have the required sensitivity to low light levels over a wide spectral range. They are robust and are successfully employed for photon detection since decades and will continue to play an important role in light detection. But they are often lacking the required position sensitivity and are rather bulky when large area coverage is demanded due to their operation in vacuum[1]. Furthermore, operation in magnetic fields is restricted, making some of their application in particle physics experiments or in medical diagnosis instruments difficult, where high magnetic fields are encountered.

Semiconductor devices like the Charge Coupled Device (CCD), Avalanche Photodiode (APD) etc., are of growing importance and are already replacing PMTs in many fields. They exhibit superior QE, are compact, provide position resolved measurements and are insensitive to magnetic fields. Their main drawback is the lacking sensitivity to very low light levels due to their limited charge amplification. Furthermore their small size restricts their use to experiments where only a small sensitive area is demanded.

Gas avalanche photomultipliers (GPMs) are successfully employed in high energy physics experiments but might find applications also in other fields as they exhibit many attractive features: Large area coverage ($\sim \mathrm{m}^2$) with flat geometry, insensitivity to magnetic fields, fast response (< 1 ns) and position resolved photon detection makes them a notable alternative

[1] E.g. the spherical ∅50 cm PMTs of Hamamatsu of the Super-Kamiokande experiment [1]

to vacuum or semiconductor photosensors. So far, their spectral sensitivity has been limited to the UV range, where most applications are in the detection of Cherenkov radiation [2, 3]. This marks also their main drawback, as most applications require sensitivity to visible light. In addition, current GPMs operate under gas flow, requiring a continuous gas supply, which makes their application considerably more intricate compared to vacuum or semiconductor photosensors.

Gas Avalanche Photomultipliers exhibiting an extended sensitivity towards the visible spectral range and sealed in a gas environment would therefore constitute a breakthrough in the field and could become an invaluable tool for research and applications in many fields. This thesis research makes an important contribution towards this goal, investigating the physical processes in gas avalanche detectors. GPMs based on the Gas Electron Multipliers [4] were found to overcome the limitations of classical, wire-based GPMs: they strongly suppress secondary process on the photocathode originating from the gas amplification and allow to easily reach gains of 10^6. In the course of this thesis work the first GPM sensitive to single photons in the visible range was realized and successfully operated. Furthermore it was demonstrated that such a device can provide for position resolved single photon counting with sub-millimeter localization accuracy.

1.1 Goals and scope of the work

The goal of this research was to conceive advanced gaseous imaging photomultipliers (GPMs), combining thin-film photocathodes, sensitive in the UV- and visible-spectral range, with fast gas avalanche multipliers sensitive to single charges. This required extensive research of numerous physical processes involved, e.g. photoemission into gas, electron and ion transport, avalanche processes in cascaded multipliers, ion-induced process at the photocathode surface and their reduction, charge localization processes etc.

Therefore the following phenomena were studied in detail:

- **Emission of photoelectrons into gas:** Photoelectrons emitted from the photocathode into the gas media undergo elastic collisions with gas molecules and may backscatter to the photocathode. The loss of photoelectrons, implying a reduced photon detection efficiency, can be considerably reduced by a proper choice of the gas mixture, the electric field conditions at the photocathode surface and the detector geometry (Chapter 4).
- **Electron collection:** Photoelectrons have to be efficiently collected into the multiplying stage of the detector in order to be recorded. This required the study and optimization of the gas mixtures as well as the detector geometry and the electric field configurations (Chapter 4).
- **Limitations of the avalanche multiplication:** Contrary to detectors based on gas ionization, where the gain limitation is due to sparks at certain "weak points" of high field, in the GPMs secondary effects on the photocathode strongly limit the achievable electron multiplication factors as well as localization and time resolutions in gaseous detectors. Especially photon- and ion-feedback effects induce these limitations

and therefore required a detailed study. The physics of ion neutralization on the photocathode surface had to be understood and ways of reducing these limitations had to be found (Chapters 5 and 7).

- **Charge transport in cascaded electron multipliers:** The study of both ion and electron transport through the stages of the detector had to be studied and understood, in order to improve the overall detector performance (Chapters 4 and 6).

- **Charge localization and timing:** The study of the localization and timing properties of these detectors involves the understanding of the processes governing the charge transport and charge spread in the detector. Ways of coupling a readout structure to the GPM and efficiently transferring the charge signals to it had to be investigated (Chapters 4 and 9).

- **Preparation of visible-light-sensitive photocathodes:** The production and characterization of photocathodes sensitive to the visible spectral range in ultra high vacuum conditions had to be mastered and improved. High quantum efficiency photocathodes, stable for extended periods of time in their production environment had to be produced in order to later couple them with gas-operated electron multiplier structures in sealed devices (Chapter 3).

- **Sealed GPMs:** Due to their high chemical instability, accompanied by a loss in sensitivity, visible light sensitive photocathodes need to be sealed to an electron multiplier inside a hermetically closed package. The required sealing technology had to be mastered, with the additional challenge of retaining the sensitivity of the photocathode and the functionality of the electron multiplier (Appendix B).

2. SCIENTIFIC BACKGROUND

2.1 Photoeffect and photoemission

Different methods of photon detection exist, but they all have in common that incident photons are converted into electrons via the *photoeffect*, which are subsequently recorded. In 1921 Einstein received the Nobel Prize for the discovery of the law of the photo-electric effect. His explanation of photoemission of electrons from metallic surfaces is considered to be one of the first proofs of the quantized nature of light. The kinetic energy of photoemitted electrons depends on the wavelength of the incident photon according to the following formula:

$$E_{kin} = h\nu - E_{pe}\,, \tag{2.1}$$

where E_{kin} is the kinetic energy of the emitted electron, $h\nu$ the energy of the incoming photon and E_{pe} the photoemission threshold of the material, e.g. the work function in metals and the sum of band gap and electron affinity in semiconductors. Therefore, only photons with energy $h\nu$ exceeding the threshold energy E_{pe} can induce photoemission.

The number of emitted electrons is proportional to the number of incident photons; the average number of photoelectrons released per incident photon is designated the photoemissive material's *Quantum Efficiency* (QE). It depends on the properties of the irradiated material and on the energy or wavelength of the incident photons. To explain the observed variation in QE for different materials by several orders of magnitude, it is useful to consider photoemission as a process involving three steps [5]: (1) absorption of a photon resulting in the transfer of energy from photon to electron, (2) motion of the electron towards the material-vacuum interface, and (3) escape of the electron over the potential barrier at the surface into the vacuum. This allows to relate the photoemission characteristics of a material to parameters of the emitter, such as the optical absorption coefficient, electron scattering mechanisms in the bulk and the height of the potential barrier at the surface [6].

Energy losses occur in each of these steps. In the first step, only the absorbed portion of the incident light is effective and thus losses by light transmission and reflection reduce the quantum efficiency. In the second step, the photoelectrons may lose energy by collision with other electrons (electron scattering) or with the lattice (phonon scattering). In the last step, the potential barrier at the surface prevents the escape of some electrons.

Metals do not constitute efficient photoemitters: firstly metallic surfaces have a high reflectivity for photons and secondly excited electrons in the bulk rapidly lose there kinetic energy in collisions with the large number of free electrons in the metal through electron–electron scattering. All photoemitters of practical importance are semiconductors: they have high photon absorption probability and the kinetic energy loss of electrons on their motion

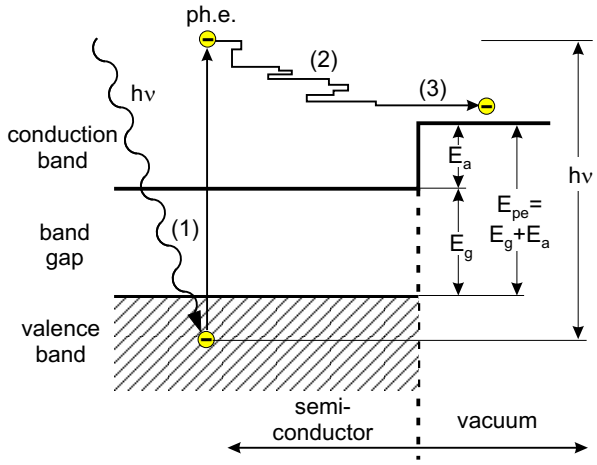

Fig. 2.1: Simplified semiconductor energy-band model and the three step model of photoemission: (1) absorption of a photon and creation of an electron-hole pair, (2) the electron motion to the surface and (3) its escape into vacuum.

is minimal, particularly if their energy is smaller than the band-gap energy. A simplified semiconductor energy-band model in Fig. 2.1 illustrates the process.

In a semiconductor an absorbed photon creates an electron-hole pair and excites the electron from the valence band (VB) to the conduction band (CB). The electron moves randomly in the conduction band and loses energy in the process. It has a relatively long range of motion as energy losses in semiconductors are dominated by electron–phonon scattering. Electron–electron scattering with considerably higher energy loss per event is strongly suppressed in semiconductors due to the small number of electrons in the conduction band. A photoelectron eventually arriving at the semiconductor surface is emitted into vacuum if it retained sufficient energy to overcome the potential barrier, the *electron affinity* E_a, of the semiconductor. The average distance an excited electron can travel inside the semiconductor and still overcome the potential barrier is designated the *photoelectron escape length*.

A photon can generate an electron-hole pair if its energy $h\nu$ exceeds the band-gap energy E_g. Under this condition photo-conductivity (or *internal photoeffect*) in the semiconductor is achieved. If the photon energy $h\nu$ is larger then the photoemission threshold E_{pe},

$$E_{pe} = E_g + E_a \tag{2.2}$$

namely the sum of gap energy and the electron affinity, photoelectron emission into vacuum (or *external photoeffect*) can occur.

Thermal excitation of electron-hole pairs is the source of substantial dark currents in semiconductor photon detectors, especially if they are based on the internal photoeffect. But due to the higher energy required for electron emission, the probability for *thermionic emission* is considerably smaller. It can be neglected in most applications, although it constitutes a constant background of single electrons in photon detectors with solid photocathodes and can be substantial for some photoemitters at elevated temperatures (Fig. 2.2). In addition it is known that the quality of the photocathode surface can change the thermionic emission properties by more than two orders of magnitude [6].

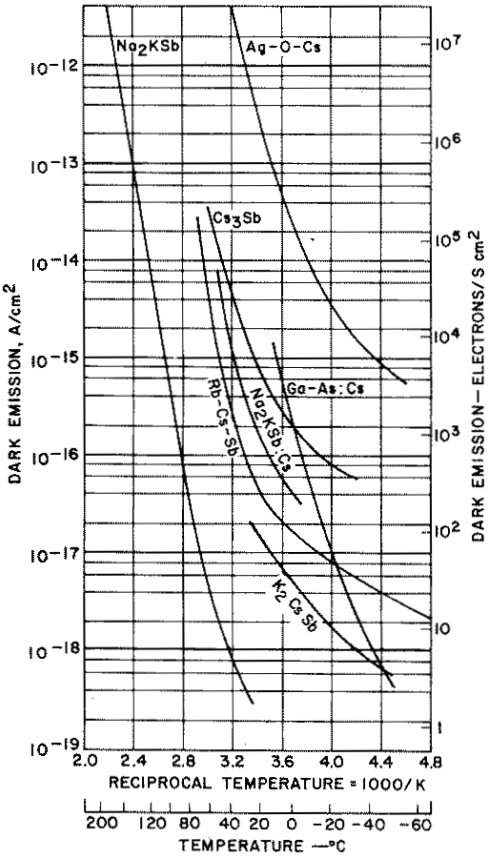

Fig. 2.2: Thermionic emission current as a function of temperature for common photocathodes in PMTs (from [7]).

2.2 Photocathodes

Photoemission is a property of all solids and is indeed utilized as an important scientific tool for identification and characterization of materials: by the photoemission spectroscopy (PES) [8]. Practical photoemitters, or *photocathodes* (PCs), exhibit high QE (typically 10 – 40%) in the desired spectral range. QE values of some common photocathodes as a function of wavelength are given in Fig. 2.3. A good and thorough discussion on photocathode theory and on most common practical photoemitters can be found in [6].

2.2.1 Reflective and semi-transparent photocathodes

One distinguishes *reflective* (or opaque) from *semi-transparent* (or transmissive) photocathodes according to their mode of operation. In reflective photocathodes light is incident on a thick photoemissive film and the electrons are emitted backwards (Fig. 2.4a). In semi-transparent photocathodes the photoemissive material is deposited on a transparent medium and the electrons are emitted forwards (Fig. 2.4b).

Because of the limited escape length of photoelectrons, the thickness of the semi-transparent photocathode film is critical. If the film is too thick, most of the photons are absorbed at a distance from the vacuum interface greater than the escape length of the photoelectrons; if

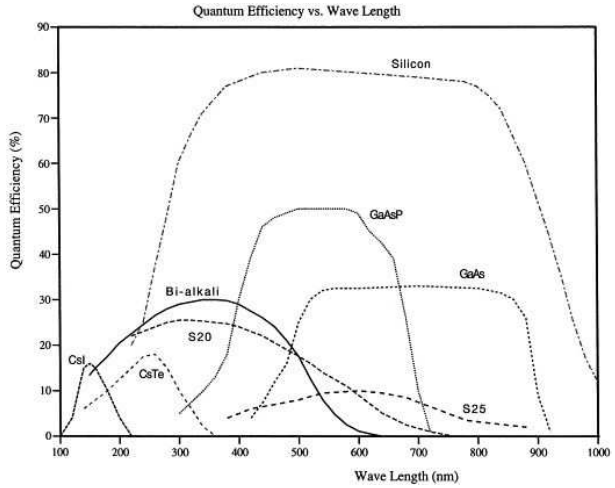

Fig. 2.3: Absolute QE spectra of several commercially available photocathodes in the UV- to visible spectral range. The efficiency of silicon devices is given for comparison. S20 and bi-alkali stands for Na_2KSb and K–Cs–Sb respectively (from [9]).

the film is too thin, much of the incident light is lost by transmission [10, 11]. The production of semi-transparent photocathodes with optimal thickness is rather complex, furthermore the optimal thickness depends on the photon wavelength. Reflective photocathodes exhibit higher QE over a wider spectral range than semi-transparent photocathodes and are simpler to manufacture. Unfortunately, the coupling of reflective photocathodes of large area to electron multipliers is more difficult.

2.2.2 Negative Electron Affinity (NEA) photocathodes

By a deliberate modification of the semiconductor band-structure the electron affinity E_a can be reduced; moreover photocathodes having the vacuum level below the conduction band minimum can be manufactured, exhibiting negative electron affinity (NEA) [5, 12]. NEA photocathodes for the visible spectral range are obtained, for example, by covering a heavily p-doped semiconductor with a thin layer of CsO having a strong dipole moment and low electron affinity. The p-doping of the bulk in combination with the surface dipole causes strong band-bending at the interface, pulling the vacuum level below the conduction band minimum (Fig. 2.5). The photoemission threshold of NEA photocathodes is determined by the band-gap energy $E_g = E_{pe}$ only. Photoexcited electrons in the bulk lose their energy in electron-phonon scattering processes and travel ∼100 Å until they reach the conduction band minimum. Electrons in the conduction band minimum can no longer lose small amounts of energy in electron-phonon interactions due to a lack of energetic states in the band gap. They continue to stay in the conduction band minimum for a long time and typically travel 10,000 Å before recombining with a hole. In *standard* photocathodes the positive electron affinity prevents electrons in the conduction band minimum to contribute to the photoemission. In NEA affinity photocathodes these electrons do contribute to the photoemission and high QE values (exceeding 50%) over a broad spectral range are observed. NEA is reported for many semiconductors, in particular III–V semiconductors (GaAs-CsO) are widely used and commercially available [9, 13, 14, 15]. Furthermore, in ternary compounds, such as

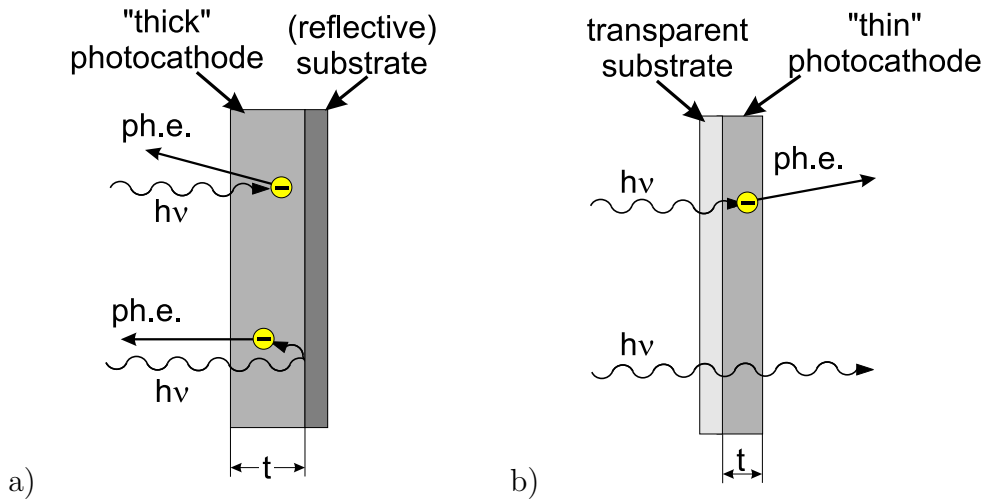

Fig. 2.4: Schematic illustration of a) reflective and b) semi-transparent photocathodes.

GaAsP, the band-gap may be tailored by varying the material composition, thus tuning the sensitivity range of the photocathode to the requirements [15, 16].

Unfortunately, the fabrication of NEA photocathodes for the visible spectral range is difficult and complex, involving the epitaxial deposition of several layers of single crystal semiconductors. They retain their properties only in ultra high vacuum conditions, restricting their use to small areas in well controlled and ultra-clean environments.

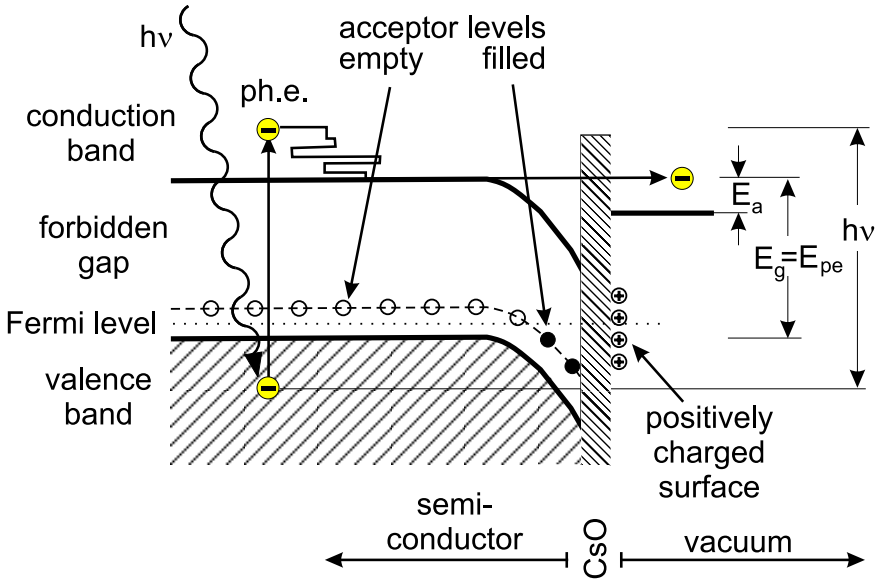

Fig. 2.5: Simplified semiconductor energy-band model showing negative electron affinity.

2.2.3 Photocathodes employed in the thesis work

CsI photocathodes

CsI photocathodes [17] are efficient photoemitters in the VUV range, limited in the short wavelength sensitivity by the transmission of the optical window and having a cut off at light around 210 nm ($E_{pe} \cong 6$ eV). They are *solar-blind*, as they do not respond to the visible. CsI has the largest QE of all alkali halides ($\sim$40% at 150 nm), due to its low electron affinity of E_a=0.1 – 0.2 eV and exceptionally large electron escape length [10, 11].

CsI films are easily prepared by thermal vacuum-evaporation and they are stable when stored in most dry gases. They are not chemically reactive and they are only slightly hygroscopic to they can even withstand short time ($\sim$ minutes) exposures to ambient air [18]. The relatively low resistivity of 10^{10}–10^{11} $\Omega \cdot m$ [3] allows their operation at high photon fluxes.

CsI photocathodes are employed in vacuum photodetectors and are commonly used in large-area (square meters) gaseous UV-sensitive wire-chamber based GPMs for Cherenkov light imaging [17, 19, 20, 21]. These detectors are discussed in Sec. 2.5.

Bi-alkali (K–Cs–Sb) photocathodes

Alkali-antimonide PCs, in particular K–Cs–Sb are widely employed in commercial vacuum-photomultipliers; they are also used in currently developed Vacuum-HPDs[1] [22]. Typical QE values of $\sim$ 30% [23] for reflective and 26% at 350 nm [24] for semi-transparent laboratory produced K–Cs–Sb photocathodes are reported, with a spectral sensitivity extending up to $\sim$ 600 nm. They have a band gap of E_g=1.0 eV and an electron affinity of E_a= 1.1 eV [6].

K–Cs–Sb photocathodes are relatively easy to produce by vacuum evaporation of an Sb film and its activation with alkali metals [23]. However, they are extremely chemically reactive and decay promptly upon few minutes exposure to $\sim 10^{-5}$ torr of oxygen and moisture [25]. Therefore, detectors comprising alkali-antimonide photocathodes must operate in a sealed-mode with multipliers made of ultra-pure materials and preferably with a getter installed inside the detector housing. Although the PCs maintain their QE in ultra pure gases [26], previous attempts to operate such PCs under gas multiplication [27, 28] were not pursued, due to strong photon- and ion-feedback effects and decay of the photocathodes' QE.

A possible way to prevent the alkali-antimonides' chemical degradation in gas is to coat them with a protective film [29]; the latter should be thin enough to allow photoelectron emission (high QE) but thick enough to prevent contact between the gas molecules and the PC. Intensive research of adequate protective materials for Cs_3Sb and K–Cs–Sb PCs, coating conditions, electron transport properties, sensitivity to impurities, degradation under photon and ion flux, etc. has yielded very satisfactory results of protection against oxygen [30, 31, 32, 25, 33]. The coating film is selected from materials having good electron transport properties, i.e. large band-gap materials, and small electron affinity. Unfortunately, these coating layers did not provide protection against moisture and they reduce the QE typically by a factor 5–7.

[1] Hybrid Photodiodes, see Sec. 2.4.2

2.3 General considerations for photodetectors

As discussed above, in all photodetectors photons are converted into electrons that are subsequently recorded as a signal in the attached electronic circuit. Single or even few electrons do not constitute a sufficient charge for detection at room temperature, as the attached electronic devices always suffer from thermal noise. Therefore, either a large number of photoelectrons is integrated over a time period in *charge integrating mode* or an electron multiplication process is creating a large enough signal, enabling fast detection of single or few photoelectrons in *pulse-counting mode*.

The fast detection of a small number of photons in pulse counting devices can be subdivided in three steps:

1. Conversion of a photon into an electron
2. Electron multiplication
3. Recording and processing of the multiplied charge

In this work the fast detection of very low light levels in the UV- to visible spectral range with gaseous photomultipliers based on cascaded Gas Electron Multiplier (GEM) [4] foils was investigated. The following sections provide an overview of alternative photon detection methods as well as reviewing the current status of gas avalanche photodetectors.

2.4 Photodetectors other than gas avalanche photomultipliers

2.4.1 Solid state devices

All solid-state photon detectors utilize the internal photoeffect for photon detection. Due to the low energies required to create an electron-hole pair (e.g. E_g=1.1 eV in Si) and the high photon absorption, solid state photon detectors exhibit QE values approaching 100% over a broad spectral range (Fig. 2.3). Additional advantageous features are robustness, excellent energy resolution and insensitivity to magnetic fields. As drawbacks can be considered their limited size and relatively high temperature dependent dark currents.

Photodiodes

In photodiodes electron-hole pairs are created by incident radiation in a depleted p-n-junction. An applied reverse electric field quickly separates the charge carriers and a fast current pulse is recorded on the attached electronic circuit. The p-n diodes deficiencies are related to the small depletion area (active detection area); many electron-hole pairs recombine before they can create a current in the external circuit. In the *PIN photodiode*, the depleted region is made as large as possible by separating the heavily doped p- and n-types by a lightly doped intrinsic layer. PIN photodiodes are used in a wide range of applications with medium to high light intensities, e.g. in precision hadron calorimeters [34, 35] or in fibre-optics readout. Lacking an internal multiplication process, photodiodes are not suited for low light level applications.

Charge Coupled Devices (CCD)

Charge Coupled Devices (CCDs) consist of a one- or two-dimensional array of potential wells in a silicon bulk. Each potential well, typically 10-15 μm in square, accumulates the photoelectrons created by light illumination. After a fixed integration time, the charge of each pixel is sequentially moved from one well to the adjacent one and finally to an attached amplifier by adjusting the voltages applied to each pixel. CCDs are *integrating devices* and do not have an internal photoelectron amplification mechanism. They exhibit a wide spectral sensitivity with high QE characteristic for silicon devices (Fig. 2.3).

CCDs are mostly used as image sensors for video-cameras, scanners or digital photo-cameras and play an important role in modern astronomy as well as direct soft X-ray imaging. They exhibit excellent 2D-imaging capabilities and are relatively inexpensive as they are mass-produced. Due to the sequential charge readout procedure, CCDs are relatively slow devices with a frame rate of typically a few 100 Hz. Recently, very specialized high speed CCDs providing frame rates of up to 4 MHz became commercially available [36]. Among the disadvantages is the noise accumulated with the image.

Avalanche Photodiodes (APD)

Avalanche Photodiodes (APDs) combine the high QE of PIN photodiodes (80% at the 300–800 nm range) with the additional benefit of internal amplification. An elaborate doping configuration in APDs creates a thick, low electric field region for photoconversion, followed by a thin, high field p-n-junction [37]. Incident photons create electron-hole-pairs in the conversion region and the electrons are subsequently accelerated in the high field p-n-region to energies sufficient to create more electron-hole pairs. Gains of up to 10^4 can be achieved, adequate for many applications. APDs are already replacing photomultipliers in some fields, for example for scintillating fibre [38, 39] and electromagnetic calorimeter readout [40]. Due to their high QE and gain uniformity, they perform very well in X-ray and gamma spectroscopy for a wide range of energies [41] and the fast signal creation in APDs (610 ps FWHM time resolution) makes them candidates for time-of-flight measurements [42]. Large Area Avalanche Photodiodes (LAAPD) were recently introduced[2] with a sensitive area up to $\sim$2 cm^2 at the expense of higher noise. APD arrays of a few tens of pixels and an total active area of $\sim$1 cm^2 are commercially available since a few years [43] and are expected to replace traditional PMTs in modern positron emission tomographs (PET) in combination with LSO scintillators [44].

Due to their limited gain and size, APDs cannot be employed for single photon detection or at large area.

Visible Light Photon Counter (VLPC)

In contrast to standard avalanche photodiodes, carrier multiplication in VLPCs [45, 46, 47] takes place across a band gap of only 50 meV, thus reducing gain dispersion considerably. Therefore, VLPCs exhibit the best known energy resolution in the visible light range. The

[2] Advanced Photonics Inc., USA

small gap is due to an impurity band 50 meV below the conduction band, created by a high donor concentration ($\sim 10^{17}$ cm^3) and low counter-doping in the p-layer of the diode.

A photon creates an electron-hole pair across the standard valence-to-conduction band gap in the intrinsic (non-doped) zone. The hole drifts through the high field depletion region and into the impurity band p-zone. Upon collision with a neutral donor, it frees an electron which starts the electron avalanche by impact ionization on neutral donor impurities. Due to space charge effects the avalanche process is self-limiting, and the gain saturates at a few 10^4. VLPCs exhibit high QE of the order of 80% and offer excellent single photon counting capability at high rates (∼100 MHz on a 1 mm diameter device [48]). They are currently massively employed for the readout of scintillating fibres in the D0 experiment at Fermilab [49]. Due to the very small impurity band gap, VLPCs need to operate at liquid helium temperatures to eliminate thermal noise and their size is limited to a few millimeters in diameter.

Silicon Photomultipliers (SiPM)

The Silicon Photomultiplier (SiPM), is a rather new device described in detail in [50]. It is a multi-pixel silicon photodiode with micro-pixels (10^3/mm^2) positioned on a common Si substrate, electronically decoupled from each other. A bias voltage 10–15% higher than the breakdown voltage is applied, and each SiPM pixel operates in Geiger mode, limited by an individual resistor and a gain determined by the charge accumulated in the pixel capacitor. SiPMs operate at room temperature considerably more stable than standard APDs and have single-photoelectron gain (10^6) and photon detection efficiency (20%) similar to vacuum PMTs. Due to their high gain, SiPM have a very good signal-to-noise ratio and are suitable for photon counting [51]. They are intrinsically very fast due to the small depletion region and the extremely short Geiger-type discharge; time resolutions of ∼120 ps FWHM were obtained with single photoelectrons [51], superior to the best vacuum PMT results.

Their main drawbacks are their limited size (∼1 mm^2), high cost and low QE, when compared with other semiconductor devices. They are not yet commercially available.

2.4.2 Vacuum devices

Vacuum photodetectors utilize the external photoeffect in photocathodes for photoconversion. As was discussed above, the QE of common photocathodes is limited to $\sim 30 - 40\%$. Photoelectron amplification is achieved by accelerating them in vacuum to high kinetic energies, resulting in the generation of secondary electrons on series of dynodes or within semiconductors.

Photomultiplier tubes (PMTs)

Photomultiplier tubes (PMT) are still the most common and versatile photon detectors, existing in a wide variety of designs and spectral sensitivities. Having high gains exceeding 10^7, they allow for reliable photon detection down to the single-photon level over a wide spectral range, from the UV to the IR. They exhibit a wide dynamic range with often a very

fast response and low noise and are commercially available. The operation in vacuum limits their size; e.g. PMTs reaching 50 cm diameter [1] are very bulky and their performance suffers in environment with magnetic fields. New, compact PMTs were developed in recent years having thin-mesh dynodes and are able to operate in magnetic fields of up to 1.5 T [52]. Furthermore, position sensitive and pixelized PMTs are now supplied by several companies with pixel sizes down to 2×2 mm^2, but they suffer from limited area and high cost. High-speed photomultipliers utilizing microchannel plates (MCPs) as electron multipliers in proximity with the photocathode and anode are also available [53]; they have rise times of ∼200 ps with single-photon sensitivity; they are available as 2×2 inch flat panel elements with segmented anodes (64 pixels) [54]. A problem in using them to cover large areas is the dead area in the contact edges, which can be as high as 50% of the array.

Hybrid Photodiodes (HPD)

Hybrid Photodiodes (HPDs) [55] combine in a single vacuum-operated device a photocathode and a solid-state sensor. Photoelectrons released from the photocathode are accelerated by an applied high voltage of 10–20 kV onto a solid-state detector. The kinetic energy of the photoelectron is converted into a few thousands electron-hole pairs in the sensor which are recorded as a signal in the attached electronics. The QE of the device is dictated by the photocathode, and is thus similar to conventional photomultipliers. The photoelectrons released by the incident light are either proximity imaged onto the silicon detector or focused by electron optics, achieving a demagnification of the photon image and allow thus for large area coverage. Unfortunately the electron optics is susceptible to image distortions which limit the achievable demagnification factors.

Segmentation of the solid state device, e.g. a segmented photodiode, results in a uniform position-sensitive device without dead regions. HPDs exhibit excellent single electron detection suitable for photon counting [24, 56] and they are able to operate in axial magnetic fields up to 1.5 T [57]. A large area, 25 cm diameter HPD is currently under development for Cherenkov imaging in cosmic ray astronomy [58].

Commercially available HPDs employing APDs instead of photodiodes, reach gains of 6–$8{\cdot}10^4$ and allow for operation at high counting rates using fast, low gain electronics [14]. However their size is currently limited to less than 1 cm in diameter.

2.5 Gas Avalanche Photomultipliers (GPMs)

Gas Avalanche Photomultipliers rely on photoelectron multiplication in gas. Subsequent to photon absorption in a gaseous or solid photocathode [2], the photoelectron is guided into a region of strong electric field. There, photoelectrons acquire high kinetic energies and liberate additional electrons by impact ionization of the gas molecules. This multiplication process, called *Townsend avalanche* [12], results in an exponentially growing number of electrons with the length of the multiplication region. The multiplied electrons are collected on an anode for subsequent pulse processing.

The photon detection efficiency of GPMs depends both on the photocathode's QE and on the single electron detection efficiency. After emission, the photoelectron has to be ex-

tracted from the vicinity of the photocathode and losses due to photoelectron backscattering (Sec. 2.6.1) might occur. Subsequently the photoelectron has to be collected in to the gas electron multiplier which has a single electron detection efficiency ϵ_{det}. The single photon detection efficiency ϵ_{photon} of GPMs can thus be described as

$$\begin{aligned} \epsilon_{photon} &= QE_{eff} \cdot \epsilon_{det} \\ &= QE \cdot \epsilon_{extr} \cdot \epsilon_{det} \,, \end{aligned} \tag{2.3}$$

with ϵ_{extr} the photoelectron extraction efficiency (see Sec. 2.6.1). Besides the photocathode's intrinsic quantum efficiency QE, ϵ_{det} depends on the choice of the counting gas, detector geometry, amplification factor and readout electronics.

Gaseous electron multipliers achieve amplification factors in excess of 10^6 and are an indispensable tool not only for light detection but in all fields where the detection of ionizing radiation is requested. The field of gas electron multiplication was dominated by wire-based detectors[3], achieving electron multiplication in the high electric field regions around thin anode wires. More recently micro-pattern gas detectors are replacing wire based gas detectors [60]; they achieve a considerable improvement of rate capability, position and time resolution by miniaturizing the detector amplification and readout structures using modern photo-lithographic processes.

Employing gas avalanche detectors for photon detection exhibit several advantageous features that are not reached by any other photodetector in this combination: Very high gains guarantees sensitivity to single charges and GPMs are thus suitable for photon counting. Due to the fast pulse generation in modern micro-pattern detectors, excellent time resolution and high rate capability exceeding 100 kHz/mm^2 can be achieved. With highly segmented anodes, sub-millimeter position resolution for single photons and less than 100 μm for multiple photon events are reported. Due to the electron drift in gas, they can operate even in strong magnetic fields. Furthermore, when operated in atmospheric pressure gas, they can be constructed very large ($\sim$m^2) in flat geometry, limited only by the photocathode manufacturing process. This gives them a distinct advantage over semiconductor and vacuum devices: the first are limited to a few cm^2 in size and the second have to withstand atmospheric pressure and thus have to be constructed rather bulky and are not position sensitive when large area coverage is requested.

The first generation of GPMs consisted of wire chambers filled with photosensitive gas for photoconversion [61, 2]. They were developed for large area Ring Imaging Cherenkov detectors, proved to be an important tool for particle identification in high energy physics and employed in many experiments [2]. Vapours like tetrakis(dimethylamine)ethylene (TMAE) or triethylamine (TEA) [2] added to a regular gas mixture and flushed through the detector volume represented the only choice of photo-converters sensitive in the UV region until a decade ago; TMAE being the most efficient photo-converter with a mean ionization potential of 5.4 eV and a QE reaching 40% at 170 nm. However, its operation is very intricate, requiring elevated temperatures due to their low vapour pressure and careful choice of detector construction materials to avoid chemical reaction with theses aggressive vapours; it is also

[3] see for example [59] for a summary of their properties

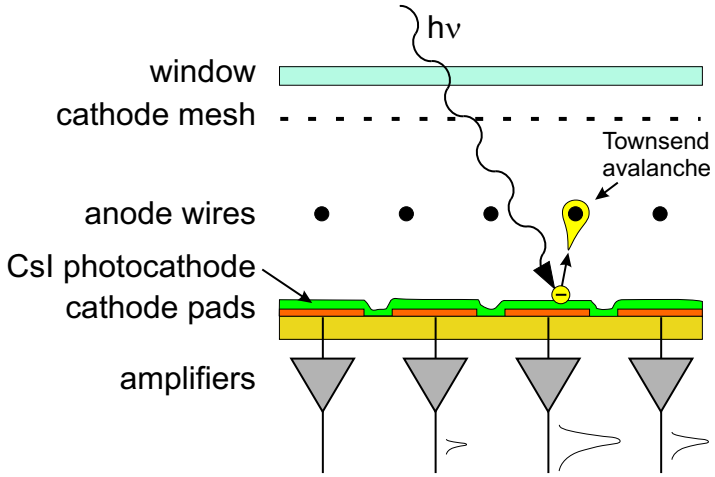

Fig. 2.6: A gas avalanche photomultiplier comprising a solid photocathode and a multiwire proportional detector with a cathode pad readout.

problematic due to detector aging by deposition of molecular fragments on the anode wires [2].

Thin films of CsI solid photo-converters replaced gaseous photocathodes in most experiments employing GPMs in Cherenkov light detection [19, 20, 21]. Albeit exhibiting somewhat lower QE than TMAE, photoelectrons from CsI photocathodes are emitted isochronously into the gas and are proximity focused onto the electron multiplier, as illustrated schematically in Fig. 2.6. Therefore they do not suffer from parallax and time jitter typically observed in GPMs with gaseous photocathodes having photon conversion regions a few millimeters wide. CsI-based wire-chamber photodetectors currently employed in high energy physics experiments are discussed in Sec. 2.7.1.

2.6 Limiting processes in GPMs

2.6.1 Photoelectron backscattering

Unlike with solid photocathodes operated in vacuum, photoelectrons ejected into gas are subject to scattering processes with gas molecules. Depending on the gas mixture and the electric field strength in the vicinity of the photocathode, photoelectrons can either scatter inelastically (i.e. excitation of the gas molecule) or elastically on the gas molecules. In the latter cases, the photoelectrons retain their kinetic energy and can eventually *backscatter* to the photocathode and reduce the photon detection efficiency considerably. The effective quantum efficiency of a photocathode operated in gas, QE_{eff} compared to the vacuum value QE can be described as

$$QE_{eff} = QE \cdot (1 - \epsilon_{bs}) = QE \cdot \epsilon_{extr} \ , \tag{2.4}$$

with ϵ_{bs} the photoelectron backscattering probability and $\epsilon_{extr} = 1 - \epsilon_{bs}$ the photoelectron extraction probability. It was found that high electric fields close to the photocathode and a

proper choice of the gas mixture, comprising molecular gases with a high inelastic scattering cross-section [62, 63], can reduce photoelectron backscattering and even yield the vacuum QE value ($\epsilon_{extr} = 1$). On the other hand, noble gas mixtures exhibit low extraction efficiencies, as they lack states of low energy excitation and electron scattering at moderate electric field strength is almost exclusively elastic [64]. The extraction probability ϵ_{extr} for some common atmospheric pressure gas mixtures for GPMs as a function of the electric field is shown in Fig. 2.7. An electric field strength of at least 1–2 kV/cm is required to minimize photoelectron backscattering.

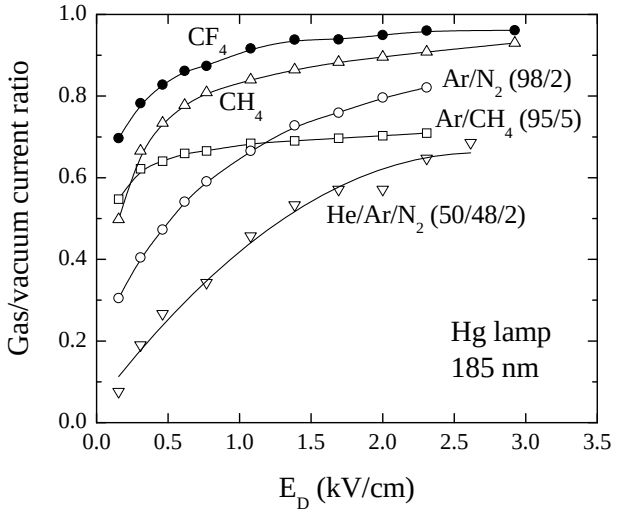

Fig. 2.7: Photoelectron backscattering for common gas mixtures in GPMs at atmospheric pressure as a function of the electric field E_D in the vicinity of the photocathode. The values on the y-axis represent the photoelectron extraction efficiency ϵ_{extr} (from [65]).

2.6.2 Photocathode aging

In vacuum photomultipliers photocathode aging is mainly due to high photon fluxes leading to an exponential decay of its QE with time. This effect of *photon aging* is also reported for photocathodes operated in gas [3, 66]. The dominant decay mechanism of photocathodes operated in gas is however due to avalanche ions impact on the photocathode [66]. It was found that CsI photocathodes may lose as much as 20% of their sensitivity after an accumulated ion charge of $\sim$20 μC/mm^2 [3]. The exact nature of photocathode aging is not completely understood. Obviously ion sputtering causes surface modifications and lattice defects in the photocathode that may reduce the escape length and modify the electron affinity. On the other hand, the authors of [66] report on rejuvenating effects of ion bombardment on photocathodes, while the authors of [67] found a dependence of the photocathode aging not only on the accumulated ion flux to the photocathode but also on the electron temperature in the gas avalanche and the production rate of active molecules.

Despite these yet unexplained observations, it is clear that photocathode aging by ion impact has to be considered and that the avalanche-ions flux, back-flowing from the electron multiplier to the photocathode should be minimal.

2.6.3 Feedback phenomena

Electron multiplication in a gas avalanches generates a large number of ions and photons, which upon impact on various detector elements may liberate *secondary electrons* from there. These secondary electrons initiate new electron avalanches in the detector and more avalanche-generated ions and photons are produced. Thus, several generations of *feedback* pulses, either ion- or photon-induced, may succeed the primary pulse. For events with a large number of primary charges, the *feedback strength*, μ, is defined as ratio of the number of electrons constituting the primary and secondary pulses respectively $\mu = n_{2nd}/n_0$ is given by

$$\mu = \gamma_{ph}(G-1) \tag{2.5}$$
$$\mu = \gamma_{+}(G-1) \tag{2.6}$$

for photon- and ion-feedback respectively, and is proportional to the avalanche gain G with the proportionality constants γ_{ph} and γ_{+}, depending on the gas mixture, pressure, detector geometry and materials. If n_0 primary electrons initiated the first avalanche, the second generation begins with $n_{2nd} = n_0 \cdot \mu$ electrons. Obviously, if the number of secondary electrons exceeds the number of primary ones ($\mu > 1$) the pulse height of the feedback will incessantly increase and ultimately result in a discharge and detector breakdown. Thus the maximum gain G_{max} of a GPM limited by feedback ($\mu = 1$) is given by

$$G_{max} = \frac{1}{\gamma} + 1 \ . \tag{2.7}$$

For the case of few or single primary charges, statistical considerations become dominant and the feedback strength μ has to be considered as the *probability* that a single avalanche ion or photon liberates a secondary electron.

Gain limitations from avalanche-generated feedback processes are well known and studied for gas detectors applied in ionizing particle detection [68] but feedback effects are much more significant in GPMs and can constrain their operation considerably. The low electron-emission threshold of photocathodes result in γ-values that are rather high and limit the achievable gain G_{max} accordingly (Eq. 2.7). Therefore, a careful consideration of feedback effects is mandatory when devising gaseous photomultipliers.

Fig. 2.8 illustrates the time structure of feedback pulses. The generation interval T_g, after which the succeeding avalanche starts, is characteristic for the type of feedback. If photon feedback to a photocathode is involved, the generation time is given by

$$T_{ph} = \frac{d}{v_{-}} \ , \tag{2.8}$$

namely the drift time of the secondary electrons (drifting with a velocity v_{-}) from the cathode to the multiplication site, separated by a distance d. For ion-feedback, the generation time is equal to the drift time of the ions (drifting with a velocity v_{+}) from the avalanche site to the cathode according to

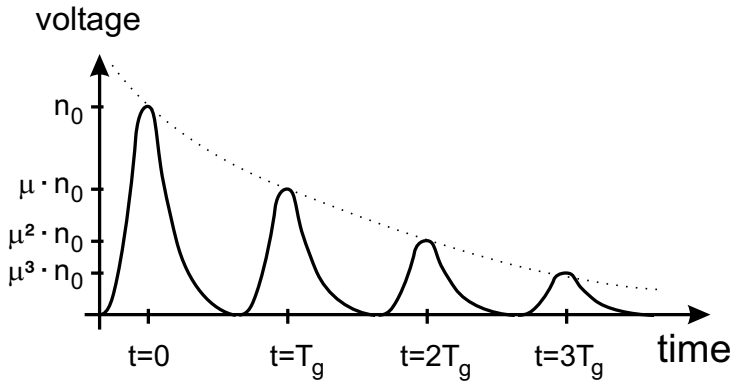

Fig. 2.8: Schematic illustration of a feedback process with $\mu < 1$ and a generation time interval T_g.

$$T_+ = \frac{d}{v_+} \, . \tag{2.9}$$

The drift time of the secondary electrons is much shorter and can be neglected in this case. The generation times differ by a factor 10^2 – 10^3 for the two processes, according to the ration of drift velocities. It allows discriminating between the two by measuring the generation time. Typical values are $T_{ph} \sim 0.1$ – 1 μs and $T_+ \sim 50$ – 500 μs for ions in atmospheric pressure gases and a drift path of $\sim$1 cm.

A proper design of the geometry and choice of the electric field configuration in a GPM can considerably reduce feedback effects on the photocathode, by blocking the photons or deflecting the ions, and is an important subject of this thesis.

2.7 Electron multipliers for GPMs

In principle, most gaseous detectors can be be filled with a photosensitive gas or coupled to a solid photocathode to form a GPM. But the differences in the electric field geometry and the electron multiplication mechanism defines their adequacies as efficient GPMs.

The following section presents a selection of gas electron multipliers that are operated as GPMs and points out their individual advantages and shortcomings. The Gas Electron Multiplier (GEM) [4] and its properties relevant to this work, are described in more detail.

2.7.1 Multiwire Proportional Chamber (MWPCs)

Multiwire Proportional Chambers (MWPCs) [69] (e.g. CLEO RICH [70]) have been the most extensively employed large area photodetectors in particle physics for Cherenkov light detection [19, 21]. While first large area UV detectors employed photosensitive gases, more modern wire chambers employed CsI photocathodes, e.g. the proximity focusing CsI-RICH detector of ALICE shown in Fig. 2.9 [71]. Photons striking the CsI layer deposited on top of a segmented cathode eject photoelectrons that are subsequently multiplied on the thin anode

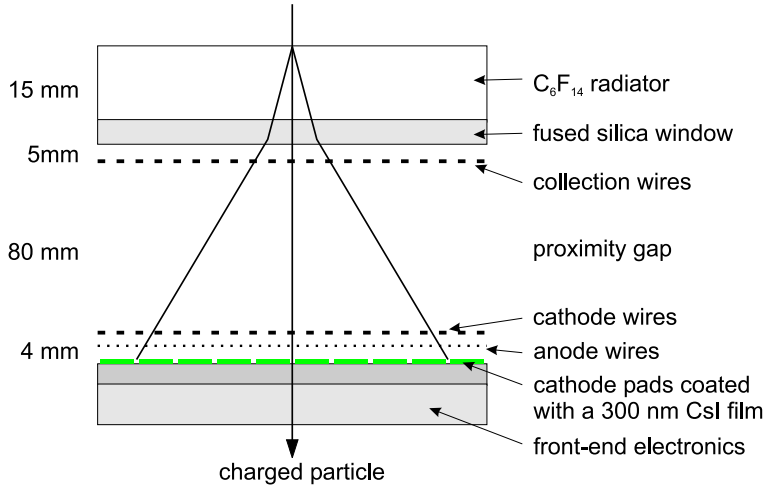

Fig. 2.9: Scheme of the proximity focusing CsI-RICH detector of the ALICE experiment [71].

wires. The large ion cloud generated in the process drifts towards the segmented cathode and induces a signal that provides the photon localization. These GPMs can be made very large ($\sim$ m^2) in flat geometry and are envisaged or successfully employed in many particle physics experiments [72, 21].

Due to their *open geometry*, namely the photocathode is fully exposed to the avalanche photons and ions, MWPC-based GPMs suffer from photon- and ion-feedback and their gain is limited to well below 10^5 [72]. Photon-feedback can be reduced by employing specially designed electrode blinds around the anode wires, but at the cost of an considerably increased complexity of the detector design and fabrication [2]. Most of the avalanche-generated ions are collected at the photocathode and cause ion feedback effects and photocathode aging, limiting the choice of the photocathode to ones with small γ-values and the gas mixture to ones with little average photon emission.

2.7.2 Micromesh Gaseous Detector (MICROMEGAS))

The Micromesh Gaseous Detector (MICROMEGAS) [73] is a miniaturized version of a very asymmetric 2-stage parallel plate detector. The conversion- or drift region of $\sim$3 mm thickness is separated from the narrow ($\sim$100 μm) amplification region by a metallic micromesh. A potential of a few hundred volts is applied across this narrow gap between the mesh and the readout anode, resulting in a very strong electric field in the amplification region. Charged particles traversing the conversion region generate electron-ions pairs and the electrons are guided into the high field region and experience gas multiplication of up to 10^6. Fast signals of $\sim$ ns duration are recorded due to a quick collection of the avalanche electrons and ions in the amplification region. A pixelized anode with high granularity ensures a good position resolution. The rate capability is also very high, characteristic for micro-pattern gas detectors.

Recently, results of MICROMEGAS-based GPMs were presented [74, 75], featuring a reflective CsI photocathode deposited on top of a high opacity (80%) micromesh [76], masking the photocathode from avalanche photons. A time resolution of σ $\sim$700 ps for single electrons

and an excellent single electron detection efficiency is reported. Furthermore, such a detector could be easily made from high purity materials only and would therefore be ideally suited for sealed operation mode. Unfortunately, the very narrow amplification gap requires a high degree of precision in the detector fabrication process and a high rate of discharges between the micromesh and the anode seems to be an immanent weakness of MICROMEGAS [75], constraining its usefulness as an electron multiplier. Furthermore, practically all avalanche ions are impinging on the photocathode with high kinetic energy acquired in the amplification region and enhanced photocathode aging can be expected. The unsuppressed ion flow to the photocathode prohibits the use of MICROMEGAS for visible-light-sensitive GPMs due to the effective ion-induced secondary electron emission (see Sec. 5).

2.7.3 Gas Electron Multiplier (GEM)

The Gas Electron Multiplier (GEM) [4] was initially developed as a *gaseous preamplifier*, preceding other gaseous detectors, like Micro Strip Gas Counter (MSGC) [77] or the Micro-Groove detector [78]. Sharing the amplification between multiple stages was proved to result in stable operation at high gains even when working with a background of heavily ionizing particles [79, 80, 81, 82]. Advances in the GEM manufacturing process resulted in detectors composed solely of GEM elements.

A GEM is made from a thin sheet of insulator (typically 50 μm thick Kapton foil), metal coated on both faces and perforated by a regular matrix of fine apertures (typically 50–70 μm diameter). Placed inside a gas environment and applying a potential difference ΔV_{GEM} of a few hundred volts between the two metal faces, the GEM acts as proportional gas avalanche amplifier: electrons drifting into the GEM holes experience gas amplification sometimes exceeding 10^4 [83] in the strong electric field in the GEM holes (typically 30–100 kV/cm). The multiplied electrons are subsequently extracted from the holes and guided either to a further amplifying element or to a patterned readout anode. Fig. 2.10a illustrates the electric field configuration at the vicinity of a GEM hole, focusing electrons into the holes.

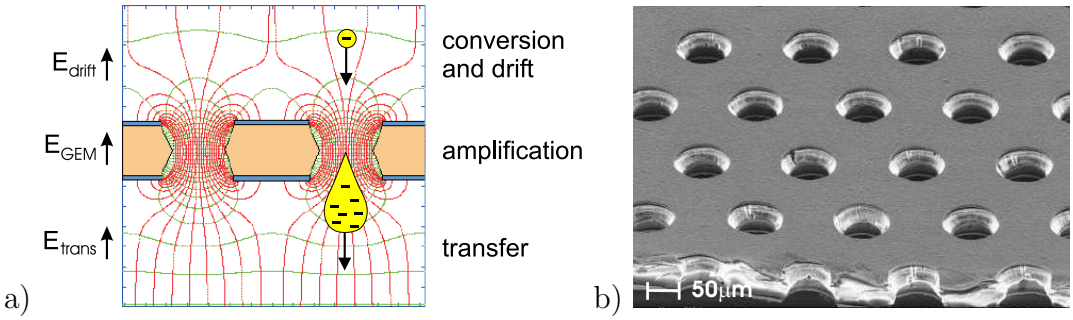

Fig. 2.10: a) Typical field-line configuration in the GEM holes. Electrons are focussed into the apertures where they undergo gas multiplication under high local fields; the multiplied electrons are extracted on the other side. b) Electron microscope photography of a Kapton-made GEM.

Resulting from the manufacturing process, of photo-lithographic structuring of the metallic layers from both sides followed by chemical wet etching of the Kapton material, the GEM holes have a *double-conical* profile, with the narrower diameter d in the hole center.

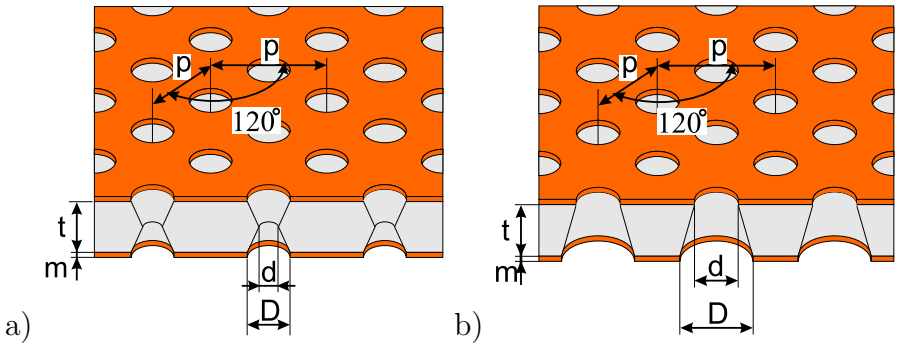

Fig. 2.11: The geometrical parameters of a) double-conical (dc) and b) single-conical (sc) GEMs: pitch p, large hole diameter D, small hole diameter d, insulator thickness t and metal thickness m. The holes are arranged in a hexagonal pattern.

Fig. 2.10b shows an electron microscope view of a 50 μm thick GEM-foil with 70 μm diameter double-conical holes. A simplified fabrication procedure where only one metal side is photo-lithographically structured results in *single-conical* hole shapes [84]. The two GEM types and the parameters defining their geometry are schematically depicted in Fig. 2.11: the pitch or hole-to-hole spacing p, the large hole diameter D, the small hole diameter d, the insulator thickness t and the metal thickness m. Most commonly, the holes are arranged in a hexagonal pattern. The geometries of all GEMs that were used in this work are listed in Tab. 2.1. They were fabricated at CERN[4] and are made from copper-coated Kapton foil with an active area (perforated with holes) of 28×28 mm^2. GEMs used for photocathode deposition (see Sec. 4) have the copper cladding coated with a thin Ni/Au layer to provide for a CsI-compatible substrate. The *photocathode effective area* denotes the area not covered by the holes (e.g. 77% for a *standard GEM* dc140). In the case of single-conical GEMs the side with the narrow holes is used for photocathode deposition.

The different operating properties arising from geometrical variations are discussed in [84] and for the case of single-photoelectron counting in Sec. 4 of this work.

Other GEM manufacturing procedures are reported, like laser drilling [85], plasma etching [80], X-ray lithography [86] and etchable glass technology [87]. These methods allow for

[4] CERN printed circuit workshop

GEM designation	t [μm]	m [μm]	p [μm]	D [μm]	d [μm]	photocathode effective area
dc140	50	5	140	70	50	77%
dc200	50	5	200	70	50	89%
dc100	50	5	140	100	80	53%
sc50	50	5	140	100	70	77%
sc25	25	5	140	110	70	77%

Tab. 2.1: The GEM geometries used in this work. The designations *dc* and *sc* stand for double-conical and single-conical holes respectively. Single-conical GEMs have the photocathode always evaporated on the face with the smaller hole diameter. The *photocathode effective area* is the fraction of the GEM area available for photocathode deposition.

the production of *clean GEMs*, compatible with ultra-high vacuum standards; their production process is more involved and expensive. Recently *thick GEM-like hole multipliers* (THGEM) were investigated [88, 89, 90]; made from 0.4–3mm thick G10 frames with dimensions typically a factor $\sim$20 larger than the ones listed in Tab. 2.1. Excellent performance was observed for these devices in first tests: gains of 10^6 and more in a single THGEM element at atmospheric Ar/CH_4 [91] and 1–10 torr iso-butane [92] and fast pulses with rise time of $\sim$5ns. Thick GEMs have the advantage of being self-supporting, robust devices that can be manufactured at low cost and operated at high gains at wide range of gas pressures.

Operation of multi-GEM detectors

By cascading several GEMs and applying appropriate voltages to the individual elements, a *multi-GEM* detector is formed. In such a configuration, the gas amplification is shared between the separate GEM stages and considerable higher gains and more stable operation can be obtained compared to a single stage device [79, 84]. As separation of the detector's amplification stage from the readout element provides additional protection of the sensitive readout electronics in case of sparks and a high degree of flexibility in the readout electrode design. A schematic illustration of a double-GEM detector consisting of two GEM foils, a drift cathode and a readout anode, is shown in Fig. 2.12. It provides also the designation for the various detector electrodes and electric fields and indicates typical dimensions.

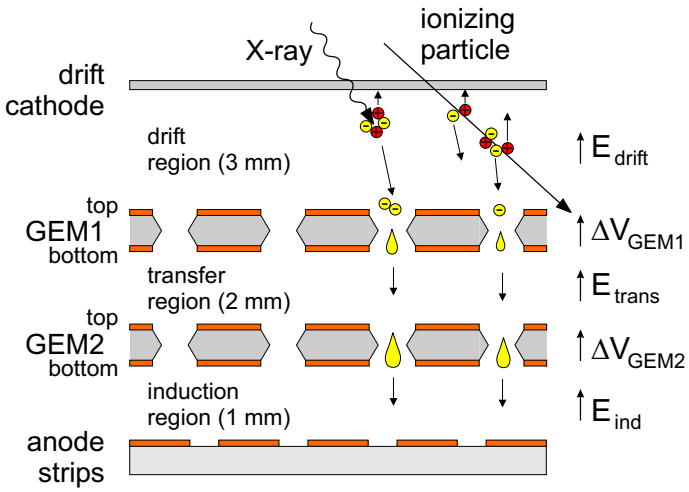

Fig. 2.12: Schematic illustration of a double-GEM detector for the detection of X-rays and ionizing particles consisting of two GEMs, an anode and a drift cathode. The gas gain is shared between the two GEM stages.

For ionizing radiation detection, the drift cathode and GEM1 delimit the sensitive volume of the detector, the *conversion* or *drift region*, where ionizing radiation is absorbed in the counting gas and primary electrons are created. The drift field E_{drift}, defined by the potential difference between the cathode and the top electrode of GEM1, guides the primary electrons towards GEM1, where the strong dipole field (Fig. 2.10a) focuses them into the holes of the topmost GEM, where they experience gas multiplication. At the hole exit, the multiplied electrons are extracted into the *transfer region* between two consecutive GEMs and are

transferred further into the holes of the subsequent GEM. After a second stage multiplication in the holes of GEM2, electrons are extracted from the holes of GEM2 into the *induction region* and towards the readout anode. The fast drift of the electrons in the induction gap induces very fast and short signals on the anode and the attached electronic circuit, guaranteeing high rate capability. As the electron transverse diffusion is comparable with the pitch, the holes of the consecutive GEM elements do not have to be aligned with that of GEM1.

Due to the strong dipole field in the hole vicinity (Fig. 2.10a), the electron transfer through the different stages of the detector is not fully efficient and electron losses are inevitable; ways to optimized electron transport were the subject of intense studies both experimentally and in simulations [84, 83, 93, 94, 95]. The guiding principles of electron transport in GEMs and the influence of the detector potentials are summarized below.

With increasing E_{drift} values, the focusing field generated by the cross-GEM voltage ΔV_{GEM1} may fail to collect all electrons from the drift region into the holes, and some will be collected at the top-GEM1 electrode instead. While only affecting the energy resolution when a large number of primary electrons has to be detected, this loss mechanism is quite critical in applications with only few or even single primary electrons (e.g. emitted from a photocathode), where it reduces the detection efficiency. Therefore, operation conditions have to be found that minimize electron losses to the top face of GEM1 and guarantee high detection efficiency.

At the bottom side of GEM1, the major fraction of the multiplied electrons is extracted from the holes and guided into the next GEM. For a constant potential ΔV_{GEM1}, the extracted charge fraction depends approximately linearly on the transfer field E_{trans}, defined as the potential difference between the bottom GEM1 electrode and the top electrode of the consecutive GEM2. But for increasing values of E_{trans}, losses to the top electrode of GEM2 become significant similar to electron losses to the top face of GEM1 for high E_{drift} values. Electron losses in the transfer region are inevitable with typically only 30–70% of the charge being transferred from one GEM stage to the next. However, electron losses in the transfer region are not detrimental to the detection efficiency of the detector; they can be easily compensated for by raising the gain.

In the induction region below the last GEM, only a fraction of the charge is extracted from the holes towards the anode, while the rest is collected on the bottom GEM electrode. Unlike in the transfer region, high electric fields E_{ind} can be applied here, allowing for a good charge extraction approaching unity for high E_{ind} values [96]. Charges can also be multiplied within the induction region, as discussed in [83] and Sec. 6.4.4. The subject of charge transport in multi-GEM detectors is further discussed in detail in Sec. 4 in the case of single photoelectrons created in the vicinity of the topmost GEM.

In analogy to the electron transport, also a fraction of the avalanche ions generated in the GEM holes is lost on the various electrodes and does not reach the drift region. The reduced *ion back-flow* of GEM detectors is very important for the realization of GEM-based GPMs and is subject of Sec. 6 of this thesis.

Due to the described electron losses in GEM detectors, one distinguishes the *real gain* from the *effective gain*. The first describes the real amplification experienced by a single primary electron, neglecting all losses during charge transfer. The second describes the *usable electron*

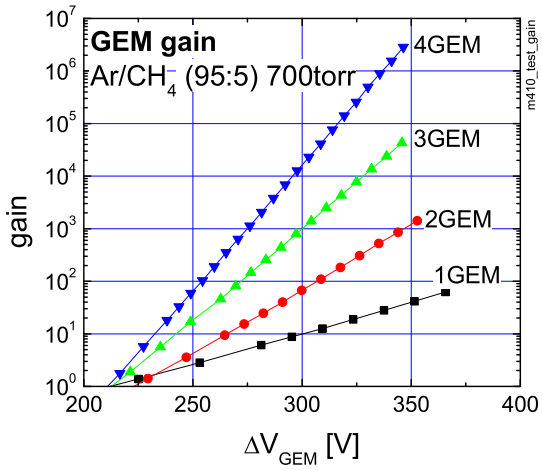

Fig. 2.13: The gain-voltage characteristics of multi-GEM detectors. The gain sharing between the individual stages is evident from the slope of the curves.

charge collected on the anode; it is calculated from the ratio of the amount of electrons collected on the anode n_{anode} and the the number of primary electrons n_0 created in the drift region according to

$$G_{eff} = \frac{n_{anode}}{n_0} \,. \tag{2.10}$$

For practical purposes, only the effective gain is of interest and *gain* is subsequently used synonymously.

Further GEM elements can be easily added to form triple- or quadruple-GEM detectors, with additional transfer regions for which the above principles of charge transfer apply accordingly. The designations of the additional elements follow straightforward from Fig. 2.12. These detectors allow for reaching even higher maximum gains at lower operation voltages ΔV_{GEM} on each GEM element, making them more stable and less prone to discharges [79, 97]. The gain increase versus ΔV_{GEM} (equal on each GEM) for multi-GEM detectors operated in atmospheric Ar/CH_4 is provided in Fig. 2.13. The slope of the gain-voltage curve of the quadruple detector is roughly four times that measured in a single-GEM detector.

The individual GEMs in a cascaded GEM detector can be operated with different ΔV_{GEM} and E_{trans} values, influencing the discharge probability [98] and the charge transport properties of the detector. They can also have different hole geometries; such an arrangement was found to reduce the ion back-flow in the detector [99].

Multi-GEM detectors have reached a high degree of maturity and due to their high rate capability [100, 101], excellent position (∼50 μm RMS) [102, 101, 103] and time resolution [101], design flexibility, robustness and reliability are employed in a multitude of applications, e.g. for particle tracking in high energy physics experiments [101, 104], neutron imaging [105, 106], Time Projection Chambers (TPCs) [107, 108], two-dimensional X-ray detection [109, 110], medical imaging for cancer detection and diagnosis [111] and of course in advanced

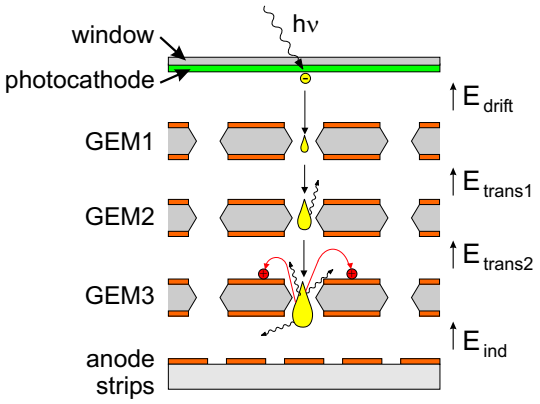

Fig. 2.14: A triple-GEM-GPM with a semi-transparent photocathode. The designation of the electric fields are indicated.

gaseous photomultipliers [112, 113]. The electron avalanche confinement in the GEM apertures proves to be beneficial for the operation [114], quenching photon mediated secondary processes. This allows the application of GEM detectors in conditions in which wire chambers or other detectors with geometries open to secondary photons can no longer operate: e.g. high gain operation in pure noble gas mixtures [114] or pure CF_4 [65] and high pressure operation [115]. GEM detectors also operate with a considerably reduced avalanche-ion back-flow from the multiplying stages of the detector into the conversion and drift region [99]. The ion back-flow reduction in cascaded GEMs and other structures will be discussed below in Sec. 6. The above mentioned properties together with the possibility of reaching gas gains exceeding 10^6 for single electrons makes multi-GEM detectors multipliers of choice for advanced gaseous photomultipliers suitable for single-photoelectron imaging.

Multi-GEM GPMs

Coupling a multi-GEM detector to a semi-transparent photocathode constitutes a GEM-GPM; such an arrangement is schematically shown in Fig. 2.14. In the framework of this thesis, such detectors were successfully equipped with CsI UV photocathodes and systematically investigated in various gas mixtures. Gains exceeding 10^6, with good time resolution of $\sim$2 ns in CF_4 and reduced ion- and photon feedback were reached ([116] and references therein), superior to the performance of any wire-based GPM.

Furthermore, in the framework of this thesis, the efficiency of single electron detection was extensively studied both experimentally [93, 94] and in simulations [95]. Obviously, it is directly related to the efficiency of extracting photoelectrons from the photocathode and focusing them into the apertures of the topmost GEM, and depends strongly on the electric field E_{drift} between the photocathode and the first GEM electrode. As was discussed above, for high E_{drift} values a fraction of the photoelectrons do not enter the GEM apertures, but are absorbed on the top GEM1 electrode. On the other hand, high electric fields close to the photocathode are required, to reduce the probability for photoelectron backscattering [63], necessary to efficiently extract electrons from the photocathode.

The absolute photoelectron detection efficiency in multi-GEM detectors was systematically investigated and it was demonstrated [93, 94] that by allowing for a moderate pre-

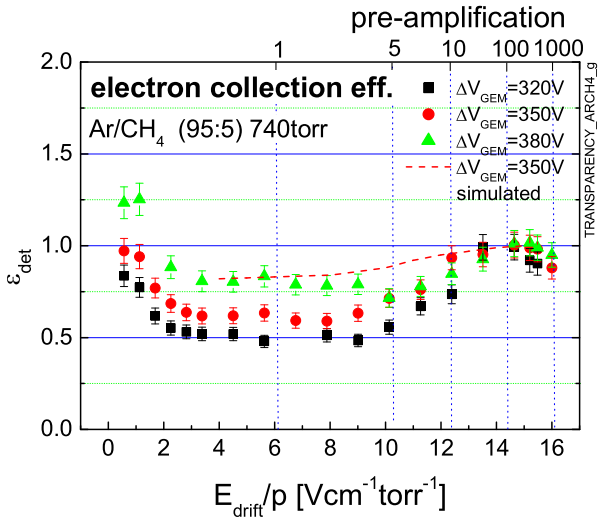

Fig. 2.15: The absolute detection efficiency for single photoelectrons emitted from a semi-transparent photocathode coupled to a GEM, as a function of the reduced electric field E_{drift}/p (bottom scale) and of the pre-amplification factor (top-scale) in the gap between the two. Full efficiency is obtained for a pre-amplification of ∼10 (from [94]).

amplification in the drift gap, losses of primary electron to the top GEM electrode can be compensated for (Fig. 2.15) in most common gas mixtures. This ensures an efficient operation of a GEM detector coupled to a semi-transparent photocathode. As a drawback of such a mode of operation, all avalanche-generated ions back-flowing to the drift region are accelerated by the high field E_{drift} (typically a factor 5–10 higher than in standard operation) and impinge on the photocathode with increased kinetic energy. If this leads to an enhanced photocathode aging and stronger ion-feedback (see Sec. 5) remains to be investigated.

Cascaded GEM-GPMs having a reflective photocathode deposited directly on the top GEM element were investigated in this work; the results are presented in Sec. 4.

2.7.4 The Micro Hole & Strip Plate (MHSP)

The Micro-Hole & Strip Plate [117, 118] was only recently introduced as a new type of micro-pattern gas detector, originally developed for the detection of x-rays. It consists of two independent electron amplification stages realized in a single element: a first amplification stage in GEM-like holes and a second stage amplification on thin anode strips on its bottom side, similar to Micro Strip Gas Counters (MSGCs) [77]. Like GEMs, MHSPs are manufactured from a thin polymer film, metal-coated on both sides and perforated by a dense matrix of small holes; in addition one side is structured with strips. Fig. 2.16a, shows the MHSP bottom side with the thin anode- and wide cathode-strips, the later encircle the apertures. The field configuration in a MHSP electron multiplier is schematically presented in Fig. 2.16b; it also indicates the MHSP potentials V_{hole}, between the top MHSP electrode and the cathode strips, and V_{A-C} between the anode and cathode strips.

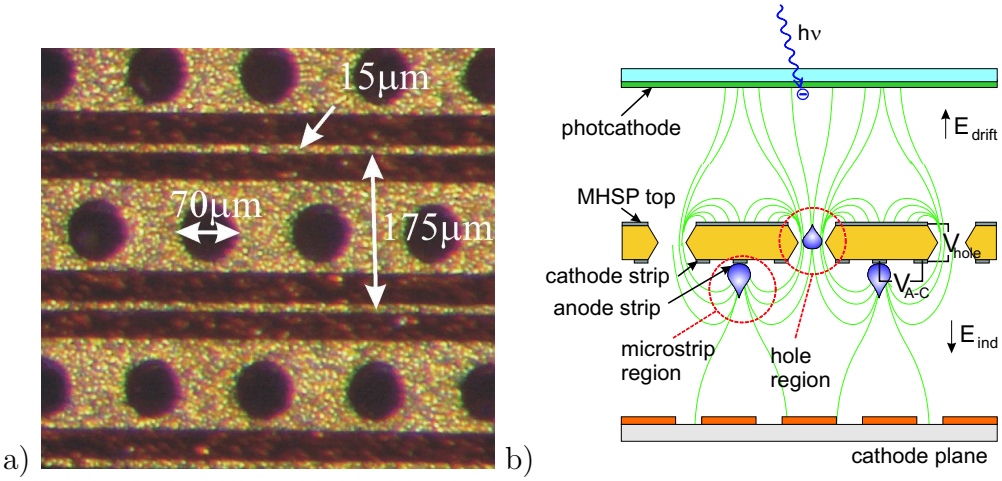

Fig. 2.16: a) Microscopic view of the bottom side of a MHSP element. One recognizes the GEM like holes in the wide cathode strips and the thin anode strips where the second electron multiplication occurs. The metal on the top MHSP side is not structured. b) Schematic illustration of a MHSP-GPM with semi-transparent photocathode and two-stage multiplication (from [119]).

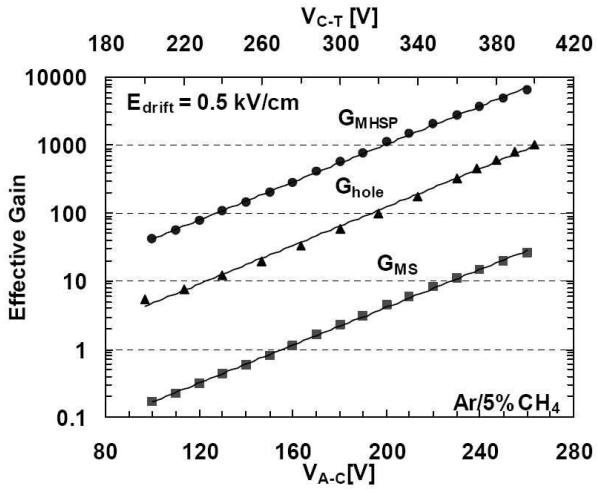

Fig. 2.17: Gain-voltage characteristic of a single MHSP element operated in 760 torr Ar/CH_4 (95:5). The hole gain G_{hole} is given as a function of V_{C-T} (used synonymously for V_{hole}) for constant V_{A-C}=0V and E_{ind}=-0.2 kV/cm. The strip gain G_{MS} is given for V_{hole}=350V and E_{ind}=-5 kV/cm (from [120]).

When appropriate potential differences are applied to the detector elements, electrons drifting into the strong electric field regions in the holes and around the anode strips experience a two-stage gas amplification and are collected on the anode strips. The first amplification in the *hole region* depends exponentially on the V_{hole}. Subsequently, the majority of the avalanche electrons is extracted from the holes towards the thin anode strips and the second amplification process occurs in the *microstrip region*; its magnitude depends on the anode-cathode voltage V_{A-C}. Gain-voltage characteristics of a MHSP element operated in atmospheric pressure Ar/CH_4 (95:5) are shown in Fig. 2.17.

The MHSP has the advantage of being a two-stage electron amplifier realized in a single

element. It allows reaching high gains approaching 10^5 [121] in a single element. As the vast majority of avalanche photons is generated close to the anode strips, photon-induced secondary effects are drastically reduced.

As pointed above, ion back-flow to the photocathode was identified to be one of the major obstacles in conceiving high gain GPMs sensitive to visible light (see Secs. 5 and 6). In the framework of this thesis, it was found that the ion back-flow can be considerably reduced in MHSPs: a large fraction of the avalanche ions are collected on the cathode strips, while another fraction can be diverted to the cathode plane by operating with a high induction field E_{ind} of appropriate polarity. A cascade of 3 GEM elements and one MHSP was operated with almost an order of magnitude lower ion back-flow when compared to a 4-GEM cascade of the same gain [120], making such a assembly an attractive option for advanced GPMs.

3. MATERIALS AND METHODS

3.1 The bi-alkali photocathode system

3.1.1 General overview

A dedicated, 3-chamber ultra-high vacuum system, designed and built at the radiation detection physics group, was operated for the production and characterization of K–Cs–Sb photocathodes and their sealing to electron multipliers to form sealed, visible-light-sensitive GPMs. A schematic illustration and a photograph of this setup are provided in Fig. 3.1. It consists of three ultra-high vacuum chambers ($\sim 10^{-9} - 10^{-10}$ torr), evacuated by turbo-molecular pumps and baked out for ∼48 hours prior to operation. They are separated from each other by gate valves. The *load-lock chamber* is used for introducing and baking out photocathode-substrates prior to their transfer into the second and central chamber, the *activation chamber*. Here, the chemical compounds are evaporated onto the glass substrate to form a photocathode. In the same chamber, the QE of the photocathode can be measured in-situ. In the third vacuum chamber, the *sealing chamber*, the electron multiplier is introduced, tested and baked before it is sealed in a gaseous environment to a photocathode. The photocathode substrate can be transferred between the chambers by magnetic manipulators. The sealing chamber is also used in several experiments for operation of electron multipliers in combination with K–Cs–Sb photocathodes without sealing the two components.

The individual elements of the system are described in detail in the following sections.

3.1.2 The load-lock chamber

Designed for introducing and baking out of photocathode substrates prior to their transfer into the activation chamber, the load-lock chamber is baked out with internal quartz lamps up to 220°C and is pumped by a turbo-molecular pump[1], backed by a *dry* diaphragm pump. Typically, a pressure of $\sim 5 \cdot 10^{-9}$ torr is reached after a bake-out at 200°C for 48 hours. The load-lock chamber is also used for pre-melting indium alloy wires in the detector packages (see Sec. B). The temperature of the chamber is monitored by a thermocouple, which is positioned either on the dedicated photocathode holder (see Sec. 3.2.1) or, in the case of indium-alloy melting, on the detector package holder.

3.1.3 The activation chamber

Photocathode production and characterization takes place inside the activation chamber. It is baked out internally by quartz lamps before photocathode production and pumped by a

[1] V-70, Varian

a)

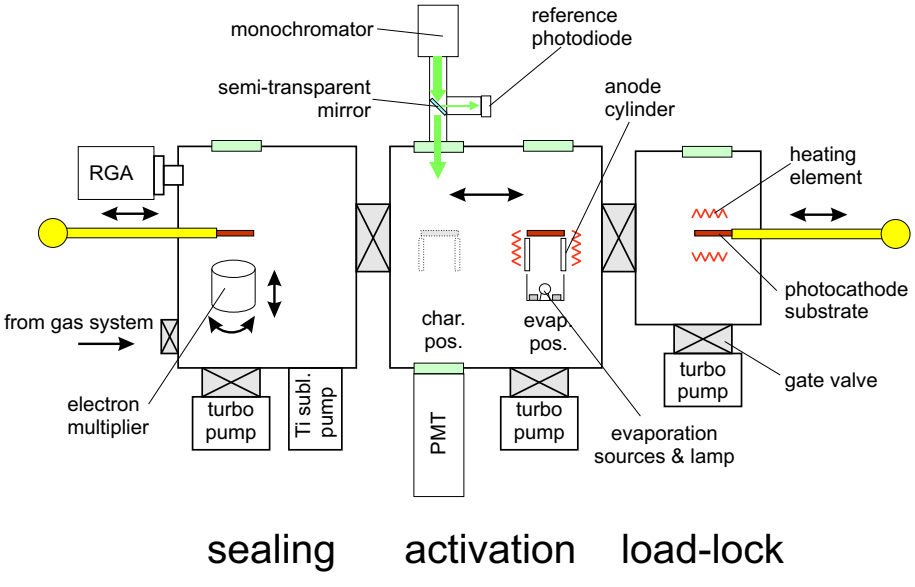

b)

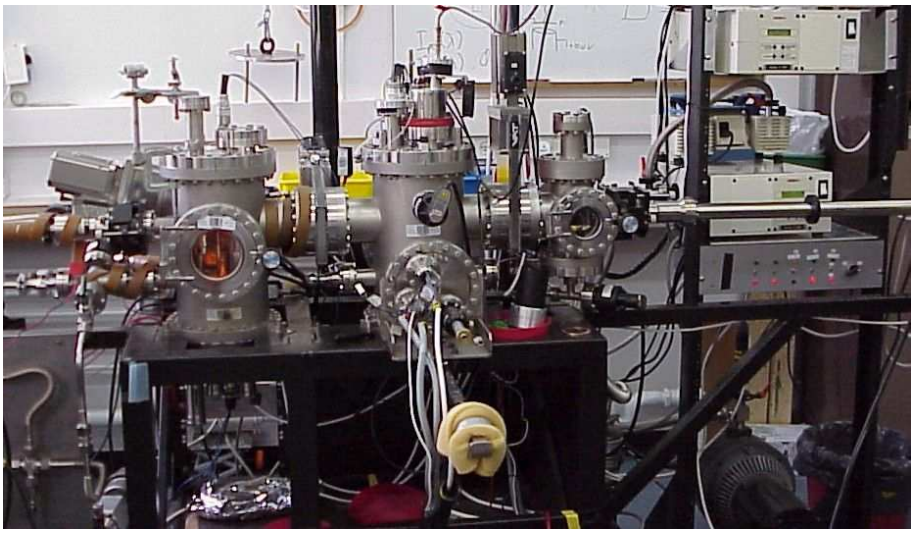

Fig. 3.1: a) Schematic illustration and a b) photograph of the vacuum-system for preparation of sealed, visible-light-sensitive GPMs. The system consists of three chambers, an introduction chamber for substrate baking, a central chamber for photocathode evaporation and characterization, and a third chamber for detector testing and sealing.

turbo-molecular pump[2] backed by a scroll pump. A base pressure of $3 \cdot 10^{-10}$ torr is typically reached after a bake-out at 250°C for 48 hours. Additional quartz lamps are located close to the photocathode substrate holder and allow for local heating during the photocathode production process. The temperature in the chamber is monitored with thermocouples placed close to the substrate holder and the evaporation sources. A residual gas analyzer[3], externally bakeable, can be attached to the chamber for monitoring the vacuum quality. A typical composition of the residual gas in the activation chamber after bake-out is provided in Tab. 3.1.

[2] V-550, Varian
[3] CIS300 RGA, Stanford Research Systems

gas	activation chamber partial pressure [torr]	sealing chamber partial pressure [torr]
hydrogen	$2.6 \cdot 10^{-10}$	$2.1 \cdot 10^{-9}$
water	$3.4 \cdot 10^{-11}$	$1.3 \cdot 10^{-9}$
nitrogen	$1.3 \cdot 10^{-11}$	$2.7 \cdot 10^{-10}$
oxygen	$1.6 \cdot 10^{-14}$	$2.6 \cdot 10^{-11}$
carbon dioxide	$2.2 \cdot 10^{-11}$	$1.1 \cdot 10^{-10}$
total	$3.3 \cdot 10^{-11}$	$3.9 \cdot 10^{-9}$

Tab. 3.1: Typical residual gas composition in the activation and sealing chambers after bake-out.

The *evaporation position* consists of three separate but identical evaporation stations placed on a moving arm; each of them permits the production of two K–Cs–Sb photocathodes. Each station contains Sb, K and Cs evaporation sources and a small incandescent lamp used for light transmission measurement during the photocathode processing. Antimony shot[4] is placed in a small Ta evaporation boat and pre-melted in high vacuum before installation in the activation chamber. Both K and Cs evaporation sources are provided by the manufacturer in form of small dispensers[5], three of each are interconnected in series by spot-welding and are placed in the respective source holders. All sources are outgased during the bake-out process by resistive heating. A shutter above the evaporation sources allows to quickly terminate the evaporation during photocathode processing. A sapphire window in the activation chamber above the evaporation position allows the illumination of the photocathode during processing. The steps of K–Cs–Sb photocathode fabrication are described in detail in Sec. 3.2.

The *characterization position* allows the in-situ measurement of the absolute QE of the photocathode: a calibrated photomultiplier[6] operated in photodiode mode (gain=1) is placed on the sapphire window below the characterization position and a monochromator[7] is placed on the top sapphire window. A Hg(Ar) lamp[8] is used as light source for the monochromator; it exhibits narrow spectral lines in the sensitivity range of bi-alkali photocathodes (254.6, 312.5, 365.0, 404.6, 435.8, 546.0 nm). A fraction of the light on the path from the monochromator to the sapphire window is reflected by a semi-transparent mirror onto a photodiode; the role of the latter is to monitor eventual light intensity fluctuations of the Hg(Ar)-lamp.

Inside the activation chamber, the substrate and its holder are placed on top of a glass cylinder with a cylindrical stainless steel anode inside. The substrate-anode complex can be displaced between the evaporation and characterization positions of the activation chamber. Fig. 3.2 shows a sketch of the substrate-anode complex positioned above the evaporation sources. The glass cylinder confines the evaporation vapours and prevents contamination of the chamber while also protecting the photocathode from pollutants outgasing from the vacuum chamber walls. The photocathode holder and the anode cylinder are electrically

[4] Sb shot, 5N, Johnson Matthey
[5] Cs/NF/5.5/17 and K/NF/3.1/17, SAES Getters
[6] XP2020Q PMT, Photonis
[7] monochromator 77250, Oriel
[8] Hg(Ar)-lamp 6035, Oriel

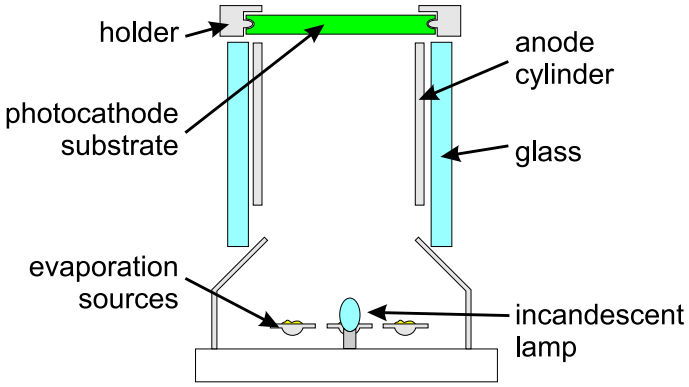

Fig. 3.2: Sketch of the photocathode-anode complex placed above the evaporation position inside the activation chamber.

connected to the outside of the chamber for current measurements or for applying a high voltage.

3.1.4 The sealing chamber

The sealing chamber is baked out externally by heating tapes and internally by quartz lamps; it is pumped by a turbo-molecular pump[9] backed by a dry scroll pump. An additional titanium sublimation pump[10] can be used to further improve the vacuum, particularly by reducing the partial pressure of water. A base pressure of $4 \cdot 10^{-9}$ torr is typically reached after a 48 hours bake-out. A residual gas analyzer, externally bakeable, can be attached to the chamber for monitoring the vacuum quality. A typical composition of the residual gas in the sealing chamber is provided in Tab. 3.1.

A special holder carries the detector package. It is mounted on a manipulator that allows both vertical and rotational displacements, required during package-photocathode sealing. Furthermore, it establishes electrical contact from the various detector electrodes to the section of the resistor network that is located inside the vacuum chamber and to the electrical feedthroughs connected to external electronic circuitry (see Sec. 8 and App. A). The photocathode–detector assembly can be illuminated from top through a sapphire window.

3.1.5 The gas system

The gas system is separated from the sealing chamber by a shut-off valve; it allows filling the sealing chamber with high purity gas mixtures required for detector operation and sealing. It can be baked by external heating tapes and is pumped with a turbo-molecular pump[11] or, for quick evacuation (*roughing*), with a clean mechanical scroll pump. After baking the gas system tubing for 48 hours at 200°C, a pressure of $3 \cdot 10^{-6}$ torr is typically achieved.

The gas flow and the mixture ratio of up to two gases is regulated by separate mass-flow controllers. In all experiments Ar and CH_4 of 99.999% purity were used. Before flowing into

[9] V-250, Varian
[10] 1020S, Thermionics Laboratory Inc.
[11] V-70, Varian

the sealing chamber, the gas mixture passes through a filter[12], purifying noble gases, N_2 and CH_4 to a 1 ppb level at a maximum flow of 1 standard liter per minute.

3.2 Fabrication of semi-transparent bi-alkali photocathodes

The production of K–Cs–Sb photocathodes in laboratory conditions was successfully established in our group some time ago [23]. It requires a careful choice and design of the experimental equipment and of all materials used in the vacuum system due to the high chemical reactivity of K–Cs–Sb photocathodes [32]. Ultra high vacuum conditions with very low residual water content are required for the successful fabrication of stable and high QE photocathodes. The system described above was designed for that purpose and allows the production of several semi-transparent K–Cs–Sb photocathodes per week.

The detailed procedure of K–Cs–Sb photocathode fabrication is presented below. It was developed and optimized in our group over a long time period and was continuously refined, in order to achieve high QE photocathodes with good reproducibility.

3.2.1 Photocathode substrate preparation

The photocathode substrate is made from special Kovar-glass[13], ∅64×5 mm. It matches the thermal expansion coefficient of the Kovar-made detector packages, which is a prerequisite for a leak-tight sealing of the two components. Two grooves are machined on the sides of the window, required for fixing it in the stainless steel substrate-holder. New windows are scrubbed with a soft sponge and a few grains of Alconex powder followed by a 15 minute rinse in demineralized water. They are dried by flushing high purity argon. A further cleaning step by glow discharge in air is performed just prior to the evaporation of a 10 mm wide metal ring on the circumference and in the grooves of the substrate. The metal ring serves two purposes: it provides electrical contact to the photocathode partially evaporated on it and it is required for sealing the substrate to a detector package (see App. B). It is deposited on the rotating substrate by thermal evaporation under 45° incidence. The metal layer comprises a chromium (100 nm) and a copper (200 nm) layer; all metals have a purity of 99.999%. The window is then tilted to 90° and a further 60 nm layer of copper is evaporated only onto the window sides and the grooves to ensure good electric contact to the substrate holder. The photocathode overlaps partially with the metal ring, ensuring good electrical contact. The previously used 3-layer metal ring of Cr/Ni/Au was abandon, as Cr/Cu was found to give a more reliable sealing to the detector packages [122]. Following evaporation, the windows are either installed in the load-lock chamber immediately or stored in vacuum until needed.

Used windows can be recuperated by removing the metals from the substrate with a chromium etchant[14] followed by the cleaning procedure for new windows.

The photocathode substrate is mounted in a dedicated stainless steel substrate-holder, gripping it by the grooves on the side during the whole process of photocathode production,

[12] GateKeeper 35K, Aeronex Inc.
[13] No. 8245, Schott
[14] CR-7, Cyantek Inc.

characterization and sealing to an electron multiplier. After the holder is screwed onto the end of the manipulator in the load-lock chamber, pumping is started and the substrate is baked by the internal quartz lamps at 200°C for 48 hours. After cooling to room temperature, the baked substrate is transferred into the activation chamber with the magnetic manipulator at a pressure of typically $4{\cdot}10^{-8}$ torr .

3.2.2 Photocathode evaporation

Antimony evaporation

Firstly, the substrate is placed in the characterization position and its light transmission characteristic is evaluated; it is required for the calculation of the photocathode's absolute QE (Sec. 3.2.3). The substrate is illuminated by the monochromator and the light transmitted through the substrate is measured on the PMT. The photocurrent $I_{PMTtrans}(\lambda)$ is recorded for the characteristic wavelengths of the Hg(Ar)-lamp (see Sec. 3.1.3). To be able to compensate for variations in the lamp intensity, it is monitored by the photodiode current $I_{PDtrans}(\lambda)$.

Following the transmission measurement, the substrate is placed in the evaporation position and heated to 175°C by the quartz lamps close to the photocathode substrate; after reaching this temperature, the heating is switched off.

A photodiode is then placed on the top sapphire window and the photocathode substrate is illuminated from below with the incandescent lamp of the evaporation station. The initial current recorded on the photodiode defines a photocathode transmission of 100%. By applying a current of 12–15A through the Sb-boat antimony is evaporated onto the substrate. Once the Sb film reduces the light transmission to 75%–85%, the evaporation is terminated by closing the shutter above the evaporation sources and switching off the current through the Sb-boat. The process of Sb-evaporation can be very quick (5-20 seconds) and has to be performed cautiously, as the thickness of the Sb layer strongly influences the final QE of semi-transparent K–Cs–Sb photocathodes. A too thick Sb layer forms a mirror-like film on the glass substrate reflecting a large fraction of the incident light, while a too thin layer is not sufficient for the formation of the required chemical composition. Sb-layers that reduce the light transmission by 15%–25% were found to yield the best results.

Potassium evaporation

During potassium evaporation, the substrate is constantly kept at 185°C. The photodiode on the top sapphire window is replaced by a Ar(Hg)-lamp, illuminating the photocathode substrate from above. Alternatively, a UV-LED[15] with a narrow emission spectrum peaked at 375 nm was used in some cases. A positive voltage of 100V is applied to the anode cylinder and the photocathode substrate is connected to a picoampermeter for monitoring the photocurrent I_{PC} during the K evaporation process. By applying high current (4–6A) to the K-dispensers, potassium is evaporated onto the photocathode substrate, forming a Sb–K photocathode. During the evaporation process, the current through the dispensers is kept

[15] NSHU590A, Nishia

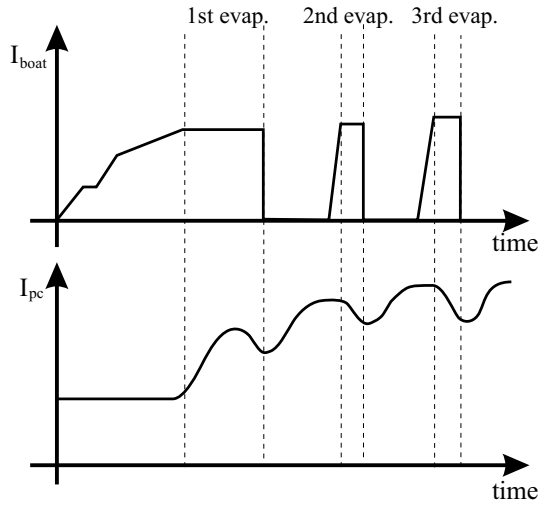

Fig. 3.3: The Cs evaporation process: the top graph shows the time variation of the applied current through the evaporation dispenser, while the bottom graph shows the resulting photocurrent.

constant ensuring a steady evaporation and a slowly and continuously rising photocurrent I_{PC}. After 1–3 minutes of evaporation, the photocurrent, and therefore the QE, reaches a plateau and eventually starts dropping. To ensure that the peak value of I_{PC} was reached and sufficient K was evaporated, the evaporation is terminated only after I_{PC} dropped to $\sim$90% of its maximum value.

Cesium evaporation

Following the potassium evaporation, the temperature is allowed to drop to 155°C before cesium is evaporated by applying a current of 4–6A to the appropriate dispenser. The Cs-activation proceeds analogous to the K-evaporation: the current through the dispenser is increased until I_{PC} starts rising, indicating an increase in QE. It is then held constant until I_{PC} reaches a peak and drops again to $\sim$90% of its maximum value after which the evaporation is terminated.

The formation of the K–Cs–Sb compounds continues for some time after the evaporation is stopped, and the resulting increase in QE is reflected by a rising photocurrent I_{PC}, typically exceeding the maximum value reached during the evaporation process. Repeating the Cs evaporation process a few times can yield considerably higher QE photocathodes compared to a single evaporation step. The process of repeated activation is schematically shown in Fig. 3.3: after each Cs evaporation the photocathodes sensitivity increases to some degree until a saturation value is reached.

3.2.3 Photocathode characterization

After the photocathode has cooled to room temperature (typically a 10 hours time period), the photocathode-anode complex is displaced to the characterization position and a positive voltage of 100V is applied on the anode cylinder. Illuminating the photocathodes from above

with the monochromator, the currents on the photocathode, $I_{PC}(\lambda)$ and on the light intensity monitoring photodiode, $I_{PD}(\lambda)$, are measured as a function of the wavelength. Together with the photocathode substrate transmission, measured prior to the photocathode evaporation (see Sec. 3.2.1) the absolute QE of the photocathode is given by the following formula:

$$QE(\lambda) = \left(\frac{I_{PC}(\lambda) - I_{PC}^{dark}}{I_{PMTtrans}(\lambda) - I_{PMTtrans}^{dark}}\right)\left(\frac{I_{PDtrans}(\lambda) - I_{PDtrans}^{dark}}{I_{PD}(\lambda) - I_{PD}^{dark}}\right) \cdot QE_{PMT}(\lambda) \cdot T_w(\lambda) \tag{3.1}$$

with:

$QE(\lambda)$ – photocathode quantum efficiency

$I_{PC}(\lambda)$ – photocurrent measured on the photocathode

I_{PC}^{dark} – photocurrent measured on the photocathode with the monochromator lamp switched off

$I_{PD}(\lambda)$ – current measured on the monitoring photodiode

I_{PD}^{dark} – current measured on the monitoring photodiode with the monochromator lamp switched off

$I_{PMTtrans}(\lambda)$ – current on the PMT from the transmission measurement

$I_{PMTtrans}^{dark}$ – current on the PMT from the transmission measurement with the monochromator lamp switched off

$I_{PDtrans}(\lambda)$ – current on the monitoring photodiode from the transmission measurement

$I_{PDtrans}(\lambda)$ – current on the monitoring photodiode from the transmission measurement with the monochromator lamp switched off

$QE_{PMT}(\lambda)$ – PMT quantum efficiency as supplied by manufacturer (see Tab. 3.2)

$T_w(\lambda)$ – sapphire window light transmission as supplied by manufacturer (see Tab. 3.2)

λ [nm]	546	435	405	365	312	254
$QE_{PMT}(\lambda)$ [%]	6.29	24.74	28.00	29.38	28.22	23.19
$T_s(\lambda)$	0.8	0.8	0.8	0.8	0.8	0.8

Tab. 3.2: XP2020Q PMT quantum efficiency and light transmission through the sapphire window for the characteristic wavelengths of the Hg(Ar)-lamp.

The QE as a function of wavelength of a good semi-transparent K–Cs–Sb photocathode is provided in Fig. 3.4 together with the QE of the reference PMT. The drop in QE for wavelengths below 400 nm is due to the reduced light transmission of the Kovar glass substrate.

Following the fabrication and characterization, the photocathode is ready to be transfered into the sealing chamber for coupling to an electron multiplier.

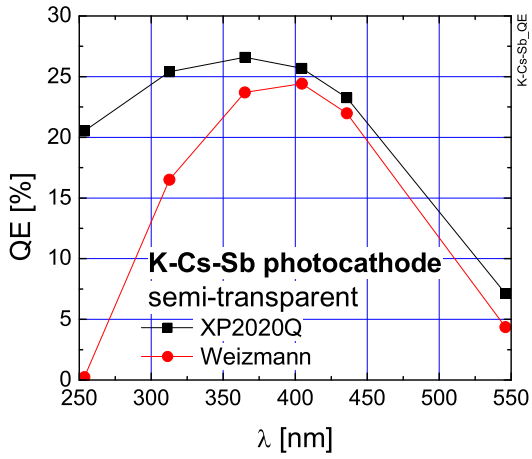

Fig. 3.4: The absolute QE of a good semi-transparent K–Cs–Sb photocathode produced in our system. The absolute QE of the XP2020Q PMT used for the transmission measurement and having the same type of photocathode is provided for comparison.

3.2.4 Concluding remarks

Fabrication of a semi-transparent K–Cs–Sb photocathodes is a complex task and many factors influence the outcome of the experiment, some of which cannot be fully controlled. The exact fabrication procedure, times of evaporation, currents through the evaporation boats, photocurrents and QE values vary considerably from photocathode to photocathode. The procedure of photocathode fabrication can still be improved in terms of reliability and reproducibility.

Another method of K–Cs–Sb semi-transparent photocathodes fabrication by simultaneously evaporating Sb, K and CS is reported in [22, 123]. This method is reported to yield high QE K–Cs–Sb photocathodes with high reproducibility and might be considered for future modifications of our K–Cs–Sb photocathode fabrication.

3.3 The CsI photocathode fabrication system

Fabrication of high QE CsI photocathodes is considerably simpler. Firstly, only a single compound, namely CsI-salt, needs to be evaporated to form the photocathode. Secondly, CsI photocathodes are rather robust and retain their QE even when exposed to ambient air for a short time. Therefore the requirements on the vacuum system and the cleanliness of detector materials used in conjunction with these photocathodes are considerably less severe.

Fig. 3.5 schematically shows the experimental setup for CsI photocathode production. It comprises a high vacuum chamber connected via a gate valve to a turbo-molecular-pump. A base pressure of $\sim 10^{-6}$ torr is typically obtained after 6 hours of pumping without baking-out the chamber. The top glass bell jar closes the vacuum chamber with a thick rubber gasket and can be removed for accessing the internal parts and for placing a photocathode substrate inside. Three evaporation stations are located at the bottom, containing the evaporation

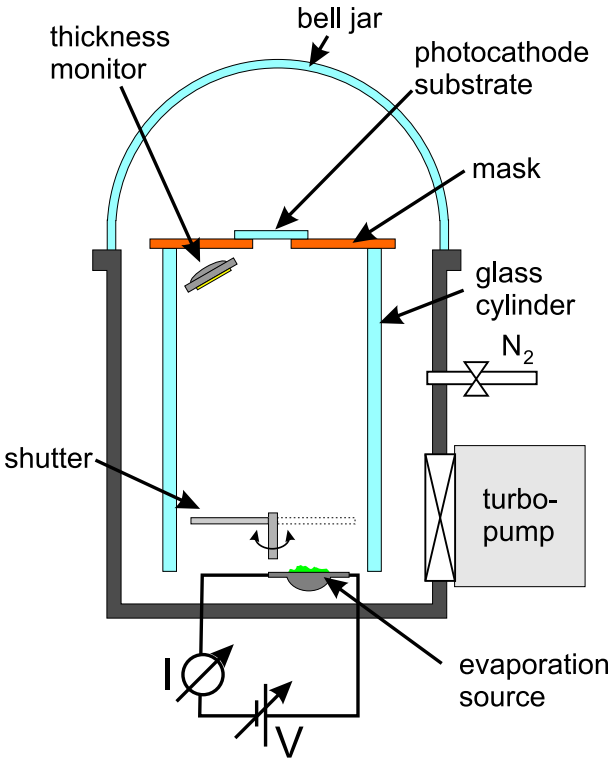

Fig. 3.5: Schematic illustration of the CsI-photocathode fabrication system.

sources for thermal evaporation. A rotatable shutter above the evaporation sources allows for a quick termination of the evaporation process. A glass cylinder confines the evaporation vapour to minimize the pollution of the chamber walls.

The photocathode substrate is situated ∼30 cm above the evaporation stations on top of a mask closing the glass cylinder, ensuring evaporation under normal incidence for small size photocathodes. The mask defines the photocathode's shape and size, while its thickness is monitored during the evaporation by a thickness monitor[16] located in the vicinity of the photocathode substrate.

To remove superficial pollutants from the CsI salt grains[17], it is filled into a small molybdenum crucible[18] and pre-melted in vacuum by sending a current of ∼100 A through it. The process of filling more CsI salt into the crucible and melting it, is repeated several times, until the crucible is uniformly filled with melted CsI and the material is ready for photocathode production.

3.4 Fabrication of CsI photocathodes

For semi-transparent CsI photocathodes, a UV transparent quartz window is used as substrate. The chamber is pumped to $\sim 10^{-6}$ torr before a 2 nm layer of aluminium is evaporated onto the substrate to provide for a good electrical contact for the relatively high resistivity

[16] STM-100, Sycon Instruments
[17] CsI 99.999%, Alfa Aesar
[18] ME2-.005TA, R.D. Mathis

CsI layer [3]. Subsequently, a 150–500 Å thick layer of CsI is evaporated at a rate of 5–10 Å/s by resistive heating of the evaporation boat (currents of 100–130 A). The evaporation process is terminated by closing the shutter on the evaporation sources and switching off the current through the boat, once the desired thickness is recorded on the thickness monitor. These photocathodes are too thick for reaching optimal QE values [17], but they are more stable compared to thinner CsI layers when exposed to ambient air during transport and assembly to an electron multiplier.

Reflective CsI photocathodes are prepared accordingly, but comprise a considerable thicker CsI layer of 2500–3000 Å evaporated on a conducting and chemically inert surface (e.g. a Au covered GEM face). They exhibit higher QE compared to semi-transparent ones and are more stable when exposed to ambient air.

CsI photocathodes are extracted from vacuum by introducing N_2 to the evaporator just prior to their incorporation in an experimental setup, minimizing their exposure time to ambient air and thus retaining their QE. Their relatively high stability permitted to use the same CsI photocathode for several weeks, despite being repeatedly exposed to ambient air during changes in the experimental setup.

Substrates for semi-transparent photocathodes were reused, after cleaning off the CsI layer by alternately rinsing them in ethanol and de-ionized water. If necessary, the aluminium coating of the quartz substrate was removed by scrubbing the substrate with a soft sponge and a few grains of Alconex powder followed by a rinse in de-mineralized water and drying in nitrogen.

3.5 Preparation of visible-sensitive GPMs in detector packages

The vulnerability of K–Cs–Sb photocathodes, even when exposed only to minute levels of oxygen, moisture or other residual gases, excludes their operation under continuous gas flow. A leak-tight sealing of the photocathode to the electron multiplier inside a gas filled vessel, or *detector package* is therefore required and all detector elements and fabrication methods have to be compatible with ultra-high vacuum requirements.

Two kind of detector packages were used by us.

- The first version, subsequently called *type A*, can house an electron multiplier made from up to 4 GEMs. It was operated successfully in combination with CsI and K–Cs–Sb photocathodes in sealed mode. Nevertheless its application was limited by voltage breakdown at the electrical feedthroughs connecting the detector elements inside the package to external circuitry. Furthermore the limited space rendered it impossible to place additional elements like gating electrodes or a segmented readout anode inside the type A detector package.

- The second package, subsequently called *type B*, was designed to allow for a more flexible detector configuration, providing enough space and electrical feedthroughs for up to 6 GEMs, gating electrodes and a 2D readout and at the same time simplifying the detector assembly procedure. During the thesis work, only the inner parts of this package were available, preventing the sealing of GPMs in the type B packages.

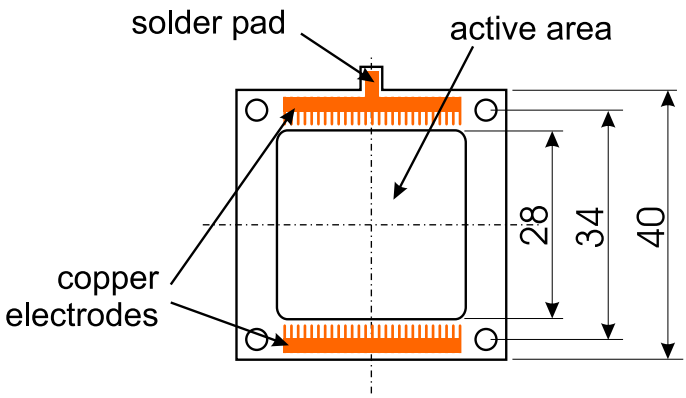

Fig. 3.6: Dimensions of a G-10 frame (1.6 mm thick) for preparation of a MWPC element. The frames for other detector elements have the same dimensions but a different design of the copper electrodes.

Nevertheless it was successfully used in an unsealed mode inside the gas-filled K–Cs–Sb photocathode fabrication setup.

The two package types and the materials and methods for assembling a cascaded GEM-GPM inside, are described in detail in App. A.

3.6 Preparation of GPMs for operation in gas-flow mode

Many experiments investigating the operation properties of electron multipliers were performed with GPMs having CsI rather than K–Cs–Sb photocathodes. Due to the relatively robust nature of CsI photocathodes, the requirements on cleanliness of the detector materials and preparation methods could be relaxed and operation in gas-flow mode was possible. The detector elements used in these experiments, their assembly to UV-sensitive GPMs and the setup for testing the CsI-GPMs are described below.

3.6.1 Detector elements

All detector elements were prepared on 40×40 mm^2 square frames, machined from 1.6 mm thick G-10. The central 28×28 mm^2 opening defined the active area of the detector; copper-pads prepared on the frames in printed-circuit technology, allowed to easily establish electrical contact to the detector elements' electrodes. Fig. 3.6 shows the dimension of the frames; the layout of the copper electrode on this particular frame is intended for holding a MWPC element. The different detector elements were prepared as follows:

- **GEM elements:** The GEM elements[19], designed with an active area of 28×28 mm^2 (see also Sec. 2.7.3) were cut to $\sim30\times30$ mm^2 in size and fixed with high voltage scotch tape to the G-10 frame. Their small size provided them with sufficient rigidity so that stretching was not necessary. The two metal faces of the GEM foil were contacted by conductive paint to separate solder pads on the G-10 frames.

[19] manufactured by CERN printed circuit workshop

- **Mesh electrodes:** Mesh electrodes were made from 50 μm in diameter crossed stainless steel wires, 0.5 mm apart (81% optical transparency). They were stretched and soldered to a G-10 frame having a copper electrode at the circumference of the central opening. The mesh was subsequently cut around the soldering and the wire ends were covered with epoxy glue.

- **MWPC elements:** MWPC elements were prepared from either 10 μm or 20 μm diameter tungsten wires. With a dedicated winding machine, sets of parallel wires, 1 mm apart, were stretched on large, robust metal frames (100×100 mm^2). These large frames were placed over small G-10 frames (Fig. 3.6) and the anode wires soldered to the copper electrodes of the G-10 frame. Subsequently, the wires were cut behind the soldering and their ends covered with epoxy glue.

- **Ion gate elements:** The ion-gate elements were prepared similar to MWPC elements described above. The wires were 50 μm in diameter and 1 mm apart. The G-10 frames for ion gate elements have two separate sets of copper electrodes, providing electrical contact to the "+" and "–" gating wire-sets respectively (see Sec.7).

According to the experimental requirements, the individual frames with the detector elements were stacked with nylon screws; the distances between the elements could be increased by placing additional spacers. This modular detector assembly scheme allowed for a very convenient detector preparation, allowing to easily add, remove or exchange elements.

3.6.2 Experimental setup

The stacked detector elements forming the GPM are mounted on a flange, carrying also the high-voltage feedthroughs. The flange closes one side of a vacuum vessel (Fig. 3.7), that can be pumped by turbo-molecular pump to 10^{-5} torr. The other side of the vessel is closed by a flange having a central quartz window which permits illuminating the GPM with UV-light. In several experiments this flange also supported the holder for semi-transparent CsI photocathodes. The system is operated in gas flow mode, using two gas-flow meters, differential pumping and regulated pressure control. During the installation of the GPM and the photocathode inside the vessel, it is continuously flushed with N_2, minimizing damage to the CsI photocathode due to moisture and oxygen.

3.7 Gain measurement of GEM detectors

3.7.1 Current mode

In most experimental conditions, the gain-voltage characteristics of a GPM can be determined relatively easy and with sufficient accuracy by current measurements. DC illumination of the photocathode generates a constant flow of photoelectrons (*photocurrent*) from the photocathode that enters the amplifying stages of the GPM. The current measured on the GPM anode is the product of the photocurrent and the effective gain of the detector. Normalized to the photocurrent measured in conditions with no gas amplification, the anode

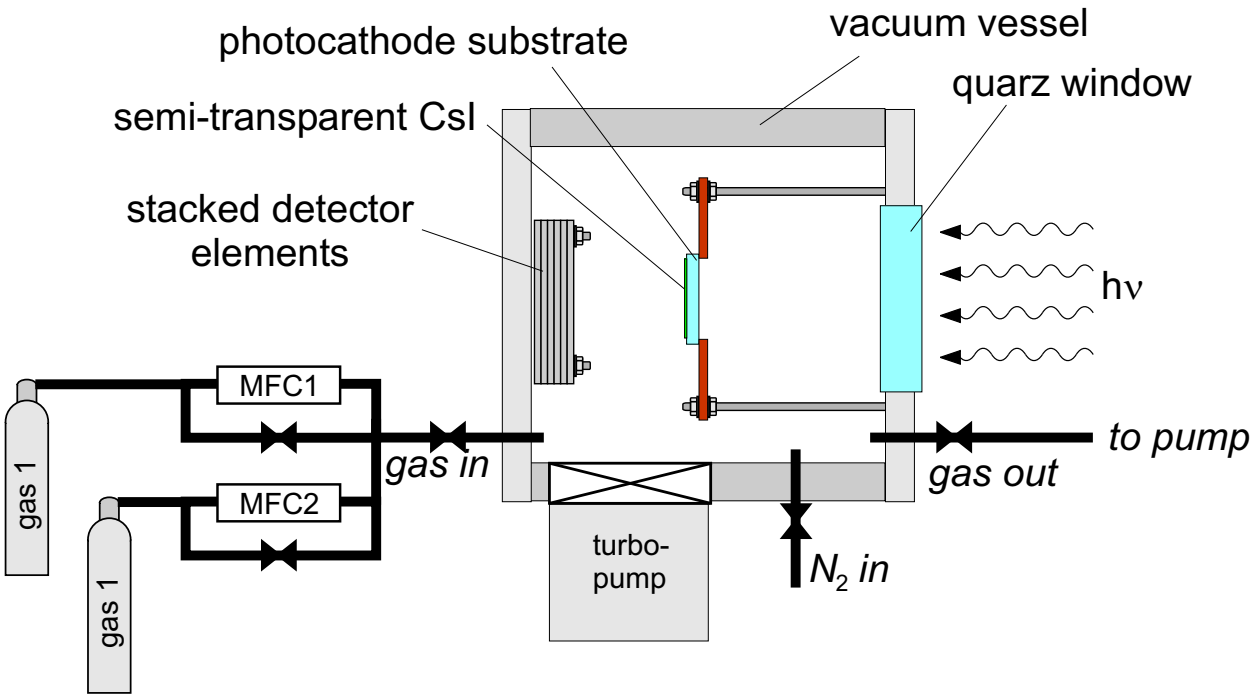

Fig. 3.7: The experimental setup for measurements in gas-flow mode.

current yields the effective detector gain G_{eff}. For reasons of detector stability, the anode current was limited to ∼10 nA; if necessary, the light intensity was reduced and the measured currents were corrected accordingly.

3.7.2 Pulse mode

The GPM gain can also be determined by a pulsed- illumination of the photocathode and analyzing the corresponding anode signals. The recorded avalanche charge is the product of the primary charge, i.e. in a GPM this is the number of photoelectrons per event, and the effective detector gain. With calibrated read-out electronics, the avalanche charge collected on the anode can be directly determined from the signals' pulse-height. Unfortunately, the number of primary photoelectrons cannot be determined with sufficient accuracy for multi-photon events: in most cases the number of photons hitting the photocathode as well as the GPMs effective quantum efficiency QE_{eff} (see Sec. 2.5) are not known. Therefore, in this work, all GPM gain measurements in pulse-mode were performed for *single-photon* illumination, generating single photoelectrons on the photocathode.

Due to avalanche fluctuations in single-electron multiplication, the corresponding pulse-height spectra are described by a Polya-distribution [2]:

$$p(q) \cong [(1+\theta)(q/G_{eff})]^{\theta} e^{-(1+\theta)(q/G_{eff})} \tag{3.2}$$

where q is number of electrons collected on the anode, G_{eff} is the single-electron gain and θ the avalanche saturation. In GEM-GPMs the multiplication-process is generally not saturated for most gas mixtures [124], and Eq. 3.2 simplifies, with $\theta = 0$, to a simple exponential distribution:

$$p(q) \cong e^{-q/G_{eff}} \tag{3.3}$$

By fitting an exponential curve to the single electron-spectrum, the GPM gain G_{eff} can be obtained.

3.8 The simulation tools

For calculating the electric fields and simulating the electron and ion drift lines, we used the finite-element programs Maxwell 3D [125] and GARFIELD [126] respectively. Unfortunately, the present implementation of GARFIELD and Maxwell 3D are partly inappropriate for obtaining quantitative results of the *electron multiplication and transport* from the simulation of GEM structures. Due to the strongly varying electrical field strength and directions close to the holes, the results are often critically influenced by the choice of simulation parameters [127]. The simulation results were still useful for providing a qualitative understanding of electron and ion transport in GPMs.

Part II

RESULTS

4. GEM-GPMS WITH REFLECTIVE PHOTOCATHODES

4.1 Introduction

As discussed in Chapter 2.2, reflective photocathodes are superior to semi-transparent ones in terms of QE and robustness. A GEM-based GPM with a reflective photocathode evaporated on the top electrode of a GEM was initially proposed in an early work on GEMs [128]. Some attempts made in this direction resulted in very low photoelectron yields [129] and were not pursued. The schematic arrangement of a multi-GEM detector with a reflective photocathode, 4 GEMs and a structured readout anode is shown in Fig. 4.1. Photoelectrons are extracted from the photocathode into the *drift region* and guided by the electric field into the holes of the first GEM. They experience first gas multiplication there and the major fraction of the avalanche charge is subsequently extracted and transferred to the following GEM stages and is further amplified. The effective quantum efficiency QE_{eff} is dictated by the effective photocathode area and by the field at the photocathode surface; the multiplication mechanism is dictated by the GEM hole geometry, electric fields across each GEM (ΔV_{GEM}) and between the GEMs (E_{trans}). The single photoelectron detection efficiency is a strong function of their focussing into the holes of GEM1, as discussed below.

Besides the advantage of employing reflective photocathodes, in such a detector geometry the photocathode is completely concealed from avalanche-generated photons. Photon feedback is therefore eliminated and does not limit the detector performance. A fraction of the avalanche-ions created in the various multiplication stages is back-flowing to the photocathode; they can induce secondary effects (ion feedback) and also damage the photocathode. Methods and results regarding ion feedback and back-flow reduction are discussed in Secs. 5 and 6.

The available surface area for photocathode deposition is reduced by the GEM holes, decreasing it's effective QE_{eff} accordingly. The *photocathode effective area* depends on the GEM geometry as shown in Tab. 2.1. For example in a dc140 standard GEM geometry the holes make up for 23% of the GEM surface, reducing the QE of the GPM averaged over the active area to 77% of its intrinsic value. The QE of a 2500 Å thick CsI photocathode evaporated on a dc140 GEM[1], measured in vacuum, is shown in Fig. 4.2. It is in good agreement with previously published data of good quality CsI photocathodes [17] considering the 23% loss of active area due to the holes.

The operation properties of such a GPM are presented in this chapter, namely the efficiency of extracting photoelectrons from the photocathode and collecting them into the amplification stages. Furthermore, results on high gain operation and time-resolution are presented.

[1] see Chapter 3.3 for details on the evaporation and QE measurement of CsI photocathodes

4.2 Single-photoelectron detection efficiency in GPMs with reflective photocathodes

As was discussed in Sec. 2.5 the photon detection efficiency ϵ_{photon} depends not only on the detector's QE but also strongly on the single-photoelectron detection efficiency ϵ_{det}. ϵ_{det} itself depends on many parameters: the detector geometry, the gas mixture, the electric field conditions, the multiplier gain, the electronics system etc. Once emitted from the photocathode surface into gas, the photoelectron has to be focussed into the first amplifying stage of the detector. The mechanism of electron extraction, transfer and multiplication in cascaded GEMs with semi-transparent photocathodes were shortly discussed in Sec. 2.7.3 and were extensively studied in [94, 95].

In the case of GEM-GPMs with reflective photocathodes the collection of photoelectrons into the multiplier is considerably more difficult. The possible fate of the photoelectron after its emission from the photocathode is schematically shown in Fig. 4.3 as steps a) to c):

a) Photoelectrons are extracted from the photocathode with an efficiency $\epsilon_{extr} < 1$ due to photoelectron backscattering on gas molecules (see Sec. 2.6.1). A proper choice of the gas mixture and high electric fields at the photocathode surface (typically >1 kV/cm at atmospheric pressure) minimize the photoelectron backscattering and allow for reaching values of ϵ_{extr} approaching unity.

b) Following extraction, the photoelectrons drift in the electric field into the GEM apertures with a probability ϵ_{hole}. Due to their diffusion in gas, not all photoelectrons enter the apertures – some may be collected at the top surface of the GEM electrode or on the cathode mesh above the GEM in unfavourable electric field conditions, reducing ϵ_{hole}. Photoelectrons that enter the aperture encounter high electric fields of

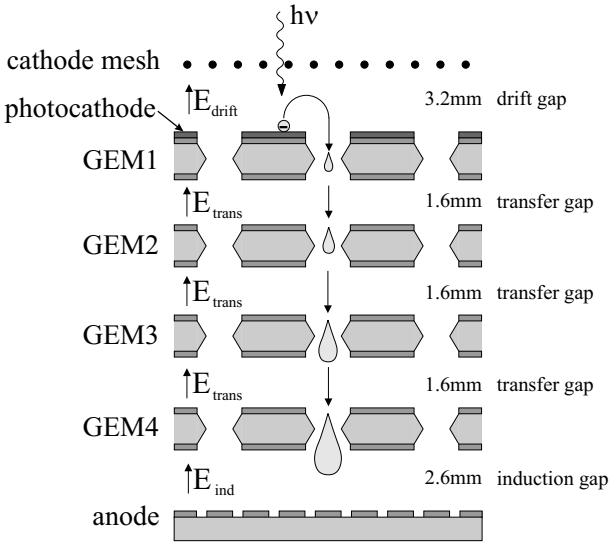

Fig. 4.1: Schematic illustration of a 4-GEM GPM, having a reflective photocathode evaporated on the top face of GEM1. Typical distances and the electric field designations are indicated.

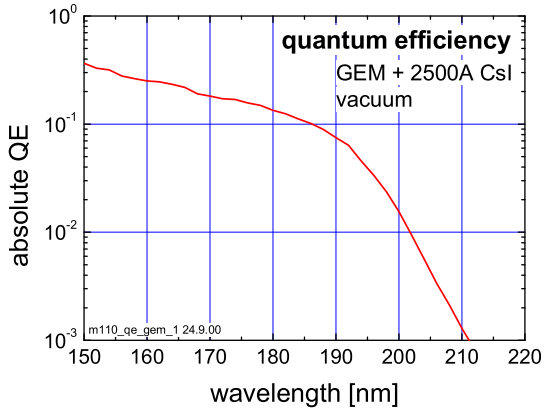

Fig. 4.2: The absolute quantum efficiency of a 2500 Å thick CsI photocathode deposited on a dc140 GEM face measured in vacuum. The photocathode covers 77% of the illuminated area.

~30–100 kV/cm and undergo gas amplification. The avalanche process for single photoelectrons results in Polya pulse-height distributions (see Sec. 3.7.2); therefore, a large fraction of the photoelectrons experience only a small multiplication. For these events only a small number of electrons arrives at the GEM-hole exit.

c) As electron losses to the bottom-GEM electrode are inevitable (see Sec. 2.7.3), there are events in which all avalanche-electrons are lost and do not reach the subsequent

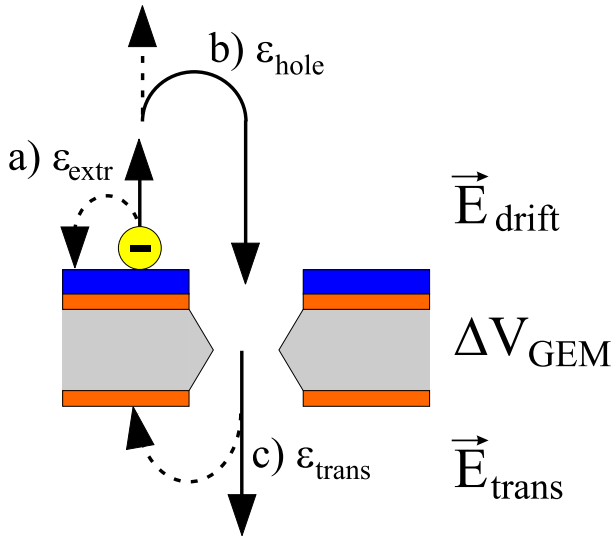

Fig. 4.3: Photoelectrons emitted from a reflective photocathode on top of a GEM electrode are a) extracted from the photocathode with an efficiency ϵ_{extr}, b) guided into the GEM apertures with an efficiency ϵ_{hole}. c) A fraction of the avalanche electrons is extracted and transferred into a following element with an efficiency ϵ_{trans}; another fraction is lost to the bottom-GEM electrode. ϵ_{trans} is unity, if at least a fraction of the avalanche charge is transferred to the next stage and the event is detected.

GEM stage. Thus ϵ_{trans}, the probability that at least a fraction of the event charge is transferred to the next multiplier stage and the event is recorded on the anode, may not be large. In fact, this loss mechanism is particularly critical in the case of single-photoelectron detection due to avalanche fluctuations discussed above. On the contrary, for a large number of primary photoelectrons, the electron avalanche size is always large and the probability of total event loss due to electron losses to the bottom-GEM electrode is negligible, even at moderate multiplication, resulting in ϵ_{trans} values close to unity.

The single-photoelectron detection efficiency can thus be described as:

$$\epsilon_{det} = \epsilon_{extr} \cdot \epsilon_{hole} \cdot \epsilon_{trans} \tag{4.1}$$

For convenience we also define a *photoelectron collection efficiency*, ϵ_{coll}; it is the efficiency whereby photoelectrons are extracted from the photocathode and guided into the GEM apertures:

$$\epsilon_{coll} = \epsilon_{extr} \cdot \epsilon_{hole} \tag{4.2}$$

4.2.1 Experimental setup and methodology

Our principal aim was to measure the *absolute* single-electron detection efficiency. It was realized by recording UV-induced single-electron pulses from a photocathode deposited on a GEM (Fig. 4.4) and using their yield for deriving the various electron transport efficiencies defined in Sec. 4.2. This method is very different from the approach based on DC current measurements [84, 97]. As explained above, resulting from the statistical fluctuations in the amplification process of single electrons, many events have only a small number of electrons at the GEM hole exit. DC current measurements are not sensitive to the loss of single

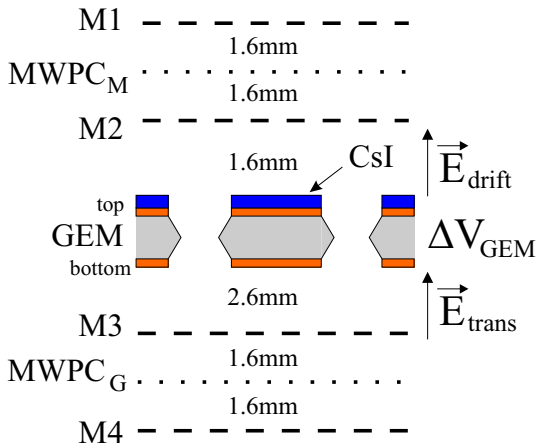

Fig. 4.4: The experimental setup used for measuring the single-photoelectron detection efficiency, consisting of a CsI-coated GEM, sandwiched between two MWPC amplification elements.

photoelectrons or to events with small gain, as their contribution to the total current is negligible when the detector is operated in multiplication mode. Under these conditions, the only way to assess the single-electron detection efficiency ϵ_{det}, is by single-electron pulse counting. Current mode measurements provide valid results for single photoelectron transport only if the detector is operated at unity gain. In these conditions, currents measured on the detector electrodes are due to transfer of the primary photoelectrons only, and thus provide an unambiguous tool for evaluation of the charge transfer process.

We found it convenient to measure ϵ_{det} by comparing the pulse-counting rate from the GEM-GPM with reflective CsI to the one measured with a multiwire GPM known to have ϵ_{det}=1 and having the same photocathode illuminated by the same light source. Fig. 4.4 shows the experimental setup consisting of a GEM foil, whose top side is evaporated with CsI, sandwiched between two MWPC detectors. The detector was realized with standard $30\times30\text{mm}^2$ elements on G10 frames; details can be found in Secs. 3.6.1 and 3.6.2.

Measurements to pinpoint the photoelectron transfer through the GEM and to assess the photoelectron detection efficiency were carried out both in current-mode and pulse counting-mode. The various electrical connection schemes are shown in Fig. 4.5. By a proper choice of potentials, four operation modes are possible: GEM counting mode, MWPC counting mode, GEM current mode and MWPC current mode.

In the *GEM counting mode*, photoelectrons released from the photocathode are guided into the GEM holes and are further transferred to the MWPC_G structure, where they are further multiplied and recorded. Measurements in the *MWPC counting mode* are used for normalizing the GEM-mode results. The CsI coated face of the GEM acts simply as a reflective photocathode with the uncoated face kept at the same potential. Emitted photoelectrons are multiplied and detected by the MWPC_M structure, with ϵ_{det}=1.

In both cases the detectors operate at equal total gains and the ratio of the number of detected *events*, with equal electronic thresholds, provides the GEM's detection efficiency. The advantage of this approach is the possibility for a direct evaluation of the efficiency of extracting electrons from the photocathode and transferring them into the GEM apertures and further towards the following multiplying element. In both modes, the MWPC provides the main electron amplification for the detection.

In the *MWPC current mode* the photocurrent is measured on the mesh M2, with a negative potential applied to the interconnected GEM electrodes (see Fig. 4.5a). The drift field, E_{drift}, extracts the photoelectrons and guides them to the mesh M2. As can be seen in Fig. 4.6, the current I_{MWPC} rises fast with E_{drift} and then saturates. This behaviour reflects the drop of photoelectron backscattering with increasing fields. Higher drift fields further reduce electron backscattering and result in a slowly increasing I_{MWPC}. For normalization of the current measurement in the GEM-mode, the value of I_{MWPC} at 3 kV/cm was chosen. This seemingly arbitrary choice can be justified by the fact that photocurrents above that value rise very moderately in all gases investigated. Higher drift-field values are not recommended as they will lead to photoelectron losses when these are transmitted to the MWPC through the mesh M2 (from high to low fields).

In the *GEM current mode* the current I_{GEM} was measured on the interconnected GEM bottom and M3 electrodes while a negative potential was applied to the top-GEM electrode (Fig. 4.5b). The GEM voltage, ΔV_{GEM}, extracts the electrons from the photocathode and

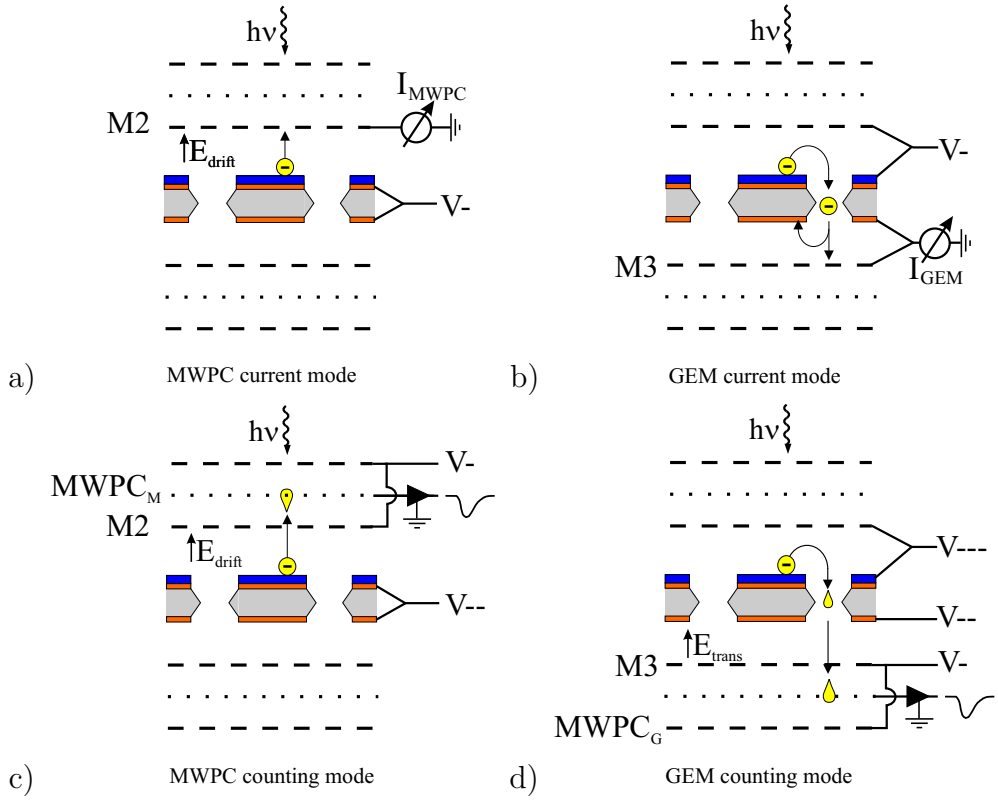

Fig. 4.5: The electrical connection schemes of the setup: a) MWPC current mode, b) GEM current mode, c) MWPC counting mode and d) GEM counting mode.

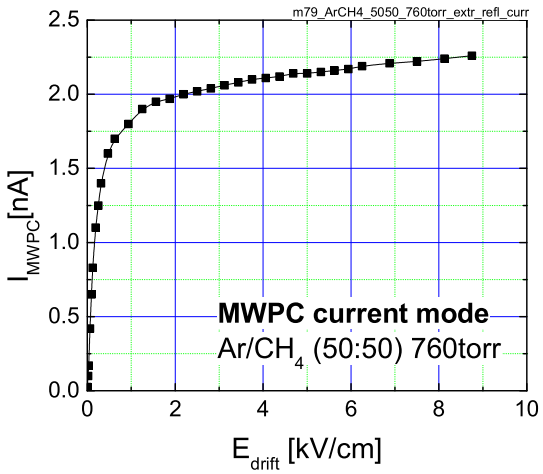

Fig. 4.6: Photocurrent measured on the mesh M2 in the MWPC current-mode in Ar/CH_4 (50:50).

guides them into the GEM holes. The transferred current I_{GEM}, normalized to I_{MWPC} measured in the MWPC current mode provides an unambiguous measure of the collection efficiency, ϵ_{coll}.

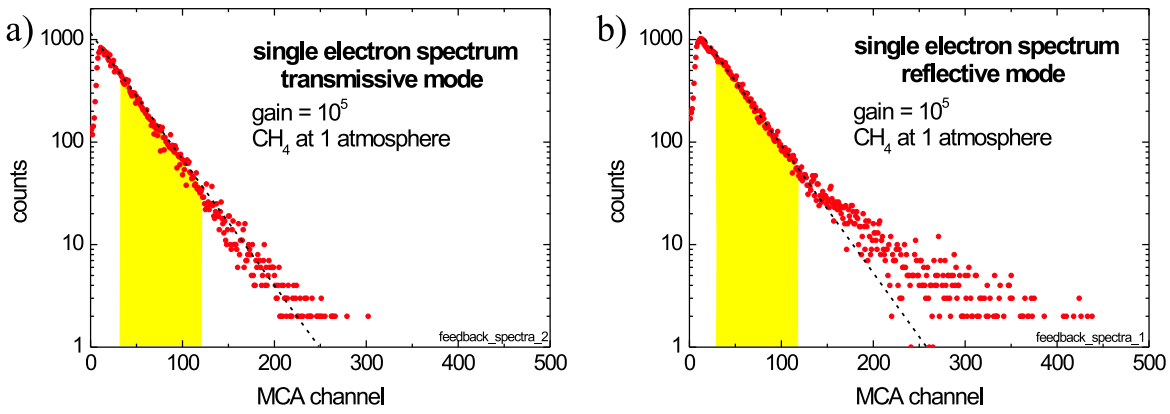

Fig. 4.7: Single-electron pulse-height spectra measured in a) GEM-mode (Fig. 4.5d, V_{GEM}= 510 V, E_{drift}=0, E_{trans}= 5 kV/cm) and b) MWPC-mode (Fig. 4.5c, E_{drift}= 3 kV/cm) in CH_4 at atmospheric pressure. The areas under which the event yields are measured are indicated.

In gas multiplication conditions, single-photoelectron pulse counting is the only reliable way of measuring the single-electron detection efficiency. Here, the counting rates in GEM and MWPC modes are measured. In the MWPC mode, the photoelectrons are extracted by the drift field E_{drift}, transferred through the mesh M2 and multiplied on the wires of $MWPC_M$. In the GEM mode, photoelectrons are guided into the GEM holes where they experience a first multiplication. The multiplied charge is then transferred in the transfer field E_{trans} to the second amplification stage in the $MWPC_G$. To permit a comparison of the counting rates, the overall gains in the two operating modes (GEM and MWPC) were held constant and equal (at approximately 10^5); it was done by adjusting the MWPC voltages, keeping the slopes of the single-electron spectra equal. In order to minimize possible errors due to electronic noise contribution (lower end of the spectrum) or to feedback effects (higher end), only the middle part of each spectrum was integrated (see Fig. 4.7) to provide the yield of counted events. The photon feedback clearly appears as an enhanced tail of the exponential distribution in the MWPC-mode (Fig. 4.7b). The absence of excess pulses in the tail of the GEM-mode spectrum (Fig. 4.7a), taken under the same total gain, clearly indicates the effective avalanche-photon screening of the photocathode, provided by the GEM.

The ratio of the event yields recorded in the GEM- and MWPC-modes defines a "practical" single-electron detection efficiency ϵ_{det}. This experimental technique relies on the exponential shape of the single-electron spectra for adjusting equal conditions in both MWPC and GEM mode. In conditions, where saturation or feedback effects yield spectra that deviate significantly from the exponential, this method is no longer applicable.

4.2.2 Role of the electric fields

The electric fields configuration in the detector is the main factor influencing the single-photoelectron detection efficiency, as it is responsible for the efficient photoelectron extrac-

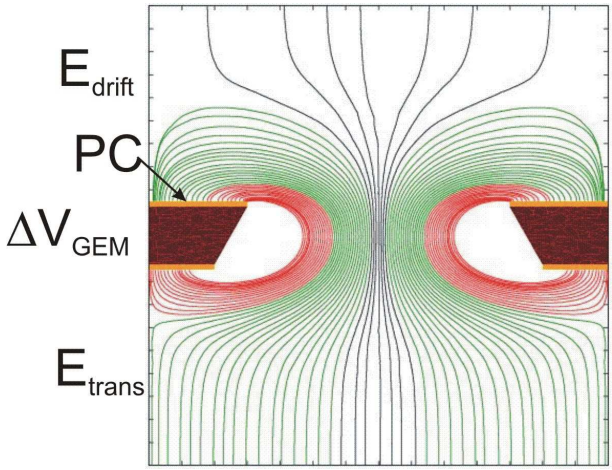

Fig. 4.8: Simulated electron drift lines in atmospheric CH_4, for photoelectrons leaving the photocathode (PC) evaporated on the top face of a sc50 GEM. The drift field is zero, the transfer field is 3 kV/cm and ΔV_{GEM}= 400 V.

tion from the photocathode, its focusing into the GEM holes and the efficient extraction of a fraction of the avalanche charge from the first GEM to the following multiplier stage. This section describes how the various detector potentials influence the relevant efficiencies.

The figures in this section were not chosen systematically but rather according to how well they illustrated the discussed effects. Therefore, the GEM geometry and the gas mixture vary among the figures presented. A systematic discussion of the influence of the GEM geometry and the gas mixture follows in Secs. 4.2.3 and 4.2.4, respectively.

Role of the GEM potential ΔV_{GEM}

The potential difference across the GEM, ΔV_{GEM}, has two effects on the single-electron detection efficiency. Firstly, it establishes an electric field on the top-GEM surface, permitting efficient extraction of photoelectrons from the photocathode and guiding them into the GEM holes. Fig. 4.8 illustrates this point, showing simulated electron drift paths on a sc50 GEM (Tab. 2.1) for ΔV_{GEM}=500 V. Secondly, photoelectrons entering the GEM apertures experience gas multiplication in the strong electric fields within the holes, resulting in a exponentially-distributed number of electrons at the hole exit. The influence of the GEM gain on the single-photoelectron detection efficiency can only be measured in pulse-counting mode and is discussed further down.

The electric field created at the top-GEM surface by the GEM potential is not homogeneous, as can be seen in Fig. 4.9. The highest electric field is encountered at the hole circumference and drops strongly towards the center between the holes; its value at the center is ∼1.5 kV/cm for ΔV_{GEM}=300 V.

Fig. 4.10 shows the electric field strength variation along the dashed line of Fig. 4.9, between neighbouring holes for three different values of ΔV_{GEM}. At ΔV_{GEM}= 500 V, the field strength (E > 2.5 kV/cm) is sufficiently high all over the surface to minimize backscattering in most gases (for comparison see Fig. 2.7).

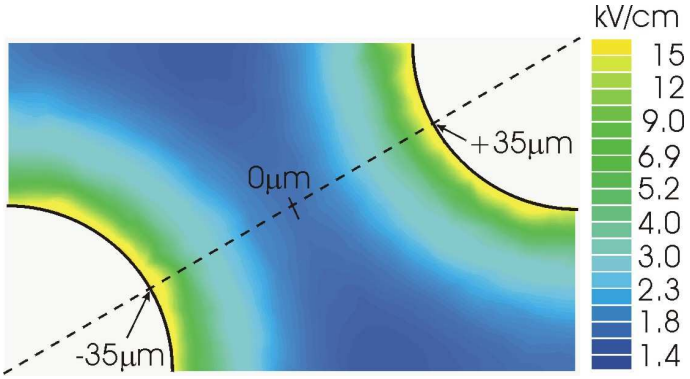

Fig. 4.9: The electric field strength at the top-GEM surface of a dc140 GEM, operated at ΔV_{GEM}= 300 V. The field is higher close to the holes and drops towards the center. The variation of the field strength along the dashed line is plotted in Fig. 4.10.

The photocurrent versus GEM voltage of a dc140 GEM in atmospheric CH_4, depicting the collection efficiency, ϵ_{coll}, is shown in Fig. 4.11. One can remark that already for a value of ΔV_{GEM} = 100 V more than 80% of the photoelectrons are extracted from the photocathode and transferred into the GEM holes. For ΔV_{GEM} values above ∼130 V, multiplication in the GEM holes makes the measurement in current mode irrelevant for deriving ϵ_{coll}.

Role of the drift field E_{drift}

The drift field E_{drift}, defined by the potential difference between the top GEM and the electrode mesh M2 (see. Fig. 4.4), modifies the electric field created by the GEM potential at the vicinity of the photocathode. Its influence on the collection efficiency can be seen in Fig. 4.12, showing the variation of the current measured in the GEM-mode, I_{GEM}, as a function of E_{drift} for a sc50 GEM operated in atmospheric Ar/CH_4 (20:80) at ΔV_{GEM}= 200 V. In

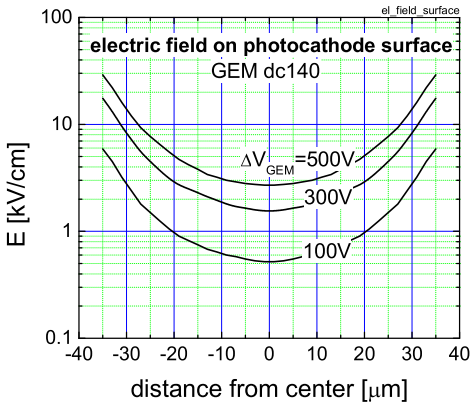

Fig. 4.10: The electric field strength at the surface of a sc140 GEM, along the dashed line shown in Fig. 4.9.

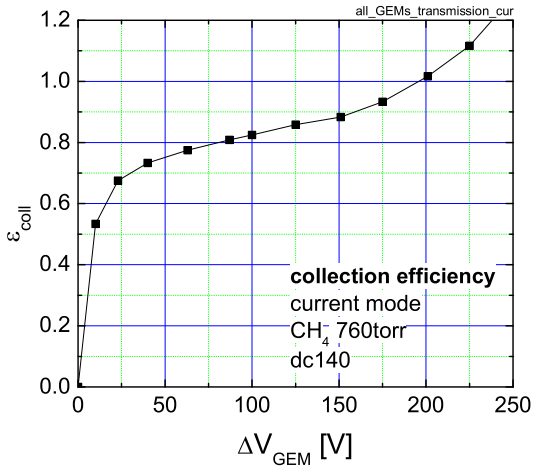

Fig. 4.11: The electron collection efficiency of a dc140 GEM operated in atmospheric CH_4, measured in current mode. The value of ϵ_{coll} is only valid for $\Delta V_{GEM} < 130$ V, due to the onset of multiplication in the GEM apertures.

addition to I_{GEM}, we also measured the current on the photocathode, I_{pc}; it has opposite polarity than I_{GEM}, as it corresponds to the flow of photoelectrons leaving the photocathode, but for an easier comparison, only the absolute values of the currents are plotted. The maximal value of I_{GEM} is reached when the detector is operated with E_{drift}=0. For both negative and positive E_{drift} values, the current on the GEM I_{GEM} drops considerably, and therefore also the collection efficiency ϵ_{coll}. In the case of positive drift field values, the electric field strength on the photocathode is reduced, resulting in higher backscattering and a lower extraction efficiency, ϵ_{extr}. The simultaneous drop of the photocathode current I_{pc} confirms this interpretation. In the case of negative drift field values, increasing the electric field strength at the photocathode surface, the photocurrent I_{pc} increases slightly due to reduced backscattering and thus increased extraction efficiency ϵ_{extr}. But a large fraction of the extracted photoelectrons are collected on mesh M2 above the photocathode rather than being transferred into the GEM holes, resulting in a smaller ϵ_{hole} and the observed drop in I_{GEM}.

In pulse-counting mode, the counting-rate measured in the GEM-mode shows the same behaviour: it has its maximum for $E_{drift} = 0$, as can be seen in Fig. 4.13 for a dc140 GEM operated in Ar/CH_4 (50:50) at $\Delta V_{GEM} = 350$ V. The width of the distribution in this case is much larger than in the previous figure. A slightly different gas mixture was used, but the higher value of ΔV_{GEM} used is mainly responsible for this effect, diminishing the influence of the drift field. For still higher ΔV_{GEM} values, the influence of E_{drift} is expected to be even smaller.

Since the optimal operation of the detector is for E_{drift}=0, the electric field configuration on the photocathode is determined only by the GEM potential. Therefore, in all subsequent measurements the potentials were chosen to have E_{drift}=0.

Roles of the transfer field and GEM gain

Electrons leaving the first multiplying stage are extracted and *transferred* to the following multiplying stage by the transfer field E_{trans}; in our case it is defined as the potential difference between the bottom-GEM electrode and mesh M3 of the MWPC$_G$ (see Fig. 4.4). As was discussed above (Sec. 2.7.3), in GEM multipliers a fraction of the avalanche electrons is lost, being collected on the bottom-GEM electrode. The fraction of the extracted charge depends approximately linearly on the transfer field E_{trans}. To confirm this behaviour, the current measurement setup described in Sec. 4.2.1 was slightly modified by individually powering the bottom-GEM and M3 electrodes, thus allowing for varying E_{trans} values. The currents on all electrodes were recorded: the transfer current I_{trans} on mesh M3, the current on the

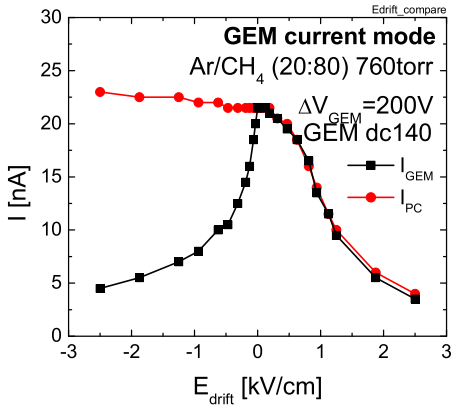

Fig. 4.12: The currents measured in the GEM configuration of Fig. 4.5b, versus the drift field, depicting the influence of the E_{drift} on the photoelectron transfer from the photocathode into the GEM holes. The measurements were performed with a dc140 GEM at ΔV_{GEM}=200V in atmospheric Ar/CH$_4$ (20:80). The absolute values of the currents are plotted (see text).

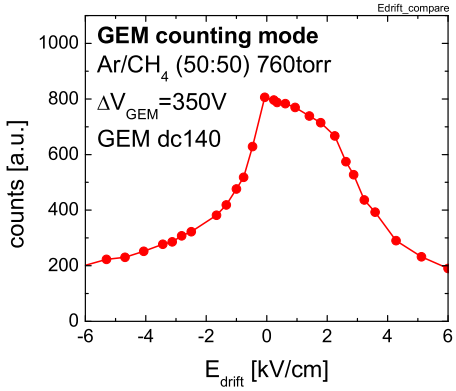

Fig. 4.13: Influence of the drift field measured in pulse-counting mode for a dc140 GEM at ΔV_{GEM}=350V in atmospheric Ar/CH$_4$ (50:50).

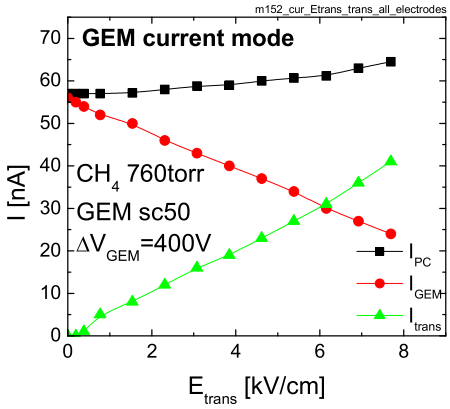

Fig. 4.14: Influence of E_{trans} on the charge extraction from the GEM holes for constant ΔV_{GEM}=400V, measured on a sc50 GEM in atmospheric CH_4.

bottom-GEM electrode I_{GEM} and the current on the photocathode I_{PC}, interconnected with mesh M2. I_{PC} has an opposite polarity to the other two currents, corresponding to electrons leaving the photocathode and, in the case of amplification, also to the collection of ions generated in the avalanche process. The sum of all three currents is zero. For clarity of presentation, only the absolute values of the currents are plotted in Fig. 4.14. The measurement was performed in atmospheric CH_4 with a sc50 GEM (Table 2.1) at ΔV_{GEM}=400V. The higher the transfer field, the larger the charge which is extracted from the GEM towards M3, explaining the increasing I_{trans} and the dropping I_{GEM}. The slight increase of I_{PC} with E_{trans} can be explained by a small gain increase in the GEM caused by the higher transfer field [96].

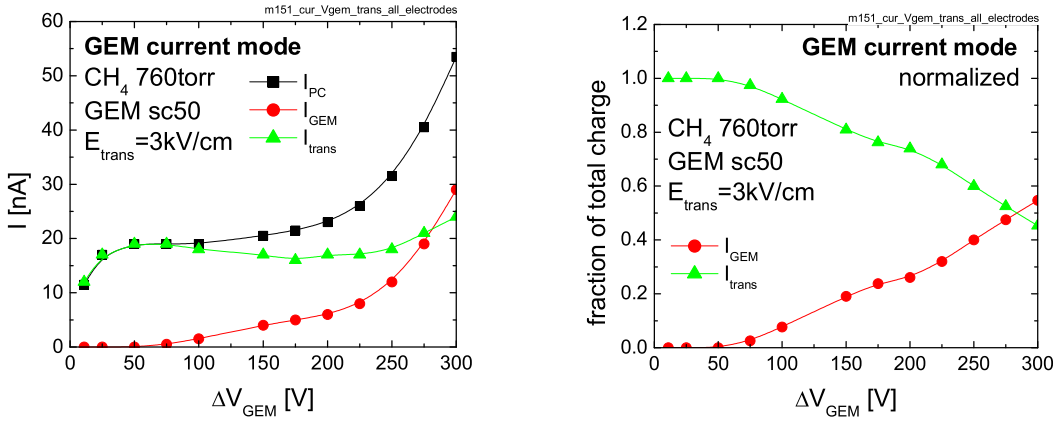

a) b)

Fig. 4.15: a) The variation of the detector currents as a function of ΔV_{GEM} measured with a sc50 GEM in atmospheric CH_4 for a constant E_{trans} and b) normalized to the photocathode current I_{PC}.

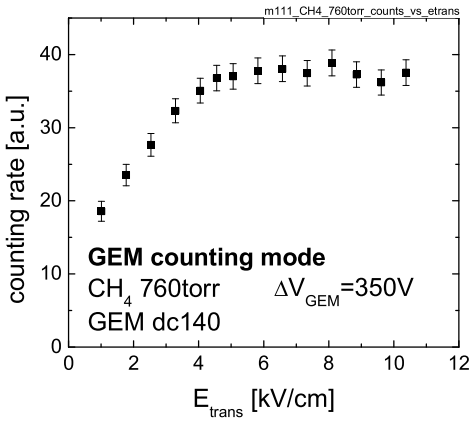

Fig. 4.16: The counting rate measured in the GEM counting mode (configuration of Fig. 4.5d as a function of E_{trans} in atmospheric CH_4 with a dc140 GEM at ΔV_{GEM}=350 V. The pulse-height (total gain) is kept constant, when varying E_{trans}. The counting rate increases up to $\sim$4 kV/cm, due to increasing electron extraction from the GEM holes. No drop in counting rate is observed for higher transfer fields.

For higher ΔV_{GEM} values, higher transfer fields are required to overcome the GEM field and to extract the same charge fraction form the GEM holes. This can be seen in Fig. 4.15a, showing the transferred current I_{trans}, the current on the bottom-GEM electrode I_{GEM} and the photocathode current I_{PC}, as function of ΔV_{GEM}, measured at atmospheric CH_4 on a sc50 GEM with a constant transfer field E_{trans}=3 kV/cm. Up to $\Delta V_{GEM}\sim$150 V the measured currents are due only to transfer of photoelectrons; for higher GEM voltages amplification in the GEM holes starts, resulting in a fast rise of the currents with increasing ΔV_{GEM}. In Fig. 4.15b, showing I_{trans} and I_{GEM} normalized to I_{PC}, the influence of ΔV_{GEM} on the charge transfer can be seen more clearly: for $\Delta V_{GEM}\sim$100 V, the transfer field is strong enough to extract almost all electrons from the GEM holes. For higher GEM potentials, I_{trans} drops and I_{GEM} increases, as the relative strength of the transfer field decreases compared to the GEM field. Therefore, higher values of E_{trans} have to be chosen, in order to extract a large fraction of the avalanche charge from the GEM and transfer it to the next amplification stage.

However, as was discussed in Sec. 2.7.3, high transfer fields in multi-GEM detectors result in electron losses at the top electrode of the the following GEM stage resulting in a decreasing electron transmission. In our measurements in pulse-counting mode, where the second stage is a MWPC, this effect was not observed (Fig. 4.16). We attribute this to the higher electron transparency of the mesh M3 compared to that of a GEM. Nevertheless, for our multi-GEM GPM application, transfer field values of 3–4 kV/cm were chosen in further experiments, providing a good charge transfer into a second stage GEM in multi-GEM detectors [84].

The single-photoelectron detection efficiency ϵ_{det} is shown in Fig. 4.17 as a function of ΔV_{GEM} for three different transfer field values; it further demonstrates the importance to operate with high transfer fields. As expected, the highest transfer field applied E_{trans}=3.8 kV/cm yields the best result, reaching maximum single-electron detection efficiency already at ΔV_{GEM}=400 V. For a smaller transfer field of E_{trans}=1.9 kV/cm, full photoelectron de-

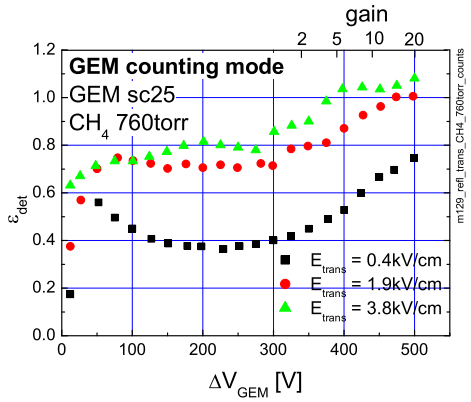

Fig. 4.17: The single electron detection efficiency ϵ_{det} as a function of ΔV_{GEM}. The measurement was performed with a sc25 GEM in atmospheric CH_4 for 3 different transfer fields values.

tection efficiency is reached at higher ΔV_{GEM} values. For a very small transfer field of E_{trans}=0.4 kV/cm, the efficiency drops with increasing ΔV_{GEM} due to the above described effect of higher charge losses to the bottom-GEM electrode; it increases at higher ΔV_{GEM} values but does not reach unity.

In all three cases the detection efficiency increases once the GEM field is sufficiently high for gas multiplication, above $\Delta V_{GEM} \sim 300$ V. Although the transferred charge fraction for each event decreases with increasing ΔV_{GEM} values, the average avalanche size increases and the GEM gain compensates losses; assuring that at least a fraction of the avalanche charge is transferred to the successive multiplication stage and a unity transfer efficiency is accomplished. The upper scale in Fig. 4.17 shows the gain corresponding to the GEM voltage shown on the bottom scale. As the charge fraction lost to the bottom-GEM electrode is higher for lower transfer fields, the gain required for compensating for these losses is also higher. Therefore it is advisable to operate the detector with high transfer field values for reaching high single-photoelectron detection efficiencies even at modest gains of the GEM carrying the photocathode.

4.2.3 Influence of the GEM geometry

GEMs with different geometries were investigated (Tab. 2.1) for assessing the impact on the single-photoelectron detection efficiency, ϵ_{det} by changing the following parameters (with respect to the standard GEM geometry dc140): the pitch (dc200), the hole diameter (dc100), the hole shape (sc50, sc25) and the GEM thickness (sc25).

The most obvious impact of the GEM geometry is the effective surface area for photocathode deposition. This varies in our case from 89% to 53% for the dc200 and dc100 geometries respectively; the standard GEM (dc140) has an active surface of 77%. Maximising the available photocathode surface favours GEMs with a small hole-to-total-area aspect ratio. On the other hand, as was discussed in Sec. 4.2.2, high electric field strength on the photocathode surface is required to overcome photoelectron backscattering and to guide the electrons into

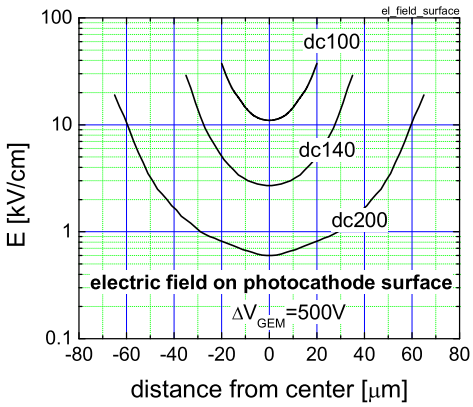

Fig. 4.18: The influence of GEM geometry on the electric field strength at the photocathode surface for ΔV_{GEM}=500V, plotted along the line shown in Fig. 4.10 for three GEM geometries: dc200, dc140 and dc100. The field is plotted versus the distance from the axis between two adjacent holes.

the GEM holes, which favors a high hole-to-total-area aspect ratio. This is demonstrated by the simulation results in Fig. 4.18; it shows the variation of the electric field strength over the photocathode area for constant ΔV_{GEM}=500 V for three GEM geometries dc200, dc140 and dc100. As expected, the dc200 geometry shows the lowest and dc100 the highest electric field strength over the photocathode surface.

The current-mode measurement of the collection efficiency ϵ_{coll}, presented in Fig. 4.19, confirms this expectation. With the dc100 GEM, almost full collection efficiency was reached at $\Delta V_{GEM} \sim 100$ V, while for the dc200 geometry only $\sim 50\%$ of the photoelectrons were collected at the same GEM voltage due to the difference in electric field strength on the photocathode surface. Again, the dc140 standard GEM geometry results fall in-between that of the dc100 and dc200 GEMs, reaching 80% efficiency at $\Delta V_{GEM} = 100$ V. In addition, the results for the two remaining geometries sc50 and sc25 are also shown. The difference in collection efficiency of these two, compared to that of the dc140 GEM, despite the same hole-to-total-area ratio, is attributed to the different hole shape and in the case of sc25, also to the GEM thickness. A higher collection efficiency is observed for the sc25 GEM, compared to that of the dc140 and sc50; it can be explained by the thinner (25 μm) Kapton foil of the sc25 GEM, resulting in higher field strengths at the photocathode surface for the same ΔV_{GEM}, reducing the photoelectron backscattering in gas. A somewhat lower field on the photocathode surface for GEMs with conical holes, is probably responsible for the slightly lower collection efficiency of the sc50 GEM.

For all GEM geometries, with the exception of dc200, collection efficiencies ϵ_{coll} exceeding 80% were reached before gas amplification sets in at ~ 100 V and where current measurements are no longer valid.

As was discussed in Sec. 4.2.2, the transfer efficiency ϵ_{trans} has a strong influence on the single photoelectron detection efficiency. The charge loss to the bottom-GEM electrode can be modified by the hole shape. GEMs with conical holes operated with the large hole

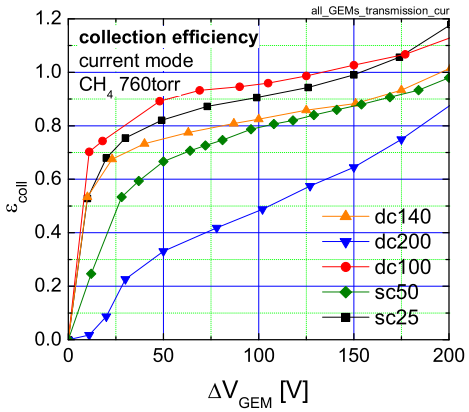

Fig. 4.19: The collection efficiency measured in current-mode in atmospheric CH_4 different GEM geometries. Values of ϵ_{coll} above $\Delta V_{GEM} \sim 100$ V are not meaningful, due to the onset of amplification in the GEM.

opening facing the transfer region, show considerably lower electron losses to the bottom-GEM electrode compared to the standard double-conical ones. This effect is demonstrated in Fig. 4.20, showing the single-photoelectron detection efficiency, ϵ_{det}, as a function of ΔV_{GEM}, measured in pulse-counting mode in atmospheric CH_4. Both GEMs with conical holes, sc25 and sc50 show higher single-photoelectron detection efficiency than the standard GEM. This can only be due to a higher transfer efficiency ϵ_{trans}, as the collection efficiency of these GEMs is comparable to that of the standard GEM geometry (see Fig. 4.19). Even the dc100 geometry with its double-conical holes, exhibiting the highest collection efficiency as shown above, has a lower overall detection efficiency, due to a small transfer efficiency.

Surprisingly, all five GEM geometries investigated exhibit practically the same gain-voltage characteristics in CH_4 as shown in Fig. 4.21. The sc25 GEM proved to be particularly fragile in operation, probably due to the thin (25 μm) insulator; a single discharge would

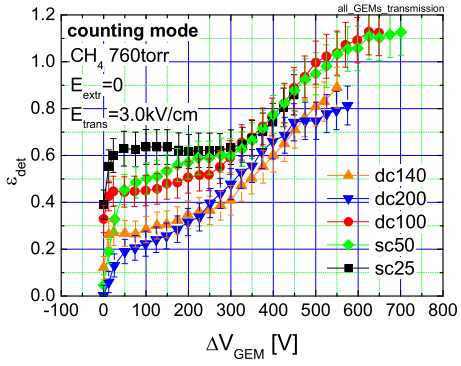

Fig. 4.20: The single-photoelectron detection efficiency as a function of ΔV_{GEM} for the different geometries investigated.

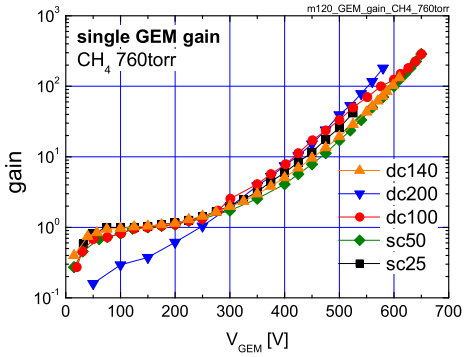

Fig. 4.21: The absolute single-GEM gain measured in current mode at atmospheric CH_4, for different GEM geometries.

cause permanent damage to the GEM, preventing further operation, while the other GEMs could withstand several discharges without noticeable degradation. This rather limits the use of the sc25 GEM geometry, unless operated at relatively low gains, where its higher ϵ_{det} is of attraction (Fig. 4.20).

Maximal detection efficiency was reached at $\Delta V_{GEM} \sim 600$ V with the dc100 and the sc50 GEM geometries, corresponding to a gain of ∼100. Even with the standard GEM geometry sc140, a single-photoelectron detection efficiency of ∼90% was reached at ΔV_{GEM}=550 V.

Besides the obvious influence of the geometry on the effective photocathode's surface area, the strongest influence on the single-electron detection efficiency is due to the hole shape. The improved transfer efficiency of GEMs with single-conical holes, could advocate for their use as a first-stage in multi-GEM GPMs with reflective photocathodes. However, reports pointing to an enhanced up-charging of these GEMs, due to the larger surface of insulator in the holes exposed to the back-drifting avalanche ions, have to be considered [83, 84].

4.2.4 Role of the gas composition

The choice of the gas mixture influences the detector operation in various ways. Firstly, operation voltages vary considerably for different gases, as reflected in the gain curves in Fig. 4.22. For example, CH_4 and CF_4 require much higher operation voltages compared to Ar/CH_4 (95:5). CH_4 is often used in MWPC-based GPMs, providing stable operation [20]; it has very low photoelectron backscattering, which yields high effective QE values. Ar/CH_4 (95:5) is our current gas mixture of choice for operation of sealed GPMs with visible-sensitive photocathodes [130, 122], the main reasons being low operating voltages, stable operation with reduced secondary effects, relatively low electron-backscattering and a small fraction of organic quencher. The second Ar/CH_4 mixture of (20:80) was investigated in an attempt to further reduce backscattering and keep the operation voltages relatively low.

CF_4 is of strong interest for windowless Cherenkov detectors, including Ring Imaging Cherenkov detectors (RICH), where the radiator gas is also the counting gas [65, 97]. In pure CF_4 the technique of obtaining the single electron detection efficiency from their spectra in

MWPC and GEM mode was not applicable. Very strong photon-mediated secondary effects caused by gas scintillation light and avalanche-photon feedback strongly limited the gain in MWPC, which prevented us from performing the usual normalization measurements in in MWPC mode. Instead, the pulse-counting rate in the MWPC mode was measured in pure CH_4 and its value used for normalizing the CF_4 results obtained in the GEM-mode. No problems in operation occurred in GEM mode operation in pure CF_4, due to the suppression of photon feedback and high and stable gains can be reached (Fig. 4.22). The absence of photon feedback, permitted reaching high gain operation in pure CF_4 also in cascaded multi-GEM detectors coupled to semi-transparent photocathodes [65] and allowed for the operation of such detectors at high gains also in noble gas mixtures [112]. As will be shown below, gains exceeding 10^6 were reached in atmospheric CF_4 in cascaded GEMs with reflective CsI photocathodes (Fig. 4.25).

The different operation voltages for the different gas mixtures have several consequences: on one hand, higher GEM potentials increase the electric field at the photocathode surface and therefore reduce photoelectron backscattering in the gas. On the other hand, for fixed transfer fields E_{trans}, electron losses at the hole exit are larger for high ΔV_{GEM} values, which tends to decrease ϵ_{trans}, as was discussed in Sec. 4.2.2. The latter can be compensated by increasing the gain of GEM1.

As was mentioned before, electron backscattering to the photocathode varies considerably with the gas mixture (see Fig. 2.7) [112, 65, 63]. While CF_4 and CH_4 have the highest known extraction efficiency even at moderate field strengths ($\sim$90% at 1 kV/cm [65]), in Ar/CH_4 (95:5) an extraction of only $\sim$70% can be reached at equal field strengths. Electron extraction in noble gases and their mixtures is more difficult at moderate fields [63, 64]. This difference in backscattering manifests itself in the different collection efficiencies presented in Fig. 4.23 for a sc50 GEM geometry. The three gases with low backscattering CF_4, CH_4 and Ar/CH_4 (20:80) show a collection efficiency of $\sim$70% or more at ΔV_{GEM}=50 V, while for Ar/CH_4 (95:5) the higher backscattering results in a extraction efficiency of only 25% at equal GEM potential. The early onset of amplification in the GEM holes in the case of Ar/CH_4 (95:5) results in an unreliable measurement of ϵ_{coll} in current mode for ΔV_{GEM} higher than $\sim$50 V.

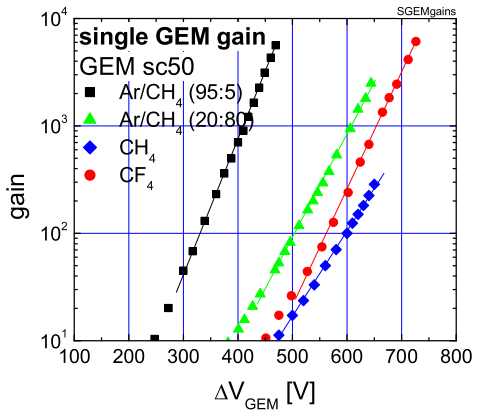

Fig. 4.22: Single GEM gain curves of a sc50 GEM operated in different gas mixtures.

Nevertheless full single-electron detection efficiency was obtained for all four gases, demonstrated in Fig. 4.24. With the exception of CF_4, in which a dc140 GEM was used, the measurements were performed with a sc50 GEM. Due to the low operation voltages required, full single photoelectron detection efficiency is reached in Ar/CH_4 (95:5) already at $\Delta V_{GEM} \sim 350$ V; in the other gas mixtures: Ar/CH_4 (20:80), pure CH_4 and CF_4, the detection efficiency reaches unity values at respectively higher GEM voltages (Fig. 4.24a).

If plotted as a function of single-GEM gain (Fig. 4.24b) CH_4 and the Ar/CH_4 mixtures require only a gain of 30 and 80, respectively for reaching full detection efficiency. For Ar/CH_4 (95:5) the low operation voltage and the high backscattering require higher gains (~ 300). In CF_4 gains exceeding 10^3 were required to overcome losses to the bottom-GEM electrode and reaching full single electron detection efficiency. The operation of a dc50 GEM in CF_4 instead of a sc50 GEM does certainly contribute to the high gains required. Furthermore, one can speculated that the very low diffusion of CF_4 compared to the other gases reduces the effect of the gain on single electron detection efficiency and is responsible for the high gain values in CF_4. A similar observation of diffusion effecting single electron detection efficiency is reported in [94] for a GEM GPM with semi-transparent photocathode. Futher investigations are necessary at this point.

4.3 Gain measurements and operation of multi-GEM detectors with reflective photocathode

Following the above study, a 4-GEM GPM with reflective photocathode, schematically shown in Fig. 4.1, was assembled with standard 30×30 mm^2 elements on G10 frames and operated in the test chamber (see Sec. 3 for details). The top-most GEMs carrying the CsI photocathode had conical hole geometry (sc50 of Tab. 2.1), while the other GEM elements were of standard geometry (dc140). The voltages to the individual electrodes were supplied by a resistor network, 10 MΩ resistors establishing equal GEM potentials and transfer fields E_{trans} in each detector stage. A 22 MΩ resistor was chosen to set a strong induction field E_{ind}. The

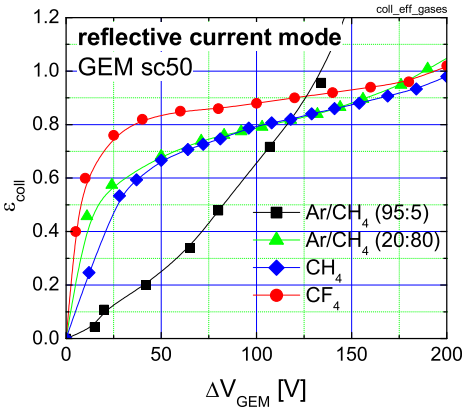

Fig. 4.23: The collection efficiency, ϵ_{coll}, measured in current mode in a sc50 GEM, in different gases.

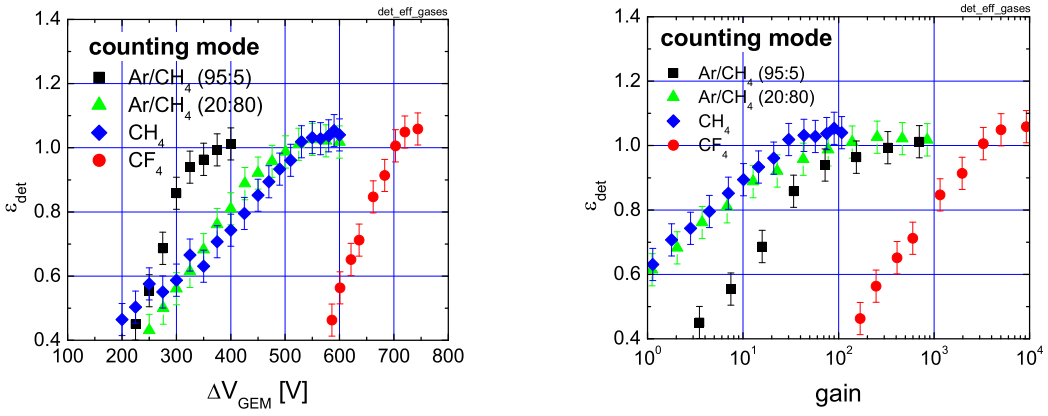

Fig. 4.24: The single-photoelectron detection efficiency in different gas mixtures. a) as a function of the GEM potential and b) as a function of the GEM gain. A sc50 GEM was used, except for CF_4, where the measurements were performed with a dc140 GEM.

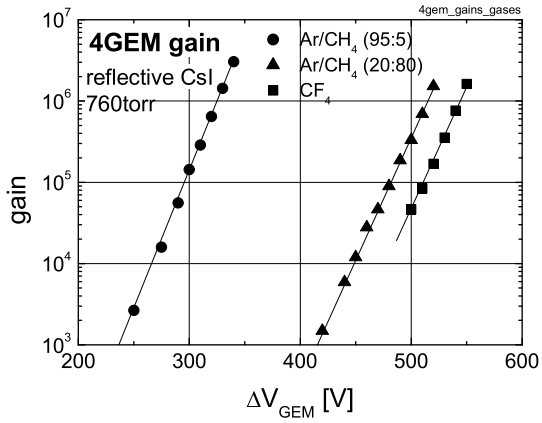

Fig. 4.25: Effective gain of a 4-GEM GPM with reflective CsI photocathode operated in different atmospheric pressure gases with equal ΔV_{GEM} values on each element.

cathode mesh and the top face of GEM1 were interconnected to assure best single electron detection efficiency.

Fig. 4.25 shows the effective gain of this detector measured in current mode (see Sec. 3.7) as a function of the GEM potential ΔV_{GEM}, set equally on all 4 GEM elements. In all three gases tested, pure CF_4 and Ar/CH_4 in the mixture ratios (95:5) and (20:80) gains exceeding 10^6 were obtained without breakdown. No photon- or ion-feedback effects were observed, which is confirmed by the absence of deviations from the exponential gain–voltage characteristics.

4.4 Time resolution

Fast and accurate timing information is required in many fields where photon detectors are employed, e.g. in time-of-flight (TOF) measurements, readout of fast scintillators and scintillating fibres, coincidence measurements, Cherenkov light detection etc. In all photon detectors the transit time of the photoelectrons from their creation point to the readout element is subject to a time jitter. The *time-transit-spread* or *time-resolution* of a detector characterizes this spread and defines the accuracy of timing measurements that can be obtained from such a system.

In GPMs, the time-resolution is determined by the fluctuations in the photoelectron transit time from their emission point at the photocathode and, after multiplication, to the anode. Obviously it depends on the detector geometry, the electric field conditions and properties of the gas composition, namely on the electron diffusion and drift velocity.

4.4.1 Experimental equipment and methodology

The detector setup, realized with standard 30×30 mm^2 G10 elements (see Sec. 3.6.1), and its signal processing scheme are schematically illustrated in Fig. 4.26, indicating also the resistor network used for powering the detector elements. To guarantee optimal photoelectron detection efficiency, the top GEM carrying the reflective CsI photocathode was of sc50 geometry (see Tab. 2.1) and the transfer field below GEM1 was chosen higher than the others. Very short photon flashes from a H_2 flash-lamp created a small number of photoelectrons on the CsI photocathode that were subsequently multiplied in the GEM holes and collected on the anode mesh. The light intensity of the H_2 flash lamp was controlled by placing optical absorbers in the light path, resulting in single photon illumination of the photocathode per flash. The trigger output signals of the flash lamp were processed by a constant fraction discriminator (CFD) to eliminate time jitter induced by pulse height fluctuations; its output provided for the *STOP* signal of the time-to-amplitude-converter (TAC)[2].

The GPM anode pulses were fed into a fast current amplifier[3] and processed by a timing-filter amplifier (TFA) and a second CFD, generating the *START* signal of the TAC. The start signal could be delayed by a selectable time. The TAC signals were measured by a multi-channel analyzer (MCA)[4]. The obtained pulse height spectrum had Gaussian shape; the width corresponding to the time-jitter of the measurement. As the light flash fluctuations can be neglected, the measured distributions provide directly the time-resolution of the detector.

In multi-photoelectron events, the drift time of individual photoelectrons is averaged. The average number of photoelectrons generated by the light flash was obtained by replacing the fast current amplifier with a charge sensitive pre-amplifier with long integration time. The pulse height of the charge signal is proportional to the number of electrons per event, a product of the number of primary photoelectrons and the detector gain. As the detector gain and the calibration of the MCA in charge units were known from previous measurements

[2] 437A, ORTEC
[3] ESN, 0.5 ns rise time
[4] MCA8000A, Amptek

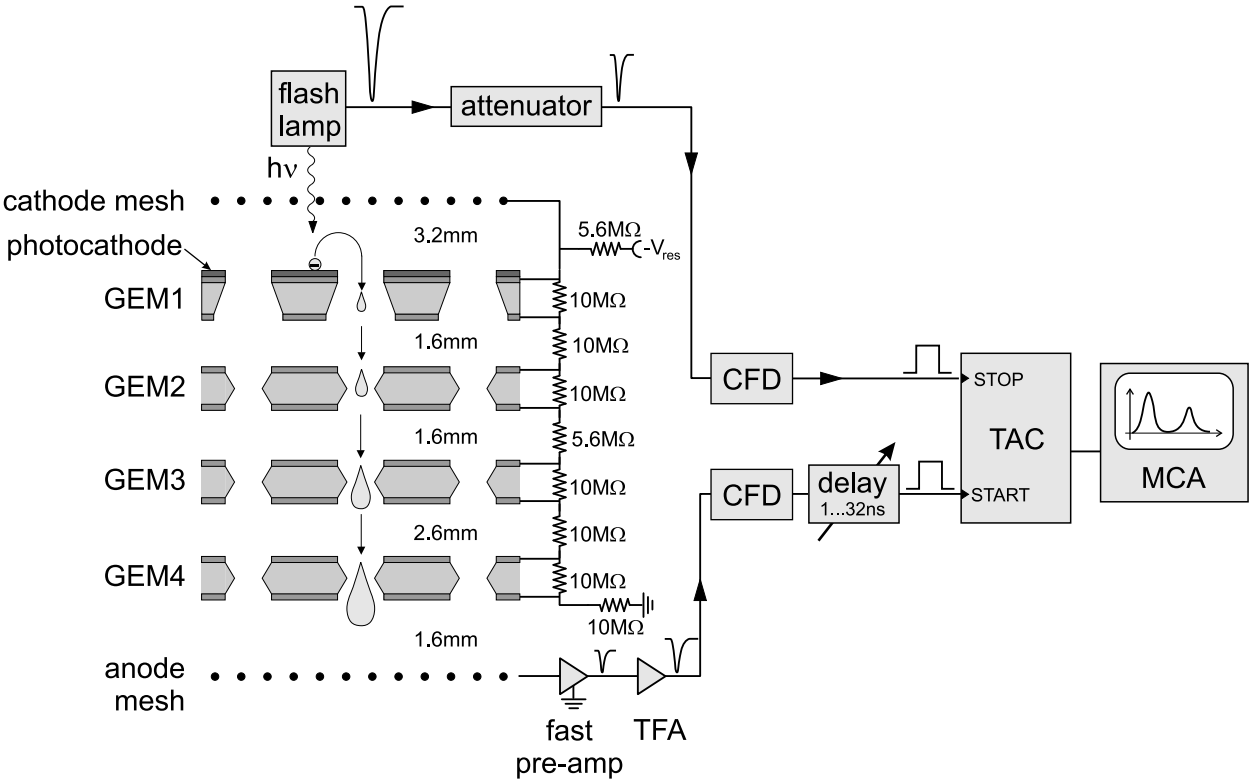

Fig. 4.26: Experimental setup for measuring the time resolution. TFA: Timing Filter Amplifier, CFD: Constant Fraction Discriminator, TAC: Time-to-Amplitude Converter, MCA: Multi-Channel Analyzer.

(see also Sec. 3.7.2), the number of primary electrons can be determined by dividing the total charge in the avalanche by the detector gain.

4.4.2 Results

An example of a single-photoelectron induced anode signal in atmospheric Ar/CH_4 (20:80), recorded with the fast current pre-amplifier, is shown in Fig. 4.27. Its rise-time of $\sim$5 ns is in good agreement with other measurements [96]; its shape is determined by the electron drift velocity and the width (1.6 mm) and field strength (2 kV/cm) in the induction gap. The signal width was found to correspond to the electron drift time from GEM4 to the anode mesh [96]. Indeed, the observed signal width of $\sim$25 ns agrees with the ratio of induction gap length and electron drift velocity (extracted from [131]) at 3.2 kV/cm: $t_{drift} \approx \frac{1.6\,mm}{6.5\,cm/\mu s} = 24.6$ ns. Faster and narrower signals can be obtained by working with a smaller induction gap and higher electric fields.

The pulse-height spectra and time resolutions obtained in CF_4 at atmospheric pressure are shown in Fig. 4.28 and Fig. 4.29 for single and $\sim$20 photoelectrons per light flash respectively. The corresponding time resolutions of σ=1.6 ns and 0.38 ns are due to the low diffusion and high electron drift velocity in CF_4 and compare well with σ=2.1 ns measured in GEM-GPMs with a semi-transparent photocathode for single-photoelectrons in the same gas [65]. The slightly better values obtained here might be due to the shorter total drift length and higher

electric fields, reducing the single electron diffusion and consequently the spread of their arrival time on the anode.

Two other gas mixtures were investigated: Ar/CH_4 (20:80) and Ar/CH_4 (95:5). They both exhibit considerably higher diffusion and slower electron drift velocities and consequently wider but lower pulses are induced on the anode. The resulting inferior signal-to-noise ratio and the relatively high noise of the fast current pre-amplifier prevented measurement of the single-electron time-resolution in these gases. Instead, the time resolution for multi-photoelectron events was measured and is shown in Fig. 4.30. In Ar/CH_4 (20:80) we obtained a time resolution of $\sigma = 0.45$ ns for ~ 40 photoelectrons when working at a gain of $2 \cdot 10^5$; in Ar/CH_4 (95:5), a time resolution of $\sigma = 0.54$ ns for 150 photoelectron events was measured at a gain of $6 \cdot 10^5$.

4.5 Discussion and conclusions on GEM-GPM operation with reflective photocathodes

We successfully operated a cascaded GEM-GPM having a reflective CsI photocathode. Such an arrangement completely conceals the photocathode from avalanche-generated photons and allows for reaching gains exceeding 10^6 with excellent time resolution for single electrons (~ 1 ns in pure CF_4). Using reflective photocathodes evaporated on the top face of GEM1 has the advantage of higher QE values compared to semi-transparent ones. They are also easier to produce and, in the case of CsI, are also more stable when exposed to ambient air.

We demonstrated that full single-photoelectron detection efficiency can be reached with GEM-GPMs employing reflective photocathodes, provided adequate operation parameters are chosen. In a cascade, the field E_{drift} above the first GEM coated with the photocathode, should be very small, approaching zero, to allow a good focusing of the photoelectrons into the GEM holes by the GEM electric field. The transfer field, E_{trans} below the first GEM, should be chosen as high as possible, to guarantee a high electron extraction from the GEM holes, but without suppressing the electron focusing into the subsequent multiplication

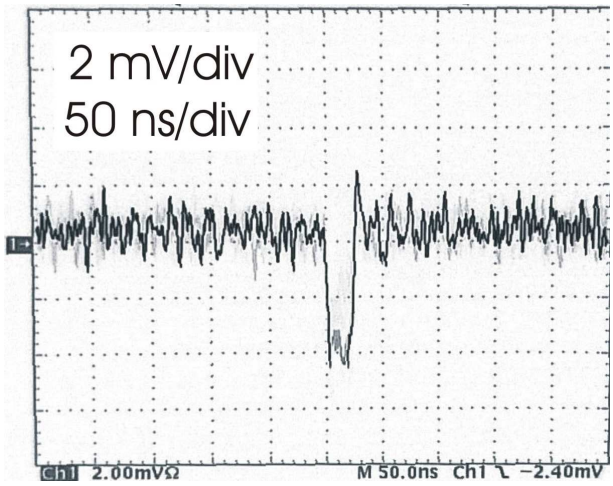

Fig. 4.27: Current signal recorded on the anode of the 4-GEM detector shown in Fig. 4.26, with a fast amplifier; ΔV_{GEM}=520 V on each GEM, in atmospheric Ar/CH_4 (20:80).

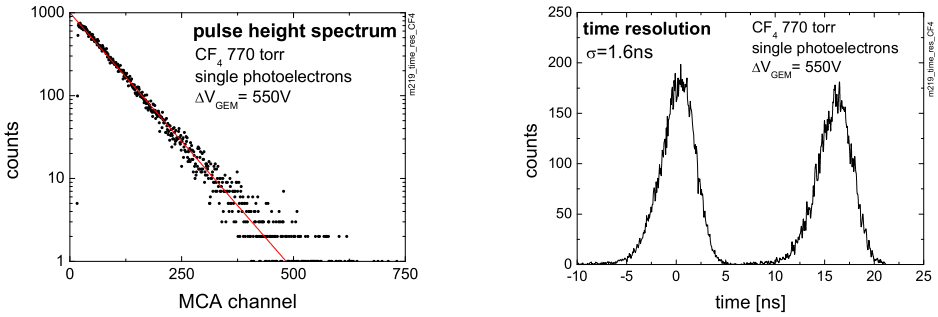

a) b)

Fig. 4.28: a) Pulse height spectrum for single photoelectron events and b) the corresponding time resolution $\sigma = 1.6$ ns at a gain of $2 \cdot 10^6$ in 770 torr of pure CF_4.

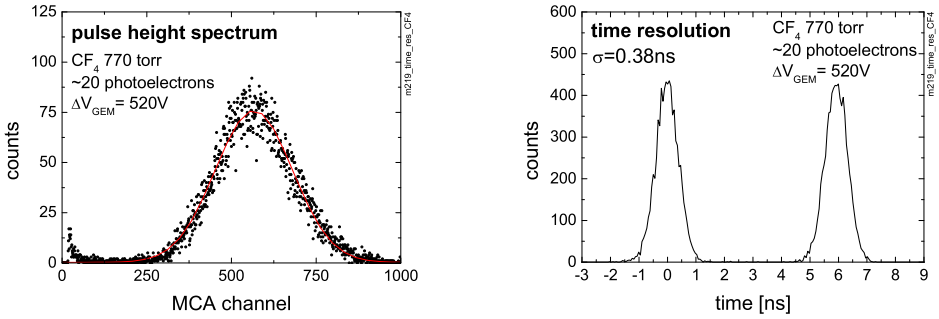

a) b)

Fig. 4.29: a) Pulse height spectrum for events with $\sim$20 photoelectrons and b) the corresponding time resolution σ=0.38 ns at a gain of $2 \cdot 10^5$ in 770 torr of pure CF_4.[6]

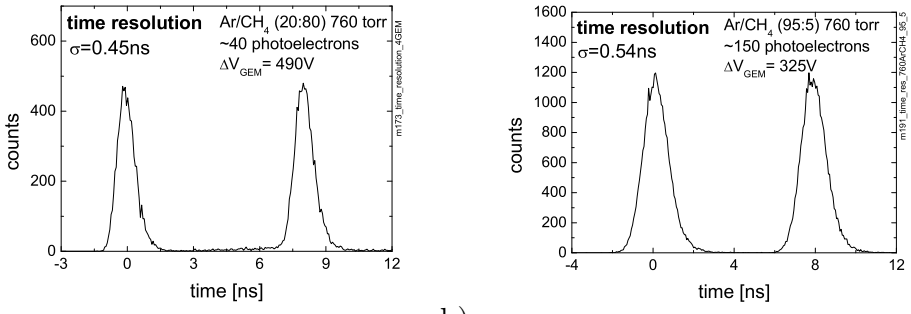

a) b)

Fig. 4.30: A time resolution of a) $\sigma = 0.45$ ns for $\sim$ 40 photoelectron events was measured at a gain of $2 \cdot 10^5$ in Ar/CH_4 (20:80) and b) of $\sigma = 0.54$ ns for 150 photoelectron events and at a gain of $6 \cdot 10^5$ in Ar/CH_4 (95:5).

element. The GEM potential, ΔV_{GEM}, is crucial, as it sets the electric field that extracts the photoelectrons from the photocathode surface and guides them into the GEM holes. Furthermore, the amplification in the first GEM is important for minimizing event losses due to electron losses to the bottom-GEM electrode at the hole exit; therefore operating

with high values of ΔV_{GEM}, particularly the first GEM is advisable.

Different GEM geometries were tested, demonstrating the advantage of GEMs having single-conical hole shapes. Operated with the wide opening facing the subsequent multiplier stage, higher charge extraction and higher transfer efficiencies are achieved compared to a double-conical hole configuration. They allow for full single-photoelectron detection at relatively low GEM gains. Nevertheless full single-photoelectron detection was also demonstrated with GEMs having double-conical hole shapes in CF_4, albeit at higher gains.

In all gases investigated, full single-photoelectron detection efficiency was achieved. Gases with low electron backscattering require lower fields at the photocathode surface for efficient operation and therefore can be operated at lower ΔV_{GEM} values.

Multi-GEM GPMs with reflective photocathodes are ideally suited for photon detection in environments with a high background of ionizing radiation. When operated with a small negative drift field and high ΔV_{GEM}, the loss in photoelectron collection efficiency, ϵ_{coll} is negligible and the detector has a largely reduced sensitivity to ionizing radiation, as only electrons created very close to the photocathode surface are transferred into the GEM holes. This unique property ensures that the majority of the particle-induced ionization electrons in the drift gap are collected on the cathode mesh (see Fig. 4.1) instead of reaching the multiplying stages of the detector, resulting in a considerably reduced background rate. Relativistic-particle rejection factors > 100 were recently demonstrated [132]. A triple-GEM detector with a reflective CsI photocathode operated with a small negative drift field is currently under study for a hadron-blind Cherenkov detector of the PHENICS experiment at RHIC (BNL) [97, 132].

The time resolution values obtained in a 4-GEM GPM with reflective photocathode are still considerably larger than those of vacuum photomultipliers, reaching values below 1 ns for single photoelectrons [133] for small area coverage PMTs. Reducing the electron diffusion by reducing the drift length and working with higher electric fields can be expected to further improve the time resolution GEM-GPMs, approaching values close to vacuum PMTs [74].

[6] A different MCA scale was used than in Fig. 4.28.

5. ION FEEDBACK IN GPMS

5.1 Introduction

As was discussed already in Sec. 2.6.3 feedback effects are of high concern in GPMs, because of the abundance of avalanche-generated photons and ions and the low electron emission threshold of the photocathode. They limit not only the maximum gain but also degrade the detector's position and time resolution and may result in an accelerated photocathode aging. Photon-induced secondary electron emission is practically eliminated in GEM GPMs with reflective photocathodes due to the optical opacity of the GEM elements as was discussed in and Sec. 4. Unfortunately, not all ions are stopped and neutralized on the GEM electrodes. A fraction of the ions follow the electric field lines through the GEM holes to the photocathode, where they may release secondary electrons and cause ion feedback.

Ion feedback has not been reported in GPMs with CsI photocathodes at atmospheric pressure operation, even at very high gains. Ion induced aging of CsI photocathodes has been investigated in depth [17, 66]. With photocathodes sensitive to longer wavelengths, i.e. with lower electron emission threshold E_{pe}, employed in multi-GEM GPMs, ion feedback was seen to induce a rather low gain limit. As an example, Fig. 5.1 shows an anode pulse originating from a multi-photon event measured in a single GEM GPM with a semi-transparent K–Cs–Sb photocathode sealed in 680 torr argon[1]. Several generations of ion-feedback pulses appear and the gain is limited to ~ 30, as compared to about 10^3 with a CsI photocathode under similar conditions. The feedback frequency T_+ $\sim$300 μs (Fig. 5.1) corresponds to the ion drift time from the GEM holes to the photocathode (see Sec. 2.6.3) and clearly identifies the secondary pulses as ion-induced ones.

To allow for realizing high-gain visible-light sensitive GPMs, we studied in detail ion-feedback phenomena on K–Cs–Sb photocathodes and methods to reduce their impact on detector operation [134, 120]. The results of these successful attempts are described in Sec. 6 , 7 and 8. This chapter addresses the physical processes of ion feedback in GEM GPMs, extending the discussion of Sec. 2.6.3 and supporting them by measurements.

5.2 Theoretical considerations

For an adequate description of ion feedback processes in multi-GEM GPMs Eq. 2.6 for the ion feedback strength μ has to be modified. Firstly, a fraction of the avalanche generated ions is neutralized on various detector electrodes and does not reach the photocathode. The *ion back-flow efficiency*, ϵ_{bf}, designates the probability that an ion originating from the avalanche process arrives at the photocathode. Furthermore, the number of secondary

[1] The fabrication of sealed detectors is discussed in App. B

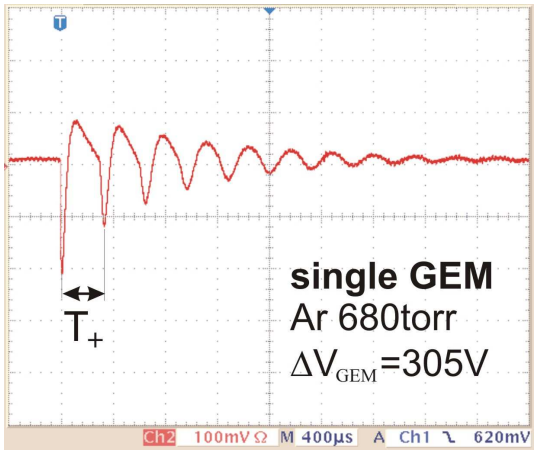

Fig. 5.1: A primary multi-photon pulse and the subsequent ion-induced secondary pulses measured in a single GEM GPM with semi-transparent K–Cs–Sb photocathode, operated in 680 torr of Ar at a gain of ∼30.

electrons generated by ion impact and initiating feedback pulses is somewhat reduced by back-scattering on gas molecules (Sec. 2.6) by a factor $\epsilon_{extr} = 1 - \epsilon_{bs}$. A modified formulation of Eq. 2.6, appropriate for the ion feedback strength μ in multi-GEM GPMs yields[2]:

$$\mu = \gamma_+ \cdot G \cdot \epsilon_{bf} \cdot \epsilon_{extr} \ . \tag{5.1}$$

The maximum attainable gain in such a system induced by ion feedback ($\mu = 1$) is therefore given by:

$$G_{max} = \frac{1}{\gamma_+ \cdot \epsilon_{bf} \cdot \epsilon_{extr}} \ . \tag{5.2}$$

From this relation, three approaches for increasing the maximal detector gain can be deduced:

1. Decreasing ϵ_{extr} by working in conditions with high electron backscattering (see Sec. 2.6). Unfortunately this option is ruled out for practical purposes, as also primary photoelectrons will suffer from the increased backscattering, decreasing the single photoelectron detection efficiency of the detector.

2. By collecting and neutralizing avalanche-generated ions on various detector electrodes and preventing them from reaching the photocathode, ϵ_{bf} is decreased and higher gains can be reached. This can be achieved by properly adjusting the electric fields inside the detector (Sec. 6) or by modifying the detector geometry and mode of operation (Sec. 7).

3. Reducing γ_+, the probability that an ion impinging on the photocathode releases a secondary electron on the photocathode (subsequently called the *ion feedback probability*). Factors influencing the value of γ_+ and its significance, as well as possible approaches to lower its value are discussed below.

[2] The additional "-1" term appearing in Eq. 2.6 is neglected here as typically $G \gg 1$.

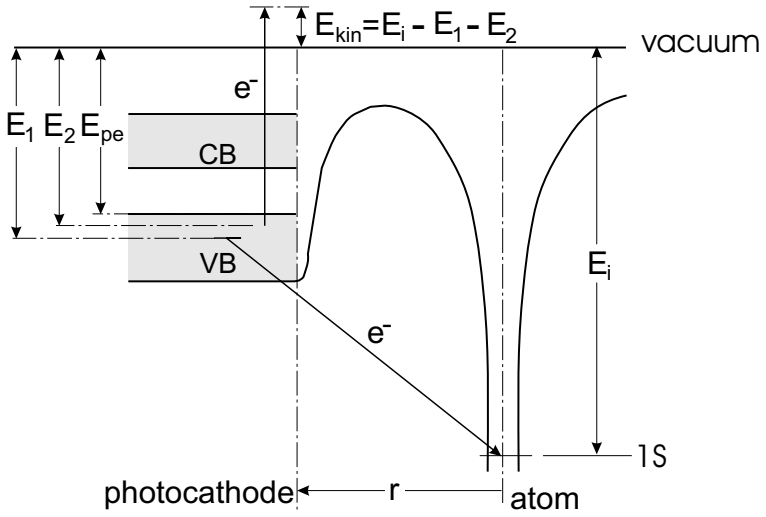

Fig. 5.2: Auger neutralization of an ion arriving at the photocathode results in the emission of a secondary electron. E_i is the potential energy of the ion, E_{pe} the photoemission threshold, E_1 and E_2 are the potential energy of the photocathode electrons that participate in the process, and E_{kin} the kinetic energy of the emitted secondary electron. CB and VB denote the conduction and valence band of the photocathode respectively.

5.3 The role of γ_+

In the context of Eq. 5.1, γ_+ designates the probability that a material releases a free electron under impact of a single ion. It does not depend on the specific detector geometry or electric field conditions but contains only the information on the physical processes taking place at the vicinity of the photocathode. The kinetic energy of ions in atmospheric pressure gases is considerably lower than 1 eV and has no influence on the secondary electron emission process [68, 135]. It is rather governed by the ions' potential energy of excitation and the properties of the emitting surface. The relevant process of *Auger-neutralization* [135] is diagramed in Fig. 5.2: A positive ion arrives at the photocathode surface and recombines with an electron from the photocathode. The remaining energy of the ion, $E_i - E_1$, is carried away by a virtual photon, exciting a secondary electron in the photocathode. This secondary electron can be emitted from the photocathode into gas with a maximum kinetic energy $E_{kin} = E_i - E_1 - E_2$.

The ions' minimal potential energy at which Auger-neutralization can occur is given by:

$$E_i \geq 2 \cdot E_{pe} \,, \tag{5.3}$$

namely when the potential energy (or ionization energy) E_i of the ions is at least two times the photoemission threshold E_{pe}. Consequently when ions with high ionization energy impinge on a photocathode with low photoemission threshold, a pronounced ion feedback can be expected. This is the reason why ion feedback is not observed in GPMs with CsI photocathodes ($E_{pe} \approx 6$ eV), while it severely constrains the operation of GPMs with K–Cs–Sb photocathodes ($E_{pe} \approx 2.1$ eV).

In ionized gas mixtures, a very efficient process of charge exchange between ions and gas

gas	E_i [eV]	gas	E_i [eV]
He	24.48	CH_4	12.6
Ne	21.56	Xe	12.12
Ar	15.75	C_2H_6	11.5
N_2	15.5	C_2H_2	11.4
H_2	15.42	C_3H_8	11.1
Kr	13.99	iso-C_4H_{10}	10.57
CO_2	13.7	C_2H_4	10.5

Tab. 5.1: Ionization potentials E_i of some gases commonly used in gaseous multipliers [137].

molecules with lower ionization potential occurs [59], similar to the process occurring in Penning gas mixtures [136]. Depending on the ion species involved, the charge exchange occurs typically after a few hundred collisions; under normal conditions (mean free path $\sim 10^{-5}$ cm), one can assume that a drift length between 10^{-3}–$10^{-2}p^{-1}$ cm (p is the fraction of the lowest ionization potential molecule in the gas mixture) is sufficient to have left migrating only one kind of ion species. Small differences in the ionization potentials result in shorter exchange lengths [59]. For typical gas mixtures at atmospheric pressure, the exchange length is a few millimeters at most; consequently, only the species with the lowest ionization potential can be expected to participate in the Auger-neutralization process. Tab. 5.1 lists the ionization potentials of some gases commonly used in mixtures for electron multipliers.

5.4 Quantitative evaluation of the ion feedback

The quantitative evaluation of ion feedback processes on K–Cs–Sb photocathodes is rather complex. Variations in the photocathode production process, and therefore its stoichiometry [138] makes the comparison of results obtained with different photocathodes questionable. Therefore, the measurement results provided below were obtained with a single K–Cs–Sb photocathode whose QE was monitored before and after the measurements. This approach required an unsealed operation of the GPM *inside* the gas filled vacuum chamber.

5.4.1 Setup and Methodology

The procedure of photocathode fabrication and characterization is provided in Sec. 3.2; the assembly of an electron multiplier inside a sealing package and its installation in the sealing chamber of the bi-alkali system is described in detail in App. A. The electron multiplier employed in this measurements consisted of a double GEM. Each of the detector's electrodes was connected to a power supply (Fig. 5.3); the package body was grounded, and the photocathode, placed on top of the package, electrostatically connected to it. The detector could be operated either in single- or double-GEM mode. The bottom side of GEM2 was used as the readout anode in double GEM operation. This is a valid approach, considering that the grounded package body generates a weak reverse field below GEM2 and ensures the collection of all electrons on the bottom GEM2 face. In single-GEM operation the interconnected faces of GEM2 served as an anode.

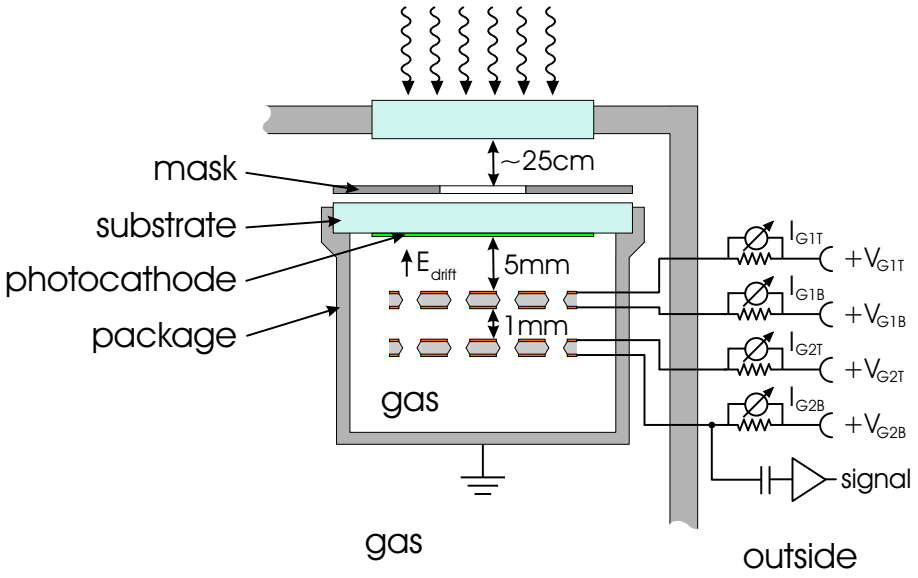

Fig. 5.3: Setup for ion feedback measurements inside the sealing chamber of the bi-alkali system.

The potentials of the detector electrodes were supplied by individual power supplies via 10 MΩ resistors. By recording the voltage drop on these resistors the respective currents due to avalanche charge collection were determined with reasonable accuracy ($\sim \pm 5\%$). In a pulse-mode operation, the charge signal was recorded from the respective anode via a decoupling capacitor. Fig. 5.3 shows the schematic detector layout within the sealing chamber.

The photocathode was illuminated through a stainless steel mask placed on top of the glass substrate, reducing the active diameter of the photocathode to ∅ 15 mm. This is to ensure that we measure in a region of homogeneous drift field over the active photocathode area, with no position-dependent photoelectron backscattering and electron collection.

According to the procedures described in App. B, the vacuum system was baked for two days after placing the electron multiplier inside the sealing chamber. At room temperature, the gas mixture was introduced to the sealing and activation chambers until a pressure of 700 torr was reached. Subsequently the photocathode was transferred from the activation chamber to the sealing chamber and placed on top of the electron multiplier, forming a visible-light sensitive GPM. Before operating the detector in gas avalanche mode, the photocathode stability was verified by measuring the photocurrent on the interconnected GEM1 faces with a constant drift field of 500 V/cm and under constant illumination for at least 15 minutes.

For the first measurements, pure argon was introduced at a pressure of 700 torr. After concluding the measurements in argon, the photocathode was retracted to the activation chamber for protection and the gas pressure was reduced to 686 torr by pumping through the filter of the gas system with a dry scroll pump. Subsequently, pure CH_4 was introduced, raising the pressure back to 700 torr, yielding a gas mixture of Ar/CH_4 (98:2). The photocathode was returned to the detector package and measurements in the new gas mixture were performed. Accordingly, the procedure was repeated several time, realizing mixtures of Ar/CH_4 (95:5), (90:10) and (80:20). These gas mixtures were of particular interest, as a dependence of the ion feedback probability on the ratio of Ar and CH_4 was reported elsewhere

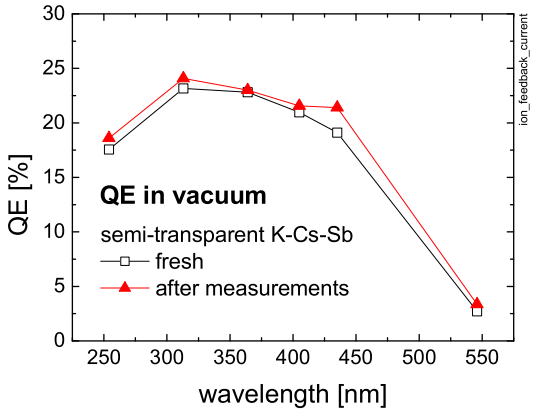

Fig. 5.4: The absolute QE of the semi-transparent K–Cs–Sb photocathode measured in vacuum immediately after fabrication and after the series of measurements in various gas mixtures.

[122]. Following the operation in Ar/CH_4 (80:20) the chamber was evacuated to 10^{-8} torr; pure CH_4 was introduced and measurements in this gas were performed.

After all measurements were completed (lasting approximately 14 hours), the chamber was evacuated for a concluding photocathode QE measurement inside the activation chamber. Fig. 5.4 demonstrates that the QE of the K–Cs–Sb photocathode was practically not affected during the measurements; the small increase in QE observed is within the measurement accuracy, taking into account that the stainless steel mask on top of the photocathode substrate may have shifted slightly during the photocathode transfer.

5.4.2 Pulse-mode measurements

The capacitively decoupled signal was processed by a charge sensitive pre-amplifier[3] followed by a linear amplifier and a digital oscilloscope[4]. Bunches of up to ~ 1000 photoelectrons were generated on the K–Cs–Sb photocathode by illuminating it with a H_2 flash lamp through the sapphire window on top of the sealing chamber. Single-GEM operation in 700 torr of argon is limited by ion feedback to a rather low maximum gain $G_{max} \sim 30$. The operation at such low gains and the electronic noise permitted pulse recording only by averaging a few hundred pulses on the digital oscilloscope.

Anode pulses obtained for drift fields of 0.2 and 0.6 kV/cm are shown in Fig. 5.5. In both cases secondary pulses with a generation time of several hundred microseconds are observed, indicative of ion feedback. The dependence of the generation time on the drift field E_{drift} is shown in Fig. 5.6. The drift-time of argon ions with mobility $\upsilon(Ar^+)$ over the 5 mm distance from the GEM holes to the photocathode

$$T_+ = \frac{5\ mm}{\upsilon(Ar^+) \cdot E_{drift}} \quad , \tag{5.4}$$

[3] 109A, ORTEC
[4] TDS 3052, Tektronix

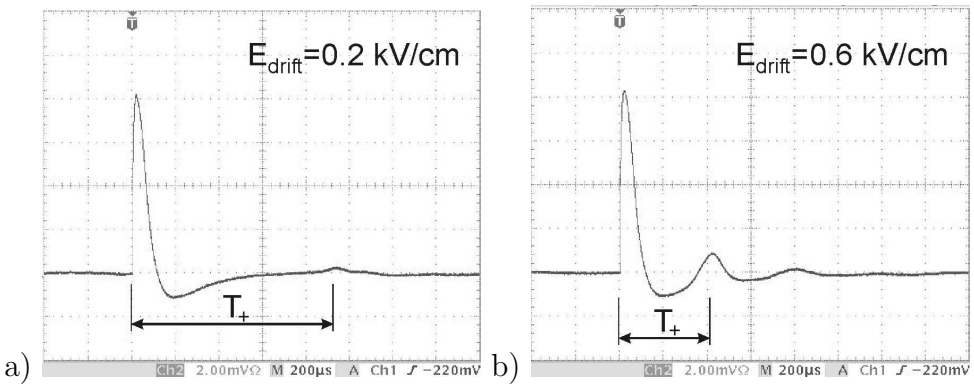

a) b)

Fig. 5.5: Anode pulses obtained from a single-GEM GPM with a K–Cs–Sb photocathode, illuminated with short light flashes. It was operated with a drift field a) E_{drift}= 0.2 kV/cm and b) E_{drift}= 0.6 kV/cm under a gain of ∼30 in 700 torr of Ar.

is equal to the generation time T_+, as expected. This is proved by fitting the data points according to Eq. 5.4; the dashed line in Fig. 5.6 yields a mobility for argon ions of

$$\upsilon(Ar^+) = 1.75 \pm 0.2 \, \frac{cm^2}{V \cdot s} \tag{5.5}$$

which is in good agreement with the literature value of 1.7 $\frac{cm^2}{V \cdot s}$ [59].

Unfortunately it is not possible to extract quantitative information on the feedback strength μ or on the feedback probability γ_+ from pulse measurements. The arrival times of the electrons contributing to the secondary pulse is considerably more spread in time compared to the primary pulse. This is due to the additional drift and diffusion of the avalanche ions and the secondary electrons and therefore dependent on the choice of E_{drift}. As a result the height of the ion feedback pulse compared to the primary pulse is strongly influenced by the bandwidth of the capacitor–preamplifier system connected to the anode and by the choice of E_{drift}. This is obvious from examining the two pictures of Fig. 5.5. Firstly, the secondary pulses have considerably longer rise time than the primary one. Secondly, the secondary

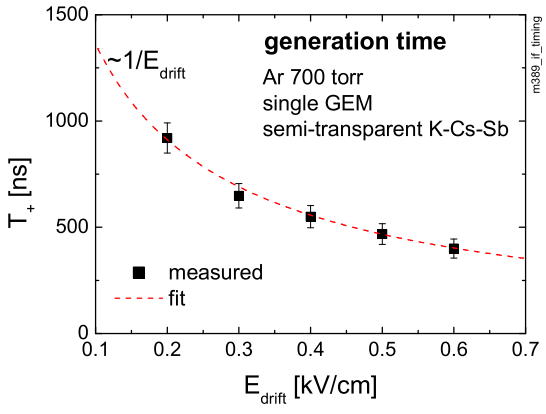

Fig. 5.6: The dependence of the ion feedback generation time T_+ on the drift field E_{drift}.

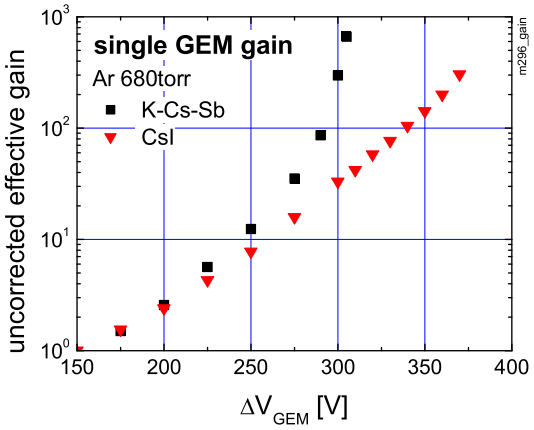

Fig. 5.7: Gain-voltage characteristics measured in current-mode in a single-GEM detector operated in pure argon at 680 torr. The ion feedback leads to a diverging behaviour with a K–Cs–Sb photocathode, while for a CsI photocathode the standard exponential behaviour is observed. The detector was operated with E_{drift}=500 V/cm.

pulse is attenuated by a factor ∼10 when working with 0.2 kV/cm instead of 0.6 kV/cm, while the ion back-flow and therefore the ion feedback is expected to change only by a factor ∼0.6/0.2 = 3 (see below).

5.4.3 Current-mode measurements

Measuring the currents on all detector elements allows for a quantitative analysis of the ion feedback strength. Recording the gain in current mode as a function of ΔV_{GEM}, described in Sec. 3.7, yields the expected exponential dependence up to a point where the secondary electrons contribute significantly to the current. As an example, Fig. 5.7 shows the gain curve obtained with a single-GEM-GPM sealed to a semi-transparent K–Cs–Sb photocathode in 690 torr of argon. Above ΔV_{GEM}=200 V the gain curve increases much faster than exponentially and diverges at about 310 V. At this point the ion feedback strength μ approaches unity and detector break-down is inevitable. For comparison, a second gain curve is plotted in Fig. 5.7, obtained with the same detector but coupled to a semi-transparent CsI photocathode and operated in the same conditions during detector testing. As ion feedback on CsI photocathodes has only a minor effect at atmospheric pressures, the gain curve has a typical exponential behaviour.

From analysis of the gain curve, measured with the K–Cs–Sb photocathode, and its deviation from the exponential increase, the strength of the ion feedback and the respective value of γ_+ can be deduced. The measured gain G_{meas} obtained from the anode current for a given value of ΔV_{GEM} contains contributions from the ion feedback according to:

$$\begin{aligned} G_{meas} &= G + \mu \cdot G + \mu^2 \cdot G + \ldots \\ &= G \sum_{n=0}^{\infty} \mu^n \\ &= \frac{G}{(1-\mu)} \ . \end{aligned} \tag{5.6}$$

G is the effective gain of the multiplier *without* ion feedback and μ the ion feedback strength at a given value of ΔV_{GEM}. Insertion of Eq. 5.1 into Eq. 5.6 yields an expression for G_{meas}:

$$G_{meas} = \frac{G}{1 - \gamma_+ \cdot \epsilon_{bf} \cdot \epsilon_{extr} \cdot G} \ . \tag{5.7}$$

Under constant illumination of the photocathode with a UV-LED[5], the current on all GEM electrodes was determined as a function of ΔV_{GEM}. These values were corrected for dark- and leakage-currents for each value of ΔV_{GEM} by blocking the light from the lamp. The currents on the electrodes were limited to $\sim$10 nA by employing optical absorbers in the light path and correcting the measured currents accordingly. From the current measurements, the parameters G_{meas}, G, ϵ_{bf} and ϵ_{extr} were obtained, allowing to determine the value of γ_+ according to Eq. 5.7.

Determination of ϵ_{extr}

Prior to the operation in avalanche mode, the detector was operated in photodiode-mode by applying a positive potential on the interconnected GEM1 electrodes and measuring the corresponding current as a function of E_{drift}. By normalizing this current to the vacuum photocurrent, obtained at the beginning and at the end of the measurement series, the photoelectron extraction efficiency ϵ_{extr} was obtained. The dependence of ϵ_{extr} on the drift field E_{drift} for the Ar/CH_4 mixtures investigated is given in Fig. 5.8. As expected, with increasing concentration of CH_4 the backscattering probability is reduced and ϵ_{extr} increased. Above a value of E_{drift}= 400 V/cm the extraction efficiency ϵ_{extr} changes only moderately, and therefore this value of E_{drift} was chosen in all gases for subsequent measurements and the corresponding ϵ_{extr} could therefore be assumed constant throughout the measurements.

Determination of ϵ_{bf}

For a given GEM voltage ΔV_{GEM}, the ion back-flow is usually defined by the ratio of currents measured on the anode (due to electrons) and on the photocathode (due to back-flowing avalanche ions). Unfortunately, the photocathode was grounded inside the vacuum chamber (via the package body), preventing the direct measurement of its current. Instead, as the sum of the currents on all detector electrodes must be zero, the photocathode current can be determined indirectly. Of course, this method suffers from relatively large errors, especially

[5] NSHU590A, Nishia

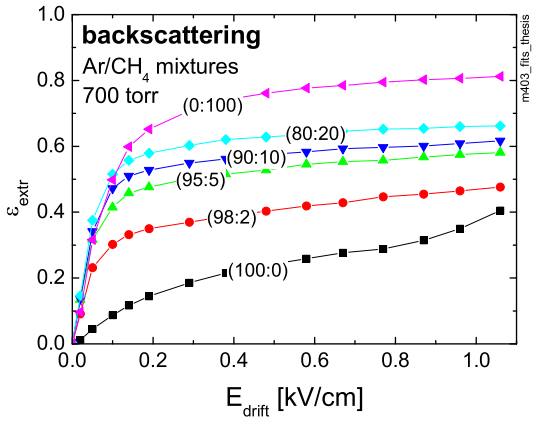

Fig. 5.8: The extraction efficiency ϵ_{extr} as a function of E_{drift} for the Ar/CH_4 mixtures investigated. The pressure in all cases was 700 torr.

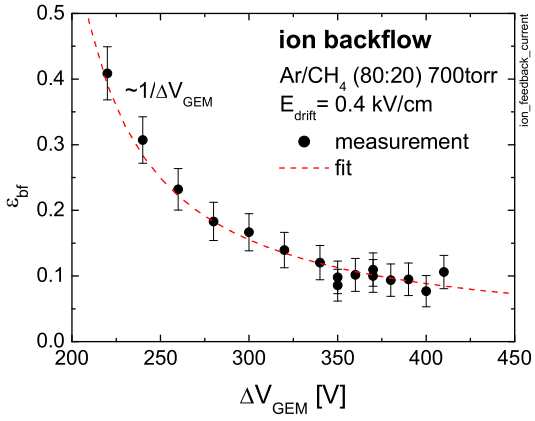

Fig. 5.9: The ion back-flow ϵ_{bf} as a function of ΔV_{GEM} measured in 700 torr of Ar/CH_4 (80:20) by current recording on all electrodes. The dashed line is a fit to the data points.

for small values of the ion back-flow ϵ_{bf}, but it was nevertheless sufficient here. Fig. 5.9 shows the ion back-flow ϵ_{bf} as a function of ΔV_{GEM} in a single GEM operated in 700 torr of Ar/CH_4 (80:20) with a drift field E_{drift}=400 V/cm. The dashed line indicates a fit to the data points, assuming a linear dependence of the ion back-flow on the ratio $E_{drift}/\Delta V_{GEM}$ (see discussion in Sec. 2.7.3 and Sec. 6). The value of ϵ_{extr} as a function of ΔV_{GEM} required in Eq. 5.7 was determined from the fit of the ion back-flow for the respective gas composition.

Determination of G_{meas}

The measured gain, G_{meas}, is determined in the usual way (see Sec. 3.7), by measuring the current on the anode and normalizing it to the photocurrent. As described above, the photocurrent was obtained from the photodiode-mode measurement at a drift field E_{drift}=400 V/cm. The data points of the G_{meas} values as a function of ΔV_{GEM} are shown

in Fig. 5.10 for different Ar/CH_4 mixtures.

Determination of G

In all gas mixtures investigated, with a K–Cs–Sb photocathode the ion feedback-induced deviation of G_{meas} from the exponential is evident (Fig. 5.10). However for low values of ΔV_{GEM}, ion feedback effects do not significantly contribute to the anode current and G_{meas} can be fitted with an exponential function in this range. These fits are displayed as dashed lines in the plots of Fig. 5.10, extrapolated to high values of ΔV_{GEM}, where G_{meas} does no longer represent the effective gain of the detector. The values of G as a function of ΔV_{GEM}, required in Eq. 5.7, were obtained from these fits.

Determination of γ_+

With the above parameters determined, the value of γ_+ can be extracted from fitting the values of G_{meas} according to Eq. 5.7, provided a significant deviation from the exponential gain-voltage characteristic is observed. For most gas mixtures, single-GEM operation was sufficient to induce the required gain deviations, except for Ar/CH_4 (98:2) and (95:5) mixtures. In double-GEM mode, the higher ion back-flow achieved when working with lower values of ΔV_{GEM} on each GEM, compensated for the lower electron extraction efficiency in these gases.

The solid line in the graphs of Fig. 5.10 displays the fits to the G_{meas} values. It describes very well G_{meas} over the whole range of GEM voltages, including the divergence close to the breakdown point, corroborating the above assumptions on the ion feedback and the deduction of γ_+. The γ_+ values obtained from these fits are summarized in Fig. 5.11 as a function of the gas mixture. Both, single- and double-GEM mode measurements were performed in Ar/CH_4 (80:20) and yielded comparable γ_+ values, confirming the validity of comparing results obtained from these two modes of operation.

As expected, the feedback probability is the highest in pure Ar, due to its high ionization potential E_i=15.75 eV; practically every second argon ion impinging on the photocathode induces a secondary electron. Pure methane on the other hand yields a factor ~ 10 lower feedback probability due to its lower ionization potential of 12.6 eV. The mixtures display γ_+ values similar to pure methane, confirming the charge exchange model of argon to methane ions. The previously anticipated improved operation of GEM-GPMs in Ar/CH_4 mixtures with minimal CH_4 content [122] are rebutted by this measurements. The higher gains G_{max} reported in these gases can be explained by a higher backscattering and lower ion back-flow.

5.5 Discussion and outlook

For reaching gains of $\sim 10^6$ with typical values of ϵ_{extr} and ϵ_{bf} of ~ 0.7 and ~ 0.1 respectively, the feedback probability γ_+ has to be as low as 10^{-5} according to Eq. 5.2. The measured values of γ_+ in Ar/CH_4 mixtures of $\sim 10^{-2}$ allows an operation at a gain of a few hundred at most. Similar observations of ion induced gain limitations in GPMs are reported by the

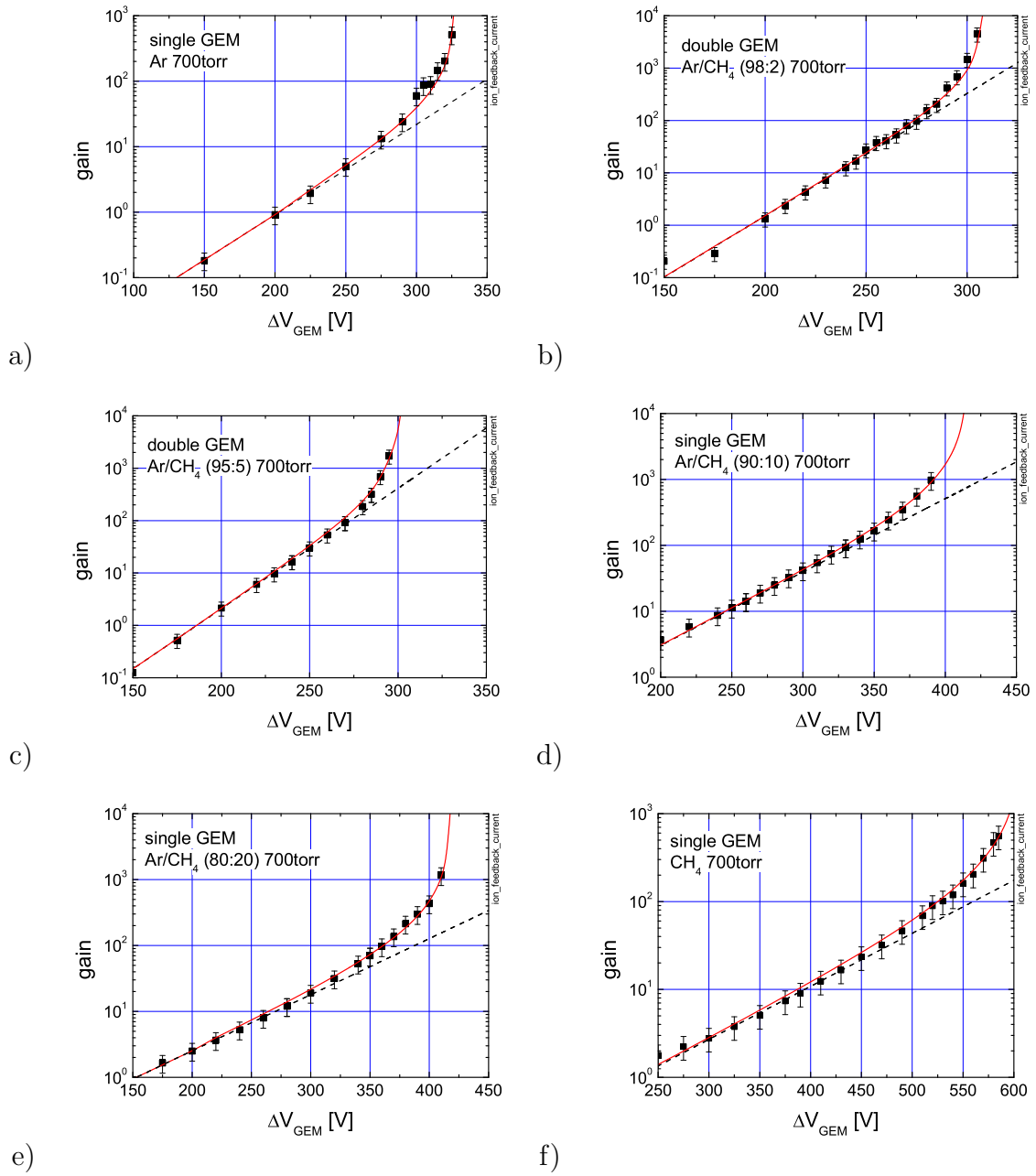

Fig. 5.10: Gain versus ΔV_{GEM} measured in a) pure Ar, b) Ar/CH_4 (92:2) c) (95:5), d) (90:10), e) (80:20) and f) pure CH_4.

authors of [139]. The authors of [28] measured a feedback probability $\gamma_+ = 3.4 \cdot 10^{-2}$ on a Cs_3Sb photocathode sealed in 20 torr of pure methane to a parallel plate electron multiplier. These values are very close to the results of this work with K–Cs–Sb photocathodes; As the photoemission threshold of Cs_3Sb photocathodes of E_{pe} =2.0 eV is very close to the one of K–Cs–Sb photocathodes (E_{pe} =2.1 eV), the Auger neutralization model predicts similar ion feedback probabilities for both cases, as is indeed the case.

No gases with ionization potential below the critical value for ion feedback on K–Cs–Sb photocathodes $E_i \leq 2 \cdot E_{pe} \approx 4.2$ eV can be devised. Nevertheless, using gas mixtures

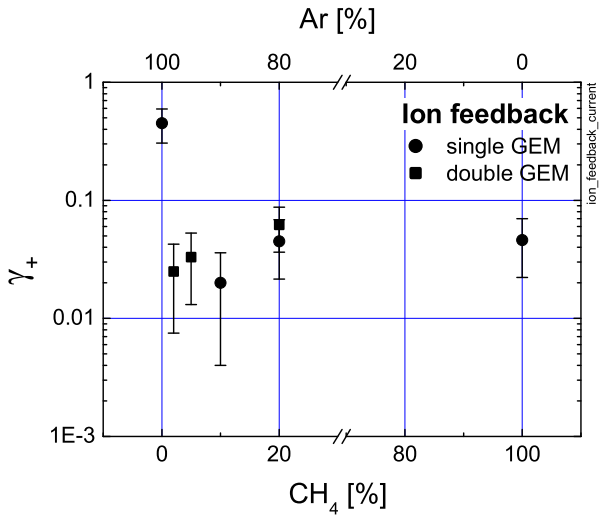

Fig. 5.11: The ion feedback probability γ_+ obtained from the fitted data for the different Ar/CH_4 mixtures at 700 torr.

with components having ionization potentials lower than CH_4 can be expected to reduce the feedback probability and increase the maximum gain of GPMs. From the gases listed in Tab. 5.1, these are long-chain hydrocarbons, e.g. iso-butane. On the other hand, ions of such gases have a high probability for dissociation, creating free radicals; they are known to induce aging in gas avalanche detectors. Photocathode may suffer from enhanced chemical aging when operated in such an environment. Nevertheless this approach is worthy of further investigation.

Another option to prevent ion feedback might be surface-coating of the K–Cs–Sb photocathodes with higher band-gap materials (e.g. CsI), similar to the approach proposed for protecting them from gas impurities [25]. Indeed in this work [25], a gas gain of 10^4 was reached in atmospheric methane in a parallel plate gas amplification mode with a K–Cs–Sb photocathode coated with 300 Å of CsBr. Though in this configuration all avalanche ions hit the photocathode, the authors did not observe any ion feedback. A feedback probability of $\gamma_+ \leq 10^{-4}$ can therefore be inferred, albeit at the cost of a considerable loss in QE by a factor $\sim$7–10 for the 300 Å coating film. Since the thickness of 300 Å was chosen to provide sufficient protection from oxygen, it may not be the optimal for providing protection form Auger ion neutralization. Therefore, it remains to be investigated if thinner coating films, yielding higher residual QE values, will show a similar effect on γ_+. In photocathodes with a spectral sensitivity further extended to the red, e.g. NEA photocathodes, ion feedback effects are expected to be even more severe.

Reduction of ion feedback effects can also be obtained by reducing the avalanche ion backflow to the photocathode, discussed in the following sections.

6. ION BACK-FLOW REDUCTION IN GEM-GPMS

6.1 Introduction

In GPMs, the large amount of avalanche generated ions back-flowing from the amplification stages to the photocathode of the detector may cause ion feedback effects, i.e. secondary electron emission; these limit the detector gain and affect its operation and response (see discussion of Sec. 5). Furthermore, accumulated ion impact on the photocathode is known to damage the photocathode surface and deteriorate its QE [67]. Avalanche-ion back-flow and its neutralization is a known important general problem in gaseous detectors. It is particularly important in large-volume Time Projection Chambers (TPCs) [140]; at high particle fluxes, avalanche generated ions drifting backwards from the multiplying elements into the sensitive volume, cause considerable electric field distortions and seriously degrade the detector's position resolution. GEM amplification stages for TPCs [107, 108] are currently being considered in an attempt to minimize the amount of back-flowing ions into the drift region.

Multi-GEM detectors have a considerably reduced ion back-flow compared to parallel-plate and wire-based multipliers. A fraction of the avalanche ions, of which the majority is generated at the last multiplication stage, is neutralized on the successive detector electrodes [84]. A further reduction of the ion back-flow would considerably improve the operation characteristics of GEM-based GPMs and TPCs. Our study on the ion transport in multi-GEM detectors, directed towards the reduction of the ion back-flow, is presented below. The results were published in [134].

6.2 Theoretical considerations

One has to distinguish *ion feedback*, which is the common terminology for ion-induced secondary effects (e.g. ion-induced electron emission from surfaces) from *ion back-flow*, which quantifies the fraction of avalanche-generated ions that leaves the amplification stages of the detector and is collected on the photocathode. In the case of GPMs, most of the back-flowing ions are collected on the photocathode, where they may initiate secondary electron emission resulting *ion feedback*; in TPCs, they constitute a slowly drifting space charge, causing electric field distortions, deteriorating the detector's resolution. The common definition of ion back-flow, denoted as ϵ_{bf}, is the flux of ions collected on a cathode, divided by the flux of electrons collected on the anode. This *practical* definition is easily accessible by measuring the relevant DC currents in a detector under constant irradiation or in the case of GPMs, constant illumination of the photocathode. In GPMs the ratio of the ion current on the photocathode and the electron current on the readout-anode determines the back-flow ϵ_{bf}.

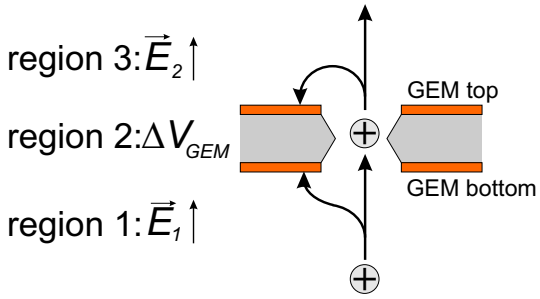

Fig. 6.1: Ion transfer through a GEM can be regarded as a two-step process: from region 1 to region 2 it is governed by the ratio $\Delta V_{GEM}/E_1$ and from region 2 to region 3 it is governed by $E_2/\Delta V_{GEM}$.

One has to be aware, that with this definition the ion back-flow is affected both by the ion and by the electron transport properties through the GEM.

Similar to the transfer of electrons and ions through a wire mesh [141, 142], charge transfer in GEM detectors depends mainly on the electric field values below, within and above the GEM electrode, as discussed for electrons in Sec. 2.7.3 and in [84]. Unlike electron transport in multi-GEM detectors, which is strongly influenced by the gas mixture and pressure, ion transport hardly depends on these factors [127, 99]; due to their higher mass, diffusion in most gases is small when compared to the relevant detector dimensions (e.g. GEM hole size and pitch). To a good approximation, ion transport is governed by the GPM geometry and the electric field conditions only. Fig. 6.1 illustrates the possible drift paths of ions in the vicinity of a GEM electrode. The ions originate from the avalanche in the GEM hole or from subsequent gas multiplication stages. Additionally, the three relevant regions with electric fields E_1, E_{GEM} (represented by the GEM potential ΔV_{GEM}) and E_2 are indicated. In analogy to the reported electron transport through a GEM foil [84], the following dependence of the ion transport on the electric fields can be anticipated: the probability of ions arriving from region 1 to enter the GEM holes will increase with $\Delta V_{GEM}/E_1$. At low $\Delta V_{GEM}/E_1$ values ions will preferentially be collected on the bottom GEM electrode. Similarly, the fraction of ions leaving the GEM holes, will increase with the ratio $E_2/\Delta V_{GEM}$, drifting into the conversion region or towards a preceding GEM. For low $E_2/\Delta V_{GEM}$ values, a larger fraction of ions is neutralized on the top GEM electrode. Obviously, the terms “low” and “high” have only a relative meaning; absolute values will depend also on the GEM geometry and, to a minor extent, on the gas mixture and pressure.

Optimal working conditions for reduced ion back-flow through a single GEM element would therefore require low $\Delta V_{GEM}/E_1$ and low $E_2/\Delta V_{GEM}$ values. Unfortunately the choice of these ratios is rather restricted in multi-GEM arrangements, where e.g. E_1 above one GEM serves simultanously as field E_2 below another GEM; the value of ΔV_{GEM} is limited by the maximum gas gain. Furthermore the electric field ratios also strongly influence the electron transport and electron losses are inevitable for a non-optimal field configuration. Although electron losses can be compensated for by increasing the real gain of the detector and working with higher multiplication voltages, more avalanche ions are generated as well, thus canceling the benefit of working in such conditions.

A field that in some cases can be chosen from a wide range of values without limiting the detector performance is the drift field E_{drift}. If an operation with low drift fields is

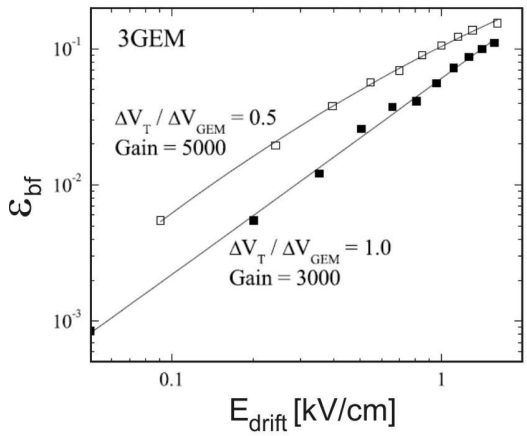

Fig. 6.2: Influence of the drift field (taken from [67]).

intended or acceptable, the ion back-flow can be considerably reduced at the last GEM stage (corresponding to an ion flow from region 2 to region 3 with a very low E_2 in Fig. 6.1). It drops almost linearly with the drift field E_{drift} as is illustrated in Fig. 6.2. The required drift field strength depends on the application; while in TPCs drift fields as low as ~ 100 V/cm are used [140], GPMs with semi-transparent photocathodes require field strengths typically exceeding 0.5 kV/cm to overcome photoelectron backscattering on gas molecules (see Sec. 2.6). The ion back-flow in these two conditions of operation differs by more than one order of magnitude.

6.3 Experimental setup and methodology

In order to make our results comprehensive and applicable for multi-GEM systems besides GPMs and to study the important case of a GEM-GPM with reflective photocathode, we chose an experimental configuration, where the ion back-flow does not depend on the drift field E_{drift}. All measurements were performed with a 4-GEM GPM having the reflective photocathode deposited on the top face of GEM1, interconnected with the cathode mesh ($E_{drift} = 0$) and keeping a constant ΔV_{GEM1}=350 V. These conditions were found to be optimal for this detector configuration in Ar/CH_4 (95:5) at atmospheric pressure (see Sec. 4 and [113]). The detector electrodes were either powered with a voltage dividing resistor network (resulting in variable transfer fields, of 2–3 kV/cm in the range of operation) or individually through 22 MΩ protective resistors. The experimental setup with the resistor network is shown schematically in Fig. 6.3.

The cathode-mesh+photocathode ion current, I_{pc}, normalized to the electron current collected on the anode, defines the ion back-flow, ϵ_{bf}, in the detector.

$$\epsilon_{bf} = \frac{I_{pc}}{I_A} \tag{6.1}$$

To minimize the influence of electron losses (to the GEM4 bottom electrode) on ϵ_{bf}, the anode mesh and GEM4 bottom electrode were interconnected. By recording the voltage drop over a 10 MΩ resistor with a floating multimeter the anode current I_A was determined indi-

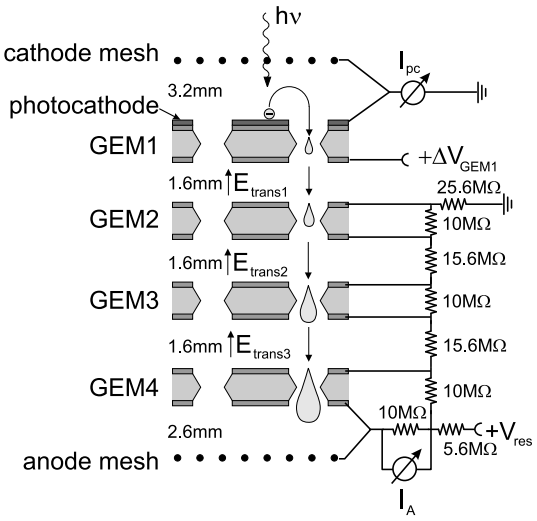

Fig. 6.3: Schematic view of the 4-GEM photodetector with reflective photocathode deposited on the top face of GEM1. Also shown is the powering scheme for ion back-flow measurements with a resistor network and constant ΔV_{GEM1}.

rectly. The considerably smaller ion current was measured directly with a pico-ampermeter connected to the photocathode substrate.

6.4 Results

6.4.1 Symmetric GEM powering

We first measured the ion back-flow in a "standard" operation mode, namely with equal ΔV_{GEM} values (with the exception of a constant ΔV_{GEM1}=350 V) and equal transfer fields. For that purpose, GEM2, GEM3 and GEM4 were powered by a resistor network (shown in Fig. 6.3); the transfer fields ($\sim$2–3 kV/cm) guaranteed a good electron transport in the detector at high gains.

In Fig. 6.4 the exponential gain increase with the voltage on the resistor network, V_{res}, is shown in addition to the corresponding ion back-flow values. The powering scheme employing a resistor network in combination with a fixed potential on GEM1 produces transfer fields which are too small for a sufficient electron transport between the GEM stages for small V_{res} values. In these conditions, ion transport is more efficient than electron transport, resulting in ion back-flow values larger than 1. With increasing V_{res} the ion back-flow drops rapidly and stabilizes at $\sim$35% for high gains.

6.4.2 Asymmetric GEM powering

In order to be more flexible in the choice of the detector potentials and the ratios between them, in all subsequent measurements the resistor network was replaced by powering each electrode through a protection resistor by an individual power supply, as already explained above.

The ion transport within the detector can be modified also by powering differently two consecutive GEMs, e.g. GEM3 and GEM4. In order to keep the overall detector gain constant, reduced potentials on one GEM were compensated for by raising the potential on the adjacent one, yielding a constant sum, i.e. for varying the potentials on GEM3 and GEM4 $\Delta V_{GEM3} + \Delta V_{GEM4}$=560 V was kept constant throughout the measurement. It should be noted that not much freedom in varying ΔV_{GEM1} exists, as its increase would lead to higher ion back-flow, while its decrease would result in the loss of primary photoelectrons (see Sec. 4.2.2). Therefore GEM1 and GEM2 were kept at constant potentials (350 V and 280 V respectively) while varying GEM3/GEM4 voltages. All transfer fields were chosen constant and equal at E_{trans}=2.5 kV/cm.

With increasing ΔV_{GEM4}, a larger fraction of ions produced in GEM4 ends on its top face. Also, as the potential across GEM3 is lowered simultaneously, the fraction of ions ending on

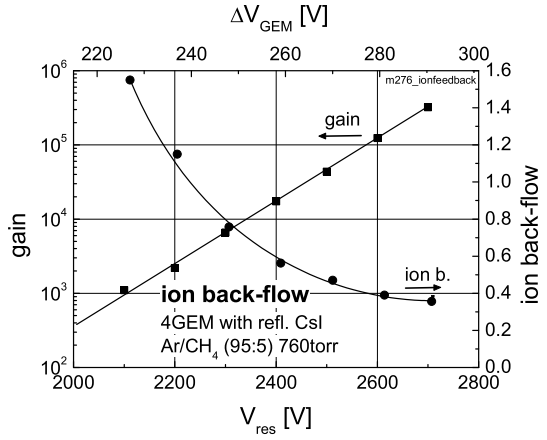

Fig. 6.4: Total gain and ion back-flow in the 4-GEM detector as function of the network voltage. The upper scale shows the corresponding voltage across the individual GEM2–GEM4 elements.

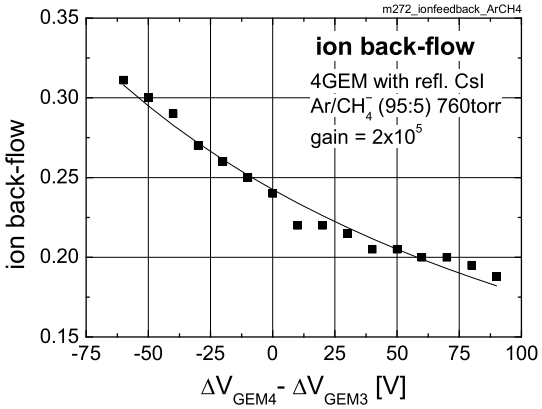

Fig. 6.5: Influence of the voltage difference between ΔV_{GEM4} and ΔV_{GEM3} on the ion back-flow.

the GEM3 bottom electrode increases. Both effects lead to a dropping ion back-flow with increasing asymmetry of the GEM powering, demonstrated in the measurement results of Fig. 6.5. Nevertheless, the improvement in ion back-flow from symmetric GEM powering (24%) to the extreme assymetric operation (18%) is not dramatic and does not justify the detector instability caused by operation GEM4 close to its breakdown limit.

6.4.3 Influence of the transfer field

Fig. 6.6 shows the influence of E_{trans3}, the transfer field between GEM3 and GEM4, on the ion back-flow and on the total gain. The other electric fields were kept constant; E_{trans1} and E_{trans2} at 2.5 kV/cm and the GEM potentials at 350 V and 280 V for GEM1 and GEMs 2,3 and 4 respectively. The gain increase with E_{trans3}, evident in Fig. 6.6, is due to an improved electron transport from GEM3 to GEM4 for $E_{trans3} < 1$ kV/cm and the extension of the electron avalanche into the transfer region for higher E_{trans} values.

At first, the ion back-flow increases with the transfer field (up to $\sim$1 kV/cm) due to a higher ion extraction from the GEM4 holes into the transfer gap above it (region 2 $\rightarrow$ region 3 in Fig. 6.1). For high E_{trans3} values the ion back-flow drops, as ions are preferentially neutralized on the GEM3 bottom electrode and do not enter GEM3 holes (region 1 $\rightarrow$ region 2 in Fig. 6.1). This behaviour is very similar to the dependence of electron transport in multi-GEM detectors on the transfer field [84].

From this result we can conclude that by choosing high values for E_{trans3}, the ion back-flow reduces from 30% in normal operation mode ($E_{trans} \sim 2kV/cm$) to $\sim$20%. Therefore, high transfer field operation in multi-GEM detectors reduces the ion back-flow to some extent.

6.4.4 Influence of the induction field

An operation with high electric fields in the induction gap (see Fig. 6.3), sufficient for parallel-plate electron multiplication is another option for reducing the ion back-flow. Unlike in the approaches discussed above, this is a non-standard mode of operation, as electron multiplication takes place not only in the GEM holes but also in the induction gap.

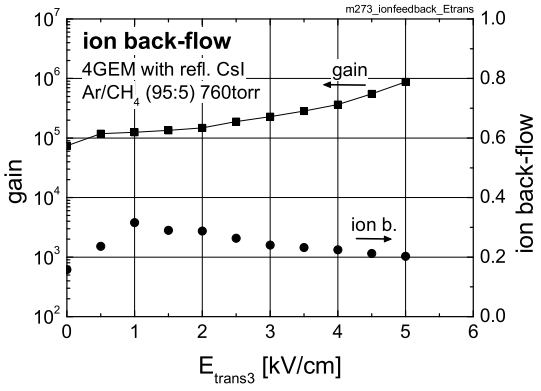

Fig. 6.6: Influence of the transfer field between GEM3 and GEM4 on the ion back-flow.

To be able to work with non-zero induction fields, the experimental setup had to be modified by disconnecting the anode mesh from the bottom GEM4 electrode and powering both individually through 22 MΩ resistors. The anode current was determined indirectly by measuring the voltage drop over the protection resistor. It is known, that for high induction field values electron losses to the bottom electrode of GEM4 are negligible [84] and hardly influence the value of ϵ_{bf}.

As the majority of ions in this mode of operation is generated in the induction gap and the high induction field E_{ind} required for multiplication induces also a low ion transmission through GEM4 (region 1 → region 2 in Fig. 6.1), such an operation has a reduced ion back-flow.

Fig. 6.7 shows the variation of the detector gain and the ion back-flow with the induction field E_{ind} for two different values of ΔV_{GEM4}. Parallel-plate amplification in atmospheric Ar/CH_4 (95:5) starts at $E_{ind} \sim 5$ kV/cm. The slight gain increase for low values of E_{ind} is due to an improved electron extraction from the GEM4 holes and due to avalanche extension out of the GEM4 holes into the induction gap.

In both cases, the ion back-flow drops with increasing E_{ind}, even before the onset of parallel-plate amplification. This is due to an improved electron extraction from GEM4 to the anode (see Sec. 6.2), when the induction field is still rather weak. For the high induction field values, a lower ion back-flow value through GEM4 is reached ($\sim 10\%$) for ΔV_{GEM4}=200 V than for ΔV_{GEM4}=300 V ($\sim 20\%$). This is a result of the higher E_{ind} values and consequently higher parallel-plate gains that could be reached for the lower ΔV_{GEM} value ($\sim 10^3$ parallel-plate gain compared to 10). The higher induction field induces lower ion transmission through GEM4 and the higher gain assures that even a larger fraction of the avalanche ions is produced in the induction gap and thus subjected to the low transmission. Unfortunately, the ion back-flow saturates at $\sim$ 10%, despite further increasing induction field and gain. It seems clear, that the avalanche in the induction gap is centered around the GEM holes. Therefore most of the ions are generated directly below the hole and, considering their low diffusion, are transferred through the GEM4 holes, explaining the observed saturation effect.

Although ion back-flow is reduced by a factor ~ 3 compared to the *standard* 4-GEM operation, this mode is more vulnerable to discharges from GEM4 to the anode, likely to damage

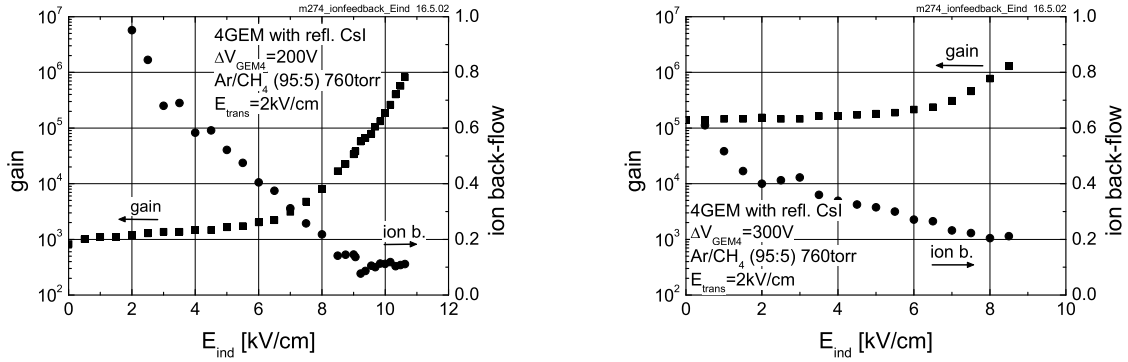

a) b)

Fig. 6.7: Influence of the induction field on the ion back-flow for a) ΔV_{GEM4}=200V and b) ΔV_{GEM4}=300V.

the sensitive electronics [79]. In addition, the anode signal contains a slow component due to drifting ions, which is not present in the regular multi-GEM operation mode and could be of a disadvantage.

6.5 Discussion and conclusions

The attempt to minimize ion back-flow in a 4-GEM detector by an optimization of the electric fields was only partly successful. Although a 2–3 fold reduction of the ion back-flow could be obtained, one is compelled to work in rather extreme operation conditions, sometimes close to the breakdown point of the GEM elements. Furthermore, the lowest ion back-flow achieved of $\sim 10\%$, is still orders of magnitude too large to allow for single photoelectron detection in GPMs with visible light sensitive photocathode or in TPCs, where ion back-flow values as low as 10^{-4} are requested (Sec. 5). It is obvious from our results, that the sole optimization of the field conditions of a GEM detector layout, is not sufficient for attaining the required low ion back-flow values.

Similar results are reported in [127], where the ion transport through a single GEM element was measured to be $\sim 60\%$, independent on the gas mixture. The ion transport through 4 GEMs should thus be suppressed by approximately $0.6^4 = 0.13 = 13\%$, which is close to the results of our measurements. The influence of the hole shape and hole diameter on the ion back-flow was investigated by others [127, 99]. Two cases were studied: single-conical hole-shape GEMs (see Sec. 2.7.3) with the narrow opening facing the approaching ions and the insertion of a GEM with small hole diameter (40 μm) in-between GEMs with large hole diameter (80 μm). Both approaches allowed for an operation with further reduced ion back-flow, albeit only by a factor ~ 2 as compared to using an assembly of only standard geometry GEMs.

A GPM detector configuration combining 3 GEMs followed by a MHSP (see Sec. 2.7.4 and [118]), was found to further suppress the ion back-flow down to $\sim 2\%$ [120]. This additional reduction in ion back-flow by a factor $\sim$10, is attributed to the particular field configuration in a MHSP, where a large fraction of the avalanche-generated ions is already neutralized on the cathode strips and on the cathode plane below the MHSP (see Fig. 2.16). Nevertheless, the ion back-flow values are still far from the $10^{-3} - 10^{-4}$ value requested for the application to visible light sensitive GPMs.

The lack of gas detectors operating with low ion back-flow values triggered the development of other gaseous detector concepts, designed for better ion suppression. Examples are the ion trap detector [143] and the reverse-MHSP [144, 145, 146]. Simulations and first experimental results indicate some of these schemes, of superior ion back-flow suppression capabilities, could become potential multipliers of GPMs with visible light sensitive photocathodes.

7. GATED OPERATION OF GPMS

7.1 Introduction to ion gating

Gating by pulsed field modifications was introduced for electrons in gas detectors for event selections in cascaded parallel grid avalanche chambers [147]. Ion gating was later introduced for suppressing space-charge effects in TPCs [148]. We adopted ion gating to reduce the ion back-flow in GPMs down to very low values, ultimately allowing for the operation of ion feedback-free visible-light sensitive GPMs.

Ion gating exploits the fact, that ion drift velocities are typically 2–3 orders of magnitude smaller than that of electron. The fast electron-generated anode signal can therefore be used to trigger a potential change in the detector, while the ions are still close to their production point, to deflect them – preventing their impact on the photocathode. This necessitates the introduction of an *ion gate*, e.g. a set of parallel wires alternatingly interconnected, incorporated between the amplifying elements and the photocathode of the GPM, controlling the charge transfer between these two stages.

A schematic illustration of a 3-GEM GPM with gating electrodes preceding GEM1 and a semi-transparent photocathode is shown in Fig. 7.1. In the *open-gate* mode, an equal potential is applied to the two wire sets, the *offset voltage* V_{gate}. In this condition, electron and ion transport through the gate is uninterrupted, provided the electric fields above (E_1) and below (E_2) are chosen adequately. In the *closed-gate* mode, ion and electron transport is blocked by applying to the *positive* and *negative* wire groups respective pulsed *gating voltages* of $+\Delta V_{gate}$ and $-\Delta V_{gate}$. The switching of these two wire sets with pulses of equal

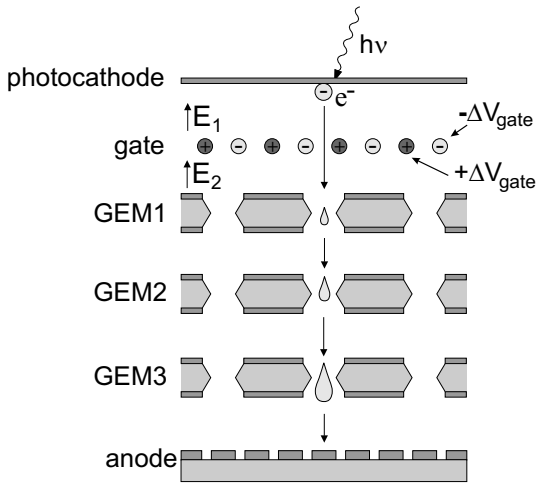

Fig. 7.1: A 3-GEM photon detector incorporating an ion gating grid between GEM1 and a semi-transparent photocathode.

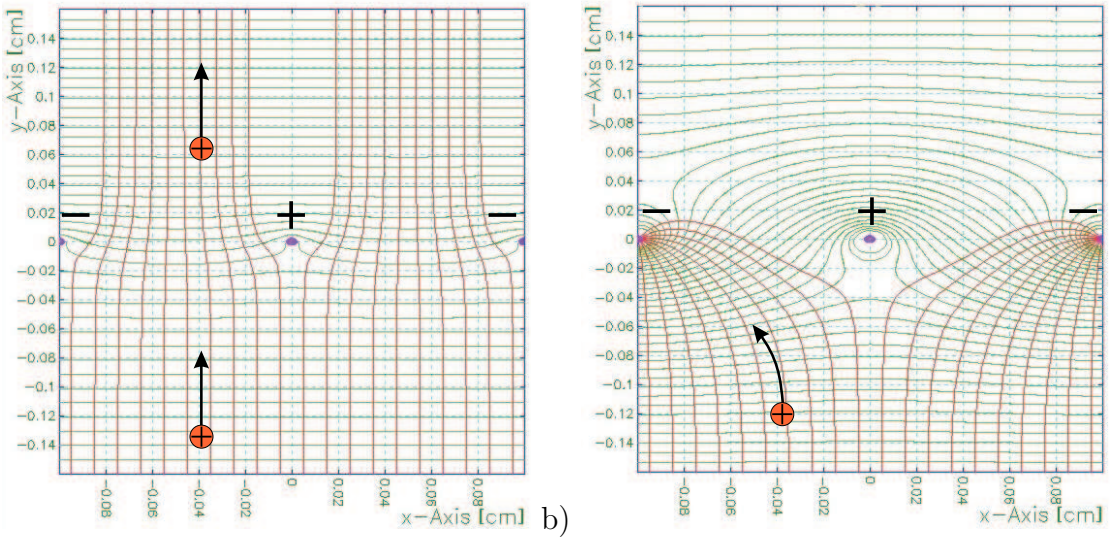

Fig. 7.2: Simulated ion drift lines in atmospheric CH_4 (starting from the bottom of the pictures) and equi-potential lines (horizontal lines) in the vicinity of the gating electrode. The wires (50μm in diameter, 1 mm apart) are shown as black dots. a) In open mode (ΔV_{gate}=0V) ions can pass through the gating grid, while in b) closed mode($\pm\Delta V_{gate}$=275V) all ions are blocked.

shape and amplitude but of opposite polarity, considerably reduces the capacitive pick-up on the detector's readout electrode, as discussed in [147].

Ions drifting towards the closed gate are deflected by the positive wires and neutralized on the negative ones. The ion transmission through the gate depends mostly on ΔV_{gate}, but also on the wire spacing, wire diameter and the electric fields below and above the gating grid [149]. The functionality of the ion gate is illustrated qualitatively in Fig. 7.2 for the open- and closed-gate modes and electric fields below and above the gate of E_1=2 kV/cm and E_2=3 kV/cm respectively (see Sec. 7.3.1). It shows simulated ion drift lines in atmospheric CH_4 in the vicinity of the gating grid. While in open-gate mode all ion drift lines pass through the gate, ion transport is completely blocked by the closed gate ($\Delta V_{gate} = \pm 275$ V) as all ion drift lines end on the *negative* gate wires.

As the majority of avalanche ions is generated in the holes of the last GEM, the spatial extension of the ion cloud is of the order of the GEM thickness (50 μm). For typical ion mobilities ($\sim$ 0.5-2.5 $\frac{cm^2}{V \cdot s}$ in atmospheric pressure gases) in an electric field of 2–4 kV/cm, this corresponds to a spread in the ion arrival-time to the gate of $\sim$1–10 μs. In order to effectively block the ion back-flow, the gate has to be closed for at least this time period for each event. This introduces a dead-time, imposing in these conditions a counting rate limit of $\sim 10^5$ Hz; it is acceptable in many but not in all applications. Larger counting rates can be achieved by subdividing the gate and the anode electrode into many independent segments.

7.2 Experimental setup

The performance of ion gating was investigated in a setup of GPMs with CsI photocathodes. The gating electrodes were realized on G-10 frames with 50 μm diameter wires, 1 mm apart, alternately interconnected (see Sec. 3.6.1). Other detector elements employed, like GEM electrodes, MWPCs and meshes, are described in previous sections and in Sec. 3.

Two methods were used to evaluate the operation characteristics and the ion back-flow suppression of the ion gate: DC current measurements and ion-feedback pulse recording. Similar to experiments described in previous sections, in DC measurements the charge transfer properties of the detector are deduced by measuring DC detector currents induced by constant UV-light illumination of the photocathode. DC potentials were supplied to the gating wires by individual power supplies. Current measurements are rather straightforward: they do not require the complex electronics needed for high-voltage switching on the gating electrodes and for pulse processing. Furthermore they were realized with GPMs having CsI photocathodes in atmospheric pressure gas; conditions where ion feedback effects are practically nonexistent.

Naturally, only in a pulsed operation mode, the gate's efficiency to suppress ion feedback can be studied. In this operation mode, flashes of UV-photons from a H_2-discharge lamp generated bunches of photoelectrons on the photocathode that were subsequently amplified; the generated avalanche ions subsequently induced ion feedback pulses on the photocathode. The yield of the feedback pulses was used to deduct the *ion feedback suppression* capability of the gate.

In pulse-mode, the potentials on the gate wires were controlled by a dedicated high-voltage pulser, developed for ion-gating in TPC's[1]. It requires three input voltages: V_{gate} and $V_{gate} \pm \Delta V_{gate}$. A TTL logic pulse (+5 or 0 V) controls the HV-pulser switching between open-gate (all wires on V_{gate}) and closed-gate (wires alternately on $V_{gate} \pm \Delta V_{gate}$).

7.3 Current-mode measurements

A series of DC current measurements were performed to evaluate the influence of the gating voltage ΔV_{gate} and the electric fields E_1 above and E_2 below the gate, on the electron and ion transfer through the gating electrode.

7.3.1 Electron transmission through the gate

In the open-gate mode ($\Delta V_{gate} = 0$) full photoelectron transmission through the gate is reached by setting the right ratio of the electric fields E_1 and E_2 above and below the gate (Fig. 7.3a); to some extent it also depends on the gas mixture and pressure [149]. In the setup schematically depicted in Fig. 7.3a, I_{mesh}, the fraction of the photocurrent that passes the gate, is recorded as a function of E_2. Normalized to the total photocurrent this measurement yields the electron transmission through the open gate.

[1] The electronic scheme and operation of the HV-pulser is described in detail in [149].

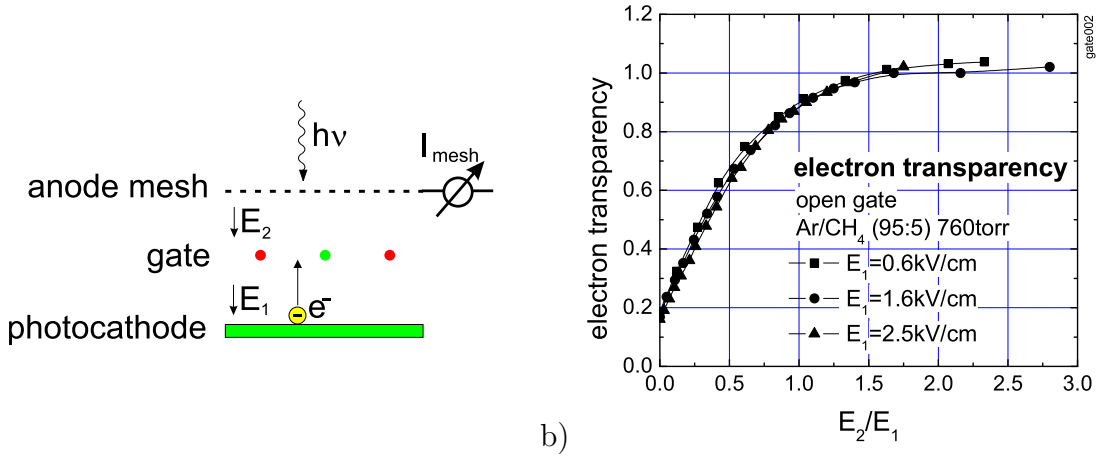

a) b)

Fig. 7.3: a) Schematic illustration of the experimental setup used for measuring the electron transmission through an open gate (ΔV_{gate}=0). b) Electron transmission through an open gate as a function of the ratio of E_2/E_1, the field below and above the mesh.

As can be seen in Fig. 7.3, the electron transmission does not depend on the choice of the individual electric fields but only on the ratio between the two. A field ratio $E_2/E_1 \geq 1.5$ guarantees full electron transmission through the open gate. In subsequent experiments the fields on both sides of the gate were chosen accordingly.

7.3.2 Ion transmission through the gate

For fixed electric fields E_1 and E_2, the ion transmission of the gate depends only on the gating voltage ΔV_{gate}. Simulation results of the gate's ion transparency in atmospheric CH_4 (Fig. 7.4) show a strong drop of the ion transmission at gating voltages above 150 V.

Similar results were obtained experimentally in a setup schematically depicted in Fig. 7.5. A constant flux of photoelectrons is emitted from the photocathode and drifts towards the

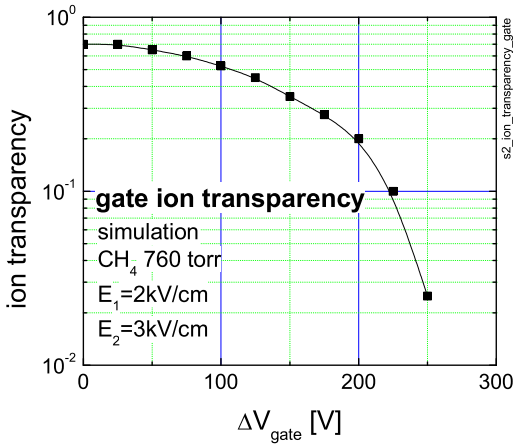

Fig. 7.4: The simulated ion transmission through the gating electrode in atmospheric CH_4 as a function of ΔV_{GEM} for E_1=2kV/cm and E_2=3kV/cm.

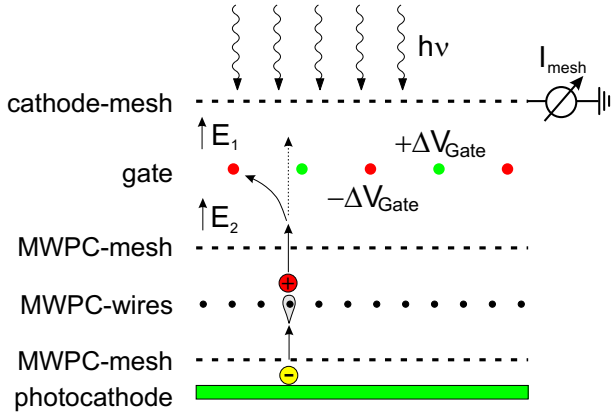

Fig. 7.5: Schematic experimental setup for measuring the ion back-flow suppression with a gate; the MWPC acts as an *ion generator*.

MWPC wires where gas multiplication takes place. The MWPC serves here as an *ion generator*; avalanche-ions are either collected on the photocathode or drift through the upper MWPC mesh towards the gate wires.

With a constant field E_2, the MWPC generated a *constant flux of ions* arriving at the gate, independent on the choice of the gating voltage ΔV_{gate}. The intensity of the ion flux could be controlled by tuning the MWPC multiplication. A fraction of the ions is transferred through the gate, collected on the cathode mesh and recorded as a current I_{mesh}. To obtain the gate's ion transparency, I_{mesh} was normalized to the total ion current arriving on the gate electrode, measured subsequently on the interconnected gating wires and cathode mesh with otherwise equal conditions.

The gate's ion transparency was determined in atmospheric Ar/CH_4 (95:5) as a function of ΔV_{gate} for several values of E_1. The results are presented in Fig. 7.6a. Very low ion transparencies approaching 10^{-4} were reached in all three field conditions applied. This value does not necessarily represent the gate property but is rather the lower limit of the measurement, determined by the maximum currents that could be generated by the MWPC (~ 0.5 μA) and by the accuracy of the pico-ampermeter recording I_{mesh}.

The absolute value of the ion transparency depends only on the ratio of the gating voltage and electric field E_1. This is clearly illustrated by the overlapping curves of Fig. 7.6b, showing the the ion transparency as a function of the ratio $\Delta V_{gate}/E_1$ for three different values of E_1. Also the simulation results for CH_4 (Fig. 7.4) follow this behaviour, indicative of the independence of the ion drift properties from the gas mixture reported also elsewhere [127, 99]. The linear dependence of the ion transparency on the field E_1 for a constant value of ΔV_{gate} was also observed by others [149], reporting an ion transparency of $\sim 1\%$ for ΔV_{gate}=80 V and E_1=0.3 kV/cm with a gate having 75 μm diameter wires, 1.25 mm apart. The considerably lower suppression seen in Fig. 7.6a for ΔV_{gate}=80 V despite working at higher fields (E_1=0.6 kV/cm), is attributed to the thinner wires (50 μm) and closer spacing (1 mm) of our gating grid, generating more intense electric fields around the ion-gate wires.

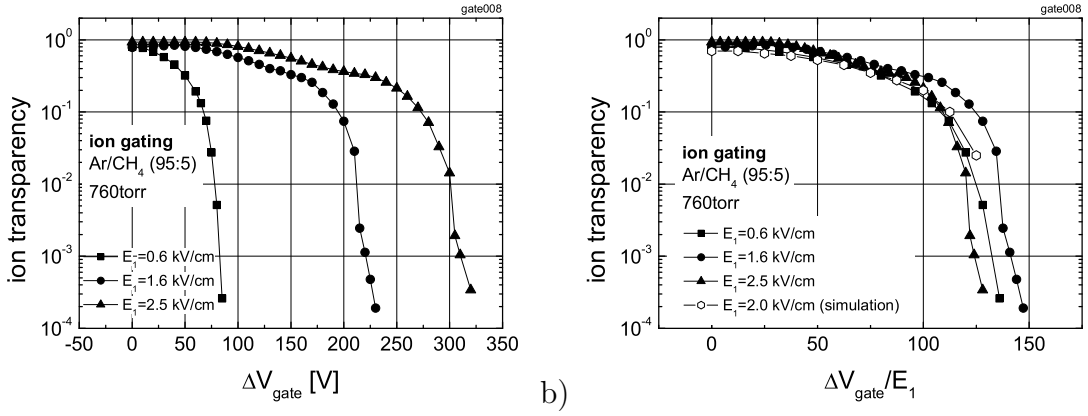

Fig. 7.6: Measured ion transmission through the gate as a function of a) ΔV_{gate} and b) of $\Delta V_{gate}/E_1$. The overlapping curves in b) indicate an almost identical dependence of the ion transmission on $\Delta V_{gate}/E_1$.

7.4 Pulse-mode measurements

Measurements in pulse mode require operation conditions, where ion-feedback pulses occur and can be observed. In GEM-GPMs with CsI photocathodes, operated in atmospheric gas mixtures, ion-feedback effects are not observed (see Sec. 5); such effects were reported for a GEM-MWPC configuration at *low pressure* (40 torr) Ar/C_2H_6 [150]. Therefore, to investigate the gate's efficiency in a pulse-mode, we operated a GEM-GPM with reflective photocathode at low gas pressure (100 torr and less). The more involved operation of gated GPMs with visible-light sensitive K–Cs–Sb photocathodes was approached differently, as discussed in Sec. 8.

It is important not to confuse the *ion-feedback suppression* measured in pulse mode with the *ion transparency* obtained from DC-current measurements described above. The latter describes just the fraction of incoming ions passing the gate, while the former characterizes the gate's ability to suppress ion-feedback pulses. Owing to their high drift velocity, secondary electrons generated by ion impact on the photocathode will arrive at the gate while it is still closed and will not be recorded on the anode. The ion-feedback suppression capability is therefore the combined result of the ion *and* the electron blocking. For a given gating voltage ΔV_{gate} it is always better than the ion blocking alone.

For reasons of convenience, instead of using the anode pulses suggested above, the trigger output of the H_2 flash-lamp was converted to logic TTL pulse with variable pulse duration and delay and utilized for triggering the HV pulser. The timing sequence of the triggering scheme is illustrated in Fig. 7.7. In the displayed example[2] the pulse duration and delay time were 35 μs and 20 μs respectively, adequate for the ion's arrival time and time spread at the gate. The present HV-pulser electronics opens the gate for *high* TTL pulses (+5 V)and closes it for *low* pulses (0 V).

The offset voltage V_{gate} was set to zero and the gating voltages ΔV_{gate} were carefully adjusted in height to minimize capacitive pick-up on the anode; the latter was further reduced by

[2] The timing corresponds to the experiment described in in Sec. 7.4.1.

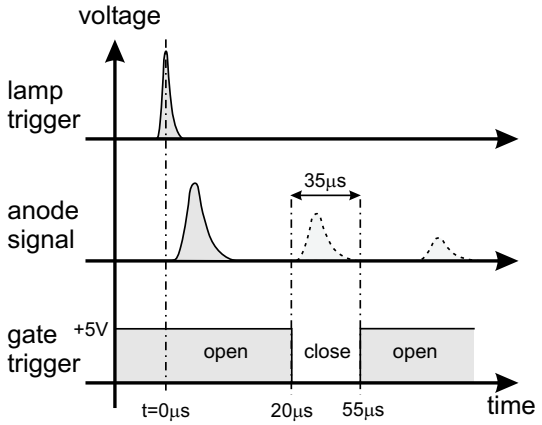

Fig. 7.7: Timing sequence of the trigger for the HV-pulser unit.

inserting an additional R-C element between the HV-pulser output and the gating wires, shaping the rise-time of the HV-pulses to ~ 700 ns.

Despite these efforts, the pulsing-induced capacitive pick-up on the anode was still large, exceeding the event's pulse height. However, holding up the signal with a sufficient delay, the signal could be *extracted* out of the pick-up and it did not affect our measurements.

7.4.1 Gated GEM + MWPC combination

We operated a GEM-MWPC structure at 40 torr Ar/CH_4 (95:5), in the testing setup schematically shown in Fig. 7.8. Only at such a low gas pressure did we observe ion-induced feedback pulses.

The GPM employed a standard GEM element coated with a reflective CsI photocathode, followed by a ion gate and a MWPC element. This GPM constitutes a relatively easy-to-operate double stage device, working stably at gains of up to 10^4, with the ion gate controlling the charge transport between MWPC, the main generator of avalanche ions, and the GEM. All electrodes were connected through protection resistors to individual power supplies, except the gating wires' potentials that were controlled by the HV-pulser.

Under pulsed UV illumination (pulse duration $\ll 1ns$), a large number of photoelectrons (~ 1000) is emitted from the photocathode and guided into the GEM holes, where they experience gas multiplication. The avalanche electrons are transferred through the open gate to the MWPC for a subsequent second stage amplification. On the MWPC anode the signal is recorded by an electronic readout circuit, capacitively decoupled from the MWPC high voltage. Of the ions produced in the MWPC stage and drifting towards the gate, some manage to pass the MWPC mesh and the gate and subsequently impinge on the photocathode, inducing secondary electron emission (see Sec. 5). A fraction of the secondary electrons generated on the photocathode are also blocked by the still closed gate and do not contribute to the ion feedback pulses.

We noticed a strong dependence of the ion feedback intensity on the GEM potential ΔV_{GEM}: for the same total detector gain, ion feedback was considerably more pronounced when working with high GEM gain and low MWPC gain than when sharing the gain equally, even

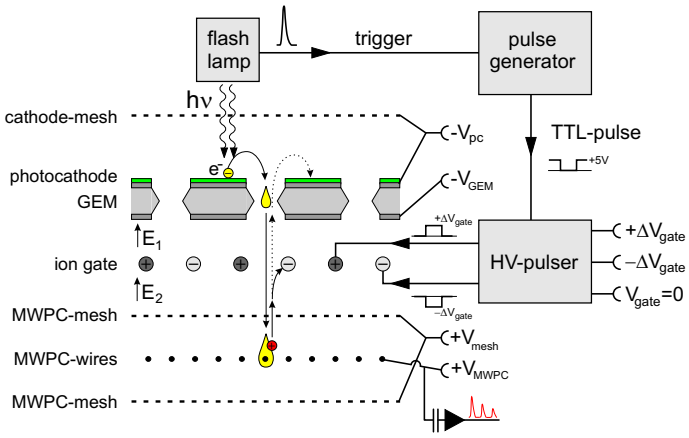

Fig. 7.8: Schematic view of the MWPC-GEM detector for evaluation the gate's efficiency in suppressing ion feedback.

for an open ion gate. Similar observations are reported by the authors of [150]. This fact indicates an influence of the ion's kinetic energy on the feedback process. It seems that if the ion kinetic energies exceed ~ 1 eV, as is the case at low pressures and in the high field region close to the GEM holes, the kinetic energy starts playing an important role in the ion feedback process. Therefore unlike at atmospheric pressure, both potential and kinetic ion energy can contribute to secondary electron emission. The apparent increase in γ_+ at low gas pressures is an interesting phenomenon and can be of use in applications, aiming to detect ions by the secondary electron emission they induce on surfaces.

We observed a sequence of several generations of feedback pulses on the anode, as can be seen in Fig. 7.9a, the feedback generation time corresponds to the ion drift time from the anode wires to the photocathode. With increasing gating voltage ΔV_{gate}, the intensity of ion-feedback pulses diminished and finally they vanished (Fig. 7.9c), due to the reduced ion- and electron-transparency of the gate in closed mode. The *ion feedback suppression* capability of the gate is shown in Fig. 7.10 as a function of ΔV_{gate}. It was defined as the pulse-height ratio of the first secondary pulse and the primary pulse.

Similar to the results of the gate's ion transparency obtained in DC mode, the ion-feedback drops very fast with increasing ΔV_{gate}, reaching values of $\sim 10^{-3}$ at 80 V. At this value, secondary pulses were no longer discernible, constituting the lower limit of the measurement. Even higher ion feedback suppression factors can be expected with further increasing values of ΔV_{gate}.

7.4.2 Gated 4-GEM operation

We operated a 4 GEM detector with reflective photocathode, incorporating the ion-gating electrode described above. As only ions produced below the gate can be stopped, it would be best placed between GEM1 and GEM2. But due to a limited voltage ($V_{gate} \pm \Delta V_{gate}$) the high voltage pulser could supply to the gating electrodes, the gate was placed between GEM3 and GEM4 instead and operated with V_{gate}= 0 V. A resistive network provided the other electrodes with the required potentials. The charge signals from the anode were capacitively decoupled from the positive high voltage and supplied to an electronic readout

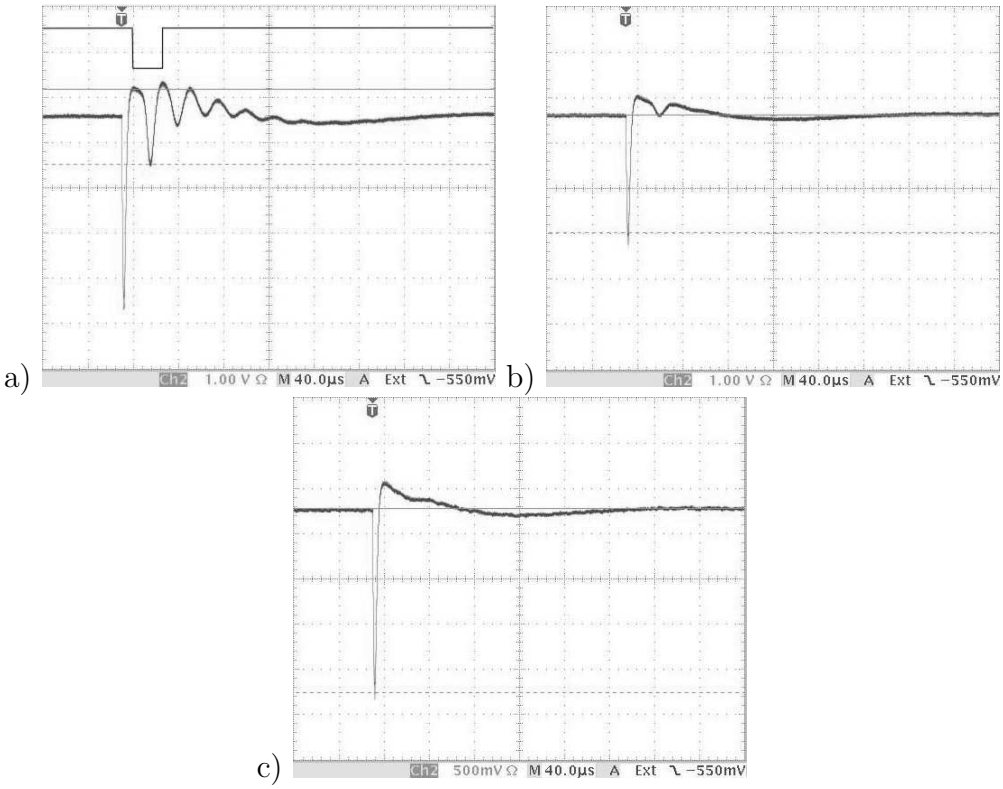

Fig. 7.9: Oscilloscope pictures of pulses measured on the multiwire anode for a) ΔV_{Gate}=0V, b) 50V and c) 80V. In a) the logic trigger pulse used to open and close the gate is also included. Time scale 40μs/div.

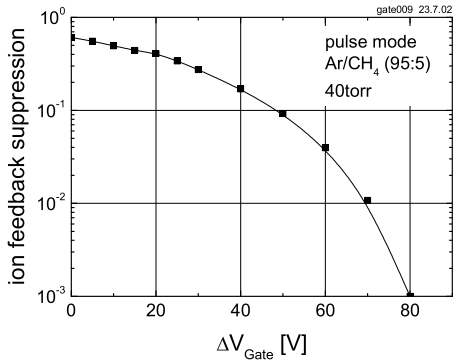

Fig. 7.10: The ion feedback suppression as a function of ΔV_{Gate} in pulse mode. For ΔV_{Gate}=80 V no secondary pulses were observed.

circuit consisting of a pre-amplifier, timing filter amplifier (TFA) and digital oscilloscope. The waveforms observed on the oscilloscope were stored and analyzed in a PC. The trigger for the high voltage pulser and for the data storage was supplied by the H_2 flash lamp illuminating the CsI photocathode on the top face of GEM1. Fig. 7.11 schematically shows the experimental setup.

The detector was operated at 100 torr of CH_4, in order to deliberately promote ion-feedback

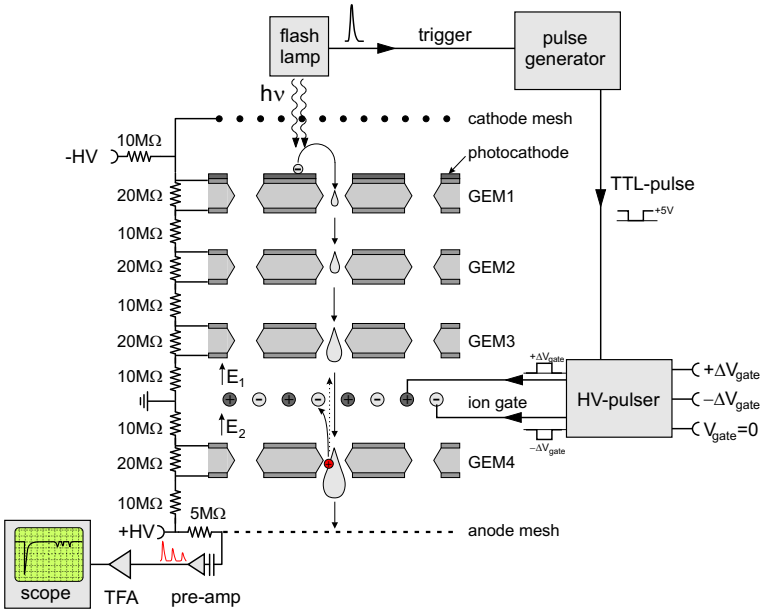

Fig. 7.11: Schematic illustration of the gated 4-GEM GPM experimental setup.

on the CsI photocathode (see Sec. 7.4). The pulsed H_2 lamp induced ∼1000 photoelectrons per light-pulse; they were subsequently multiplied in the four successive GEM stages. At a total gain $> 10^5$ the detector electronics was sensitive to single photoelectrons. Due to the low pressure, the avalanche is no longer confined but extends out of the GEM holes. The avalanche extension induces a spread of the ion's arrival time at the photocathode. This explains the manifestation of the ion feedback effect as a series of individual ion-induced single-electron pulses, rather than a single but large secondary ion feedback pulse. They are spread in time over ~ 10 μs and appear approximately 45 μs after the primary pulse (Fig. 7.12); the ~ 45 μs generation time is in good agreement with the ion's drift time from GEM4 to the photocathode.

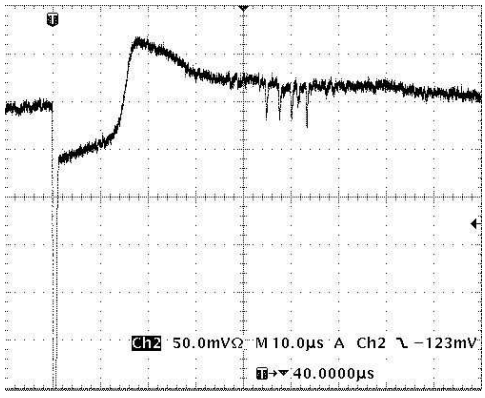

Fig. 7.12: A single-event pulse recorded on the 4-GEM anode, induced by a multiple photon burst hitting the photocathode. At least four ion-induced feedback pulses are discernible ∼45 μs after the primary pulse. The primary pulse is not shown in full height. Time scale: 10μs/div.

After accumulating a few thousand waveforms for different gating voltages ΔV_{gate}, the average number of feedback-induced single-electron pulses was determined. This number is proportional to the ion feedback intensity and allowed the determination of the ion feedback suppression capability of the gate as a function of ΔV_{GEM} (Fig. 7.13). At a voltage of 80V the after-pulses were 10^4 times less frequent than with an open gate. Lower ion feedback suppression values could not be measured due to statistical limitations of the measuring system. Again it is important to note, that the ion feedback is suppressed both by reducing the ion back-flow and by stopping secondary electrons at the gate.

Unfortunately, only a qualitative comparison with the previous results presented above is possible, as different transfer fields, gas mixtures and pressures were used in the experiments. Nevertheless, one easily recognizes the fast drop of the ion feedback with increasing gating voltage ΔV_{gate} already noted in Fig. 7.10 and in Fig. 7.6 measured in current mode.

7.5 Discussion and conclusions on the gated GPM operation

We have shown that the ion back-flow could be reduced by four orders of magnitude by incorporating a pulsed gating electrode with alternatingly polarized wires into the cascaded GEM detector. Ion feedback is even further suppressed due to the additional stopping of secondary electrons at the ion gate. Albeit no higher ion feedback suppression than $\sim 10^{-4}$ could be measured due to limitations in the dynamic range of the measurements, it can be expected that it can be completely inhibited by active ion gating with reasonable gating potentials ΔV_{gate}.

The demonstrated ion feedback suppression levels are sufficient for most applications, particularly for the operation of high-gain GPMs with visible-sensitive photocathodes, as demonstrated in Sec. 8.

The gating restricts the rate capability of the detector due to the dead-time caused by a closed gate and segmenting the anode and gate electrodes is recommended; in addition it

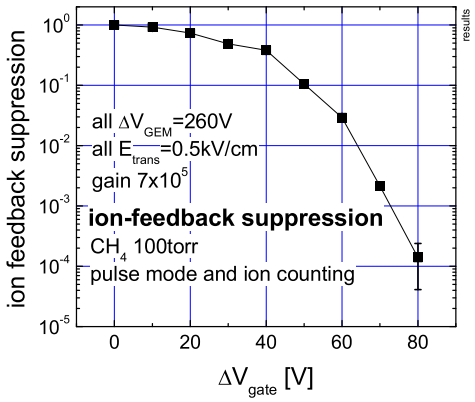

Fig. 7.13: The ion feedback suppression as a function of ΔV_{Gate} in pulse mode in a 4-GEM detector operated at 100Torr CH_4 with transfer fields of 0.5kV/cm and equal GEM voltages of 260V.

should minimize the capacitive pick-up.

8. GATED OPERATION OF VISIBLE-SENSITIVE GPMS

8.1 Introduction

The results on ion gating of Sec. 7 were applied in a cascaded GEM-GPM with a semi-transparent K–Cs–Sb photocathode, capable to operate at gains sufficient for single-photoelectron detection. By incorporating an ion-gate between the first GEM and the photocathode, the already low ion back-flow in the cascaded GEM was further reduced to levels below 10^{-5}. Ion-feedback effects are extremely low in such conditions and should therefore no longer limit the maximum detector gain (Sec. 5.2). To allow for a flexible detector assembly, the experiments were performed inside the photocathode preparation system rather than in a sealed package, similar to the experiments described in Sec. 5.

The preparation of a multi-GEM detector with gating electrodes, compatible with ultra-high vacuum conditions, coupling it to a K–Cs–Sb photocathode and operating it inside the photocathode preparation system was nevertheless a challenging task. It consisted of assembly of an electron multiplier made from clean materials only; baking it to 200°C; solving pick-up noise issues from the vacuum pumps and gauges; preparation of stable, high QE K–Cs–Sb photocathodes; preparation of dedicated multiple HV electrical connections between the detector electrodes and the external of the chamber, etc. A large effort went into the design and preparation of the bakeable ultra-clean electron multiplier; a description of the design, materials and methods is provided in App. A.

8.2 Experimental setup

The electron multiplier (see Fig. 8.1) consisted of four 30×30 mm^2 Au-coated GEMs of standard dc140 geometry (see Tab. 2.1) followed by an anode made from a thin sheet of stainless steel. The detector elements were held in place and separated from each other by 1 mm thick alumina-ceramic frames with a central opening of 20×20 mm^2, defining the active area of the electron multiplier. An ion-gate was placed 1 mm above the top-most GEM and 5 mm below the photocathode. It consisted of parallel Au-coated tungsten wires, 50 μm in diameter and 1 mm apart, assembled on a ceramic frame. The preparation of the gate-electrode and all details of the electron multiplier assembly are provided in App. A.

Following the assembly, the detector was first tested in 700 torr of Ar/CH_4 (95:5), in the test chamber (see Sec. 3.6.2) in combination with a semi-transparent CsI photocathode; it was then investigated inside the sealing chamber of the bi-alkali photocathode fabrication system (see Sec. 3.1). Fig. 8.1 shows schematically the detector setup and the resistor network used for powering the individual electrodes. A part of the resistor network had to be placed inside the sealing chamber as the number of HV feedthroughs was limited.

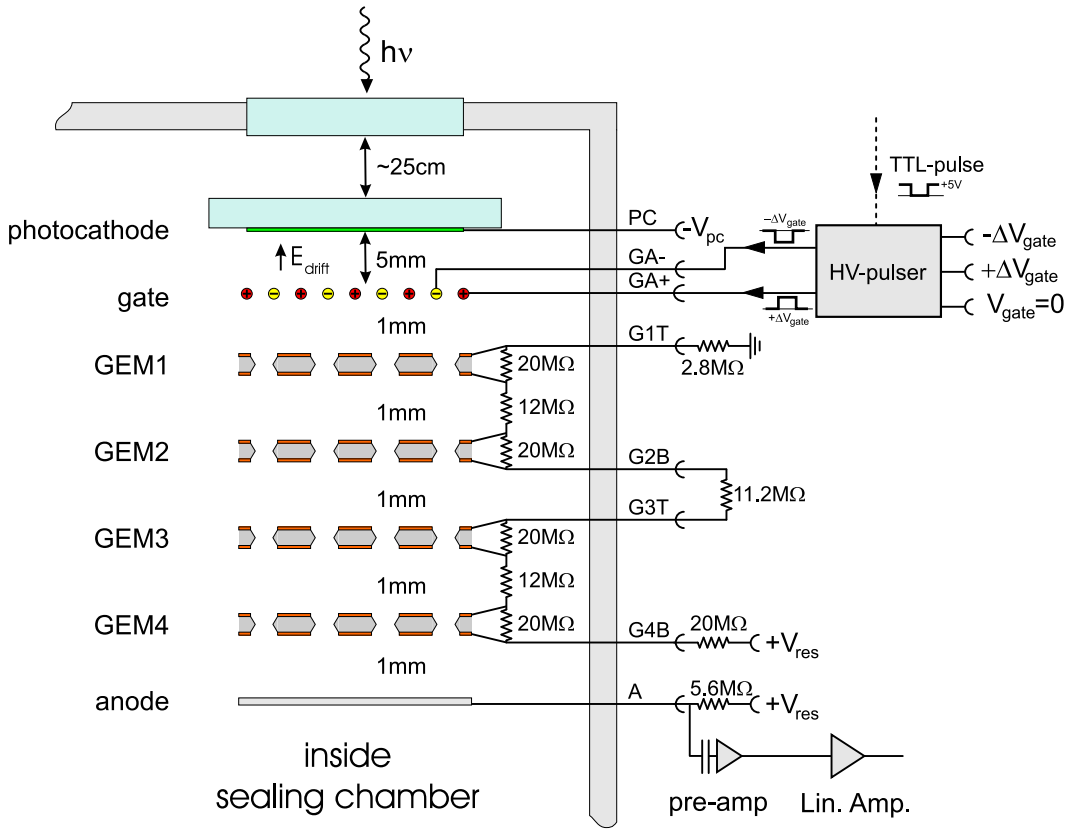

Fig. 8.1: Schematic illustration of the gated visible-sensitive GPM detector setup and its resistor network. The feedthroughs of the vacuum chamber to the outside are labeled PC for photocathode, $GA+$, $GA-$ for the gate electrodes, $G1T$, $G2B$, $G3T$ and $G4B$ for the GEM contacts and A for the anode.

Voltage limitations of the HV-pulser required an operation with a gate offset voltage of zero (V_{gate}=0). The same potential V_{res} was applied to the anode and to the resistor network V_{res}, with the induction field defined by the potential drop on the resistor between the feedthrough $G4B$ and the power supply of the resistor network (Fig. 8.1). Despite the same potential V_{res} applied, a separate power supply[1] was used to provide the anode voltage; it allowed measuring the anode DC current with an accuracy of ±0.1 nA. Monitoring the anode current was a convenient method to note unstable detector conditions and to prevent discharges in the detector. When strongly fluctuating anode currents exceeding ∼1 nA were noticed, the voltage on the resistor network was lowered by ∼100 V, reducing the detector gain. After a few minutes stability was reached and the potential could be raised to its normal value. Not lowering the voltage in case of observed fluctuations in the anode current often resulted in breakdown. An identical power supply was employed for the negative potential V_{drift} to the photocathode for monitoring the photocurrent.

Capacitively decoupled from the anode high voltage, the charge signal was recorded by a charge sensitive pre-amplifier[2] followed by a pulse-shaping timing-filter amplifier (TFA)[3]. The pulses were either observed on a digital oscilloscope or fed into a multi-channel analyser

[1] model N471A, 2-channel HV power supply, CAEN
[2] model 109A, ORTEC
[3] model 454, ORTEC

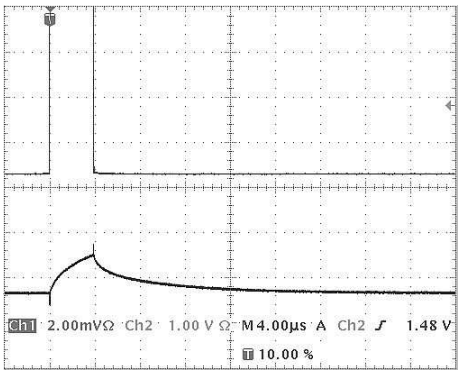

Fig. 8.2: The light emission of the pulsed UV-LED measured on a PIN-photodiode (bottom line) under the application of a 6V square pulse (top line) to the LED. The 4 μs square pulse applied is shorter than the rise- and fall time of the UV-light output intensity of $\sim$10μs.

(MCA)[4]. For obtaining pulse height spectra, it was necessary to include a linear gate and stretcher module[5] in-between the TFA and the MCA to compensate for base-line shifts of the pulses.

As light source we employed a UV-LED[6], whose narrow spectral emission around 375 nm coincides with the sensitivity peak of K–Cs–Sb photocathodes. By applying short voltage pulses to the LED, a tunable "flash lamp" was realized; the emitted light intensity could be conveniently controlled by adjusting the height and width of the voltage pulse, down to the single-photon level. Fig. 8.2 shows the response of a PIN photodiode to the UV-LED light, applying 4 μs wide square pulses of 6 V. As a result of its intrinsic capacity, the light output intensity of the LED rises and falls with a characteristic time constant of ~ 10 μs.

The LED light was transmitted with an optical fiber and focused by a small lens to illuminate a $\sim$ 3 mm diameter spot in the center of the photocathode through the top sapphire window of the sealing chamber.

8.3 Preparative measurements

Following the assembly, the detector was mounted in the testing setup (see Sec. 3.6.2) in combination with a semi-transparent CsI photocathode for functionality tests. Using an identical resistor network to the one shown in Fig. 8.1, the detector gain was determined in current mode under constant UV illumination (see Sec. 3.7.1). The resulting gain-voltage characteristic of the 4-GEM-GPM with ion-gate[7] in 700 torr of Ar/CH_4 is provided in Fig. 8.3. To avoid risks of discharge, we limited the voltages on the GEMs to ΔV_{GEM}=325 V, corresponding to a total gain of $8 \cdot 10^5$.

The detector was subsequently operated in pulse mode with a H_2 flash lamp, up to a gain of $\sim 10^6$. Although no ion-feedback signals were observed, the gate was operated at ΔV_{gate}=200 V to verify its operation and assessing the magnitude of the capacitive pick-up.

[4] MCA8000A, Amptek
[5] model 542, ORTEC
[6] NSHU590A, Nishia Corp.
[7] The gate was kept open at all times in current mode measurements.

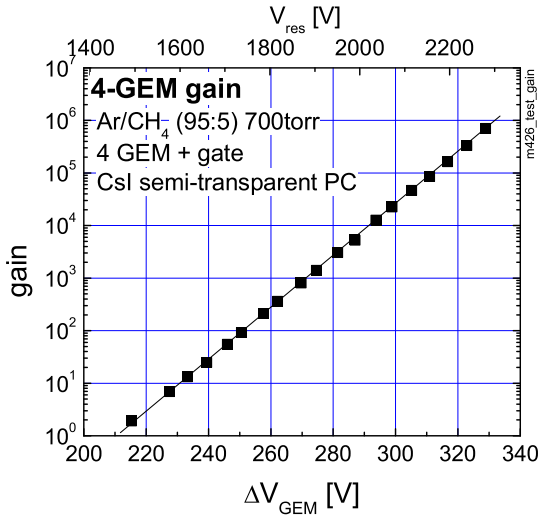

Fig. 8.3: The gain of the gated 4-GEM detector with a CsI photocathode operated in 700 torr of Ar/CH_4 (95:5), as a function of the GEM voltage ΔV_{GEM} (bottom scale) and of the voltage on the resistor network (top-scale).

Subsequently, the electron multiplier was introduced into the sealing chamber of the K–Cs–Sb photocathode setup by plugging the ceramic detector-base into the ceramic package-holder (see App. A). The photography of Fig. 8.4 shows the assembled detector mounted in the chamber. The chamber was subsequently pumped and baked for two days at 150°C, resulting in a pressure of $\sim 4{\cdot}10^{-9}$ torr at room temperature.

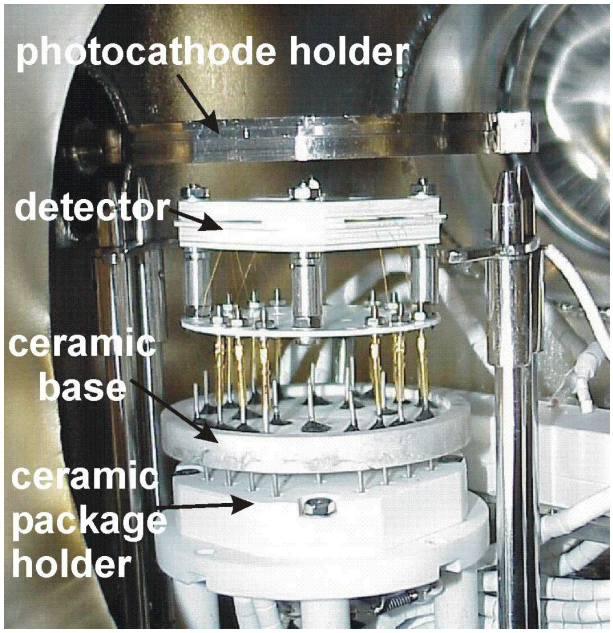

Fig. 8.4: Photography of the gatable electron multiplier mounted in the sealing chamber with a photocathode positioned on top.

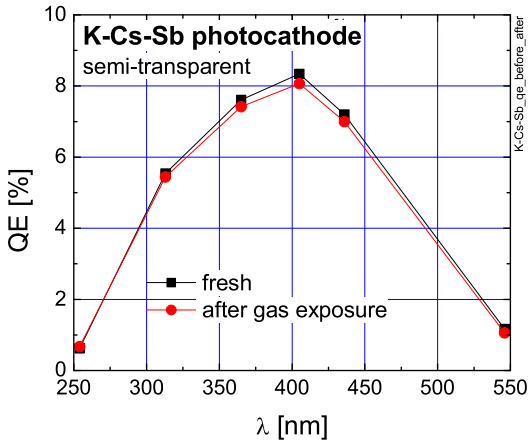

Fig. 8.5: The absolute QE of a K–Cs–Sb photocathode measured in vacuum before and after concluding the 3-day experiment.

In the meantime, a semi-transparent K–Cs–Sb photocathode was prepared and characterized in in the activation chamber of the same system. After introducing 700 torr of Ar/CH_4 (95:5) into activation and sealing chambers, the photocathode was transferred to the sealing chamber and positioned $\sim$5 mm above the gating electrode of the detector, forming the GPM. The procedures of photocathode fabrication, gas introduction to the vacuum chambers and transfer of the photocathode to the electron multiplier are described in Sec. 3.2 and Sec. 5.4.1.

During the measurements, lasting over 3 days, the photocathode's QE did hardly deteriorate. This is demonstrated in Fig. 8.5, showing an example of the absolute QE of one K–Cs–Sb photocathode, measured in vacuum in the activation chamber before and after the measurements. The small deviations are within in the measurement accuracy.

Prior to the operation in gas-avalanche mode, the detector was operated in a photodiode mode, while illuminating the photocathode homogeneously with a DC light source. The induced photocurrent was measured on the photocathode (contact *PC* in Fig. 8.1) with a pico-ampermeter while varying the voltage V_{drift}, defined as the potential difference between the photocathode and the interconnected ion-gate and top GEM1 electrodes (contacts *GA+*, *GA-* and *G1T* of Fig. 8.1). The current-voltage characteristic of Fig. 8.6 displays the expected behaviour of a steep rise, followed by a moderately rising plateau of the photocurrent as the backscattering probability drops with increasing field strength on the photocathode. In subsequent measurements a constant $V_{drift} = -100$ V was applied to the photocathode, while an offset voltage $V_{gate}= 0$ was used on the ion gate, corresponding to a drift field of $\sim$0.2 kV/cm. This value might be too low for optimal photoelectron extraction from the photocathode; it was chosen to permit operation at reduced values of the gating voltages ΔV_{gate}, while retaining a high ion-feedback suppression on the gate[8]. This was necessary, as gating voltages exceeding $\Delta V_{gate} \approx \pm 200$ V were found to cause spurious pulses in the detector after baking, presumably due to field emission from sharp edges of the gating wires.

[8] See discussion in Sec. 7.3.2 on the influence of the electric fields on both sides of the gating electrodes on the ion-back flow.

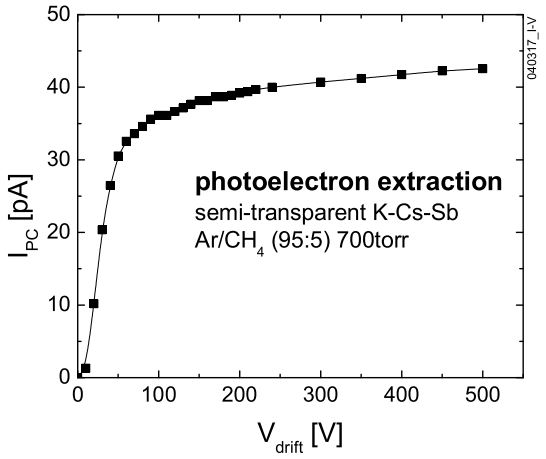

Fig. 8.6: Photocurrent extracted in DC mode from the photocathode as a function of the drift voltage V_{drift}.

8.4 Pulse-mode operation

In pulse-mode operation the detector was illuminated with short light flashes ($\leq 4\mu$s) from the UV-LED. We took a safe approach, keeping the gate closed most of the time, in order to avoid the possibility of detector breakdown caused by background-induced ion feedback, as shown in Fig. 8.7. The gate was opened only ~ 100 μs before the emission of the LED, to allow the capacitive pick-up signal induced by the high voltage switching to vanish; it was closed immediately after the observation of the anode pulse. Following the results of Sec. 7, a gating voltage of ΔV_{gate}=$\pm$150 V was applied, known to suppress the ion back-flow down to 10^{-4}, inhibiting ion feedback.

Fig. 8.8 shows charge pulses of multi-photon events recorded on the anode at ΔV_{GEM}=300V, corresponding to a gain of $3 \cdot 10^4$. The large gating-induced capacitive pick-up is dominant, as seen in Fig. 8.8a, due to a non-optimized switching electronics. The anode-signal is better

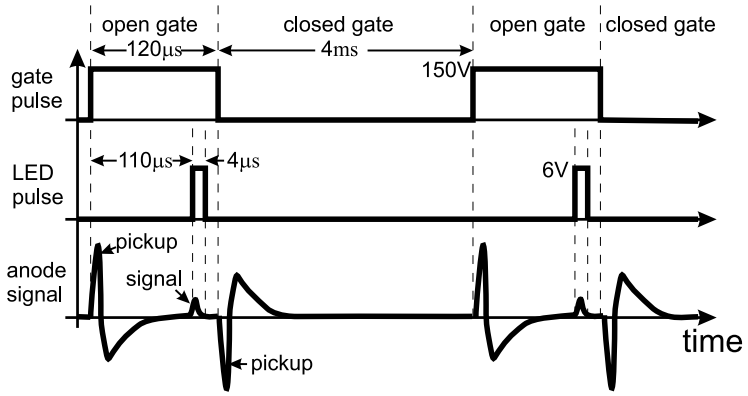

Fig. 8.7: The schematic diagram of the pulses applied to the gate pulser and to the UV-LED and the response recorded on the anode.

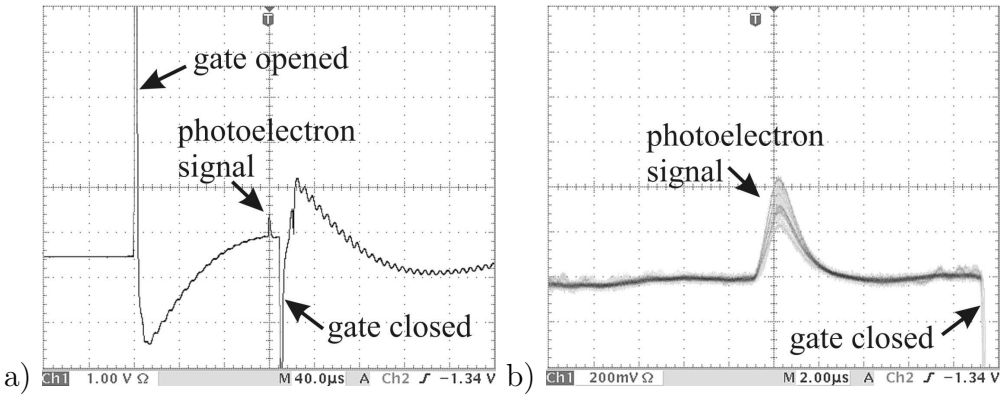

a) b)

Fig. 8.8: Anode signals from multiple photoelectrons recorded at ΔV_{GEM}=300 V. The capacitive pick-up from the high voltage switching on the gate is clearly seen. The signal originating from the photon flash is indicated in a) and is shown more clearly with a smaller time and voltage scale in b).

shown on an expanded time scale in Fig. 8.8b. As a result of the large pick-up, the anode signals had to be processed by a Timing-Filter-Amplifier (TFA) and a Linear-Gate-And-Stretcher (LGS) prior to their recording with the multi channel analyzer. Using segmented anodes for position encoding and segmented gating electrodes, will reduce the capacitive pick-up.

Fig. 8.9 shows two pulse-height spectra originating from multi-photon events. From the peak position in the spectrum and the known detector gain[9], the number of primary photoelectrons was estimated to be ∼200 and ∼20, recorded at respective detector gains of $8 \cdot 10^3$ and $5 \cdot 10^4$.

At low UV-LED intensities, the recorded photoelectron signals showed a *structure*, as shown in Fig. 8.10; each of the small peaks corresponds to a single photoelectron. This spread in time is a result of the time-width of the emitted LED light, generating photoelectrons on

[9] The gain for a given GEM voltage was taken from the current measurement of Fig. 8.3.

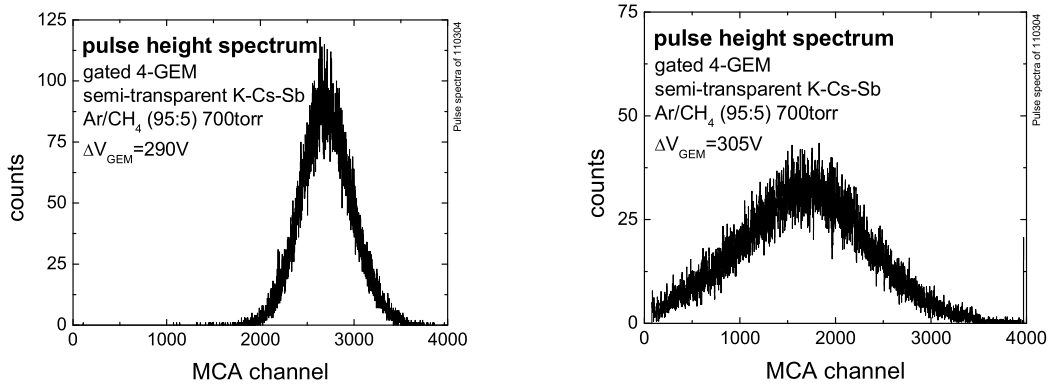

a) b)

Fig. 8.9: Pulse-height spectra recorded with the gated visible-sensitive GPM, of a) ∼200-photoelectron pulses, recorded at a gain of $8 \cdot 10^3$ and b) ∼20-photoelectron pulses, recorded at a gain of $5 \cdot 10^4$.

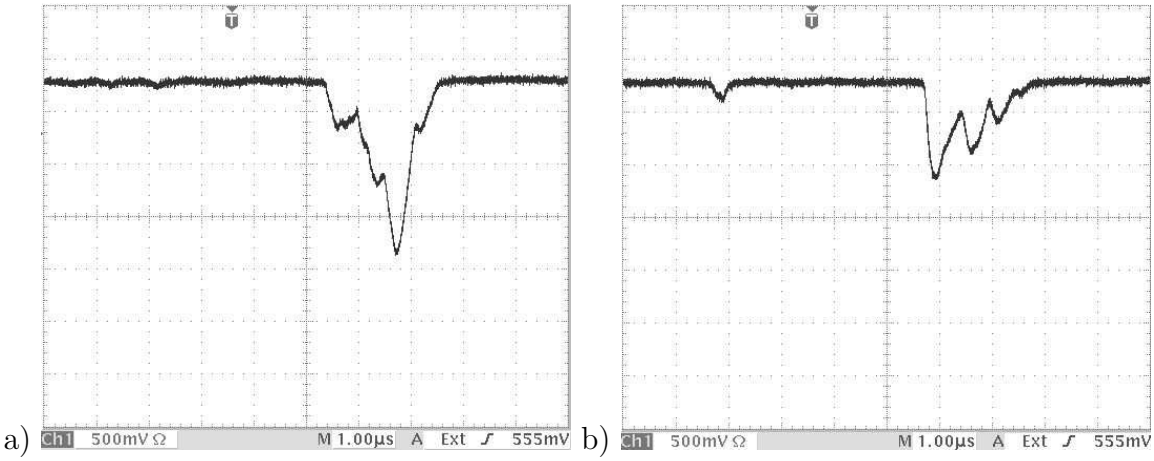

Fig. 8.10: Two examples of a single event of few photoelectrons recorded on the anode of the gated visible-sensitive GPM. The detector gain was $\sim 8 \cdot 10^4$; time scale 1 μs/div.

the photocathode over a time interval of several microseconds.

Even lower LED intensity yielded single-photoelectron pulses, observable already at a gain of $\sim 8 \cdot 10^4$ (ΔV_{GEM}=310 V). Again, resulting from the long time-width of LED light emission, the single-electron pulses are spread over a time interval of a few microseconds, as shown in Fig. 8.11. Pulse-height spectra of single-photon events were acquired for different values of ΔV_{GEM} (Fig. 8.12). The exponential-shape of the spectra proves, that the observed pulses are indeed originating from single photoelectrons. From the exponential shape of the single photoelectron spectra we determined the detector gain as described in Sec. 3.7.2.

The resulting voltage-gain characteristic is plotted in Fig. 8.13 (full circles). For lower values of ΔV_{GEM}, the amplification was not sufficient for single electron detection and therefore, the detector gain could not be determined from the slope of the single-electron pulse-height spectra. Instead, relative measurements of the pulse-height of multiple-photon events were recorded (crosses and right Y-axis). The dashed line in Fig. 8.13 indicates the gain-voltage characteristic that was obtained in current mode with a CsI photocathode (see Sec. 8.3 and Fig. 8.3). As expected, a very good agreement between the different and independent

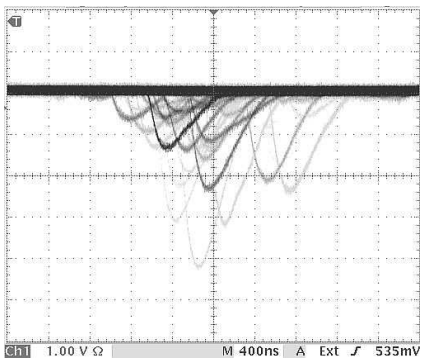

Fig. 8.11: Multiple single-electron pulses recorded on the anode of the visible-sensitive GPM at a gain of $3 \cdot 10^5$ (ΔV_{GEM}=322 V). The time jitter is due to the time-width ($\sim 4\mu$s) of the LED emission. The rise and fall times of the pulses are dictated by the 200 ns time constant of the TFA.

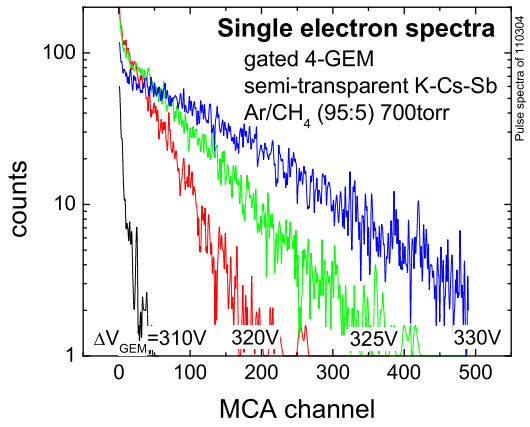

Fig. 8.12: Single-electron pulse-height spectra obtained for ΔV_{GEM}=310 V, 320 V, 325 V and 330 V, corresponding to respective gains of $7.5 \cdot 10^4$, $2.4 \cdot 10^5$, $4.6 \cdot 10^5$ and $9.3 \cdot 10^5$.

measurement methods is observed.

A gain close to 10^6 was reached in pulse mode with the bi-alkali photocathode and no ion feedback effects were observed even at the highest gains. This is by orders of magnitude the *highest* amplification factors ever reported for GPMs with visible-sensitive photocathodes.

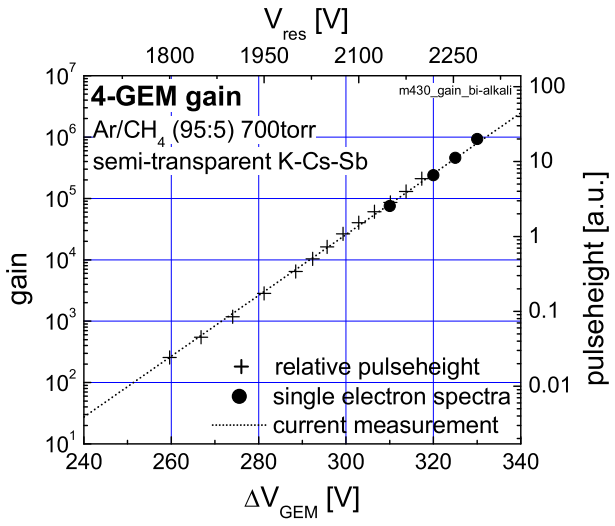

Fig. 8.13: The gain of the visible-sensitive 4-GEM GPM (Fig. 8.1) operated with a K–Cs–Sb photocathode in 700 torr Ar/CH_4 (95:5). The data points derived from the single electron spectra of Fig. 8.12 are indicated with full circles. The crosses are only relative measurements of the pulse height. The dashed line indicates a fit to the current measurement of Fig. 8.3 obtained with a CsI photocathode.

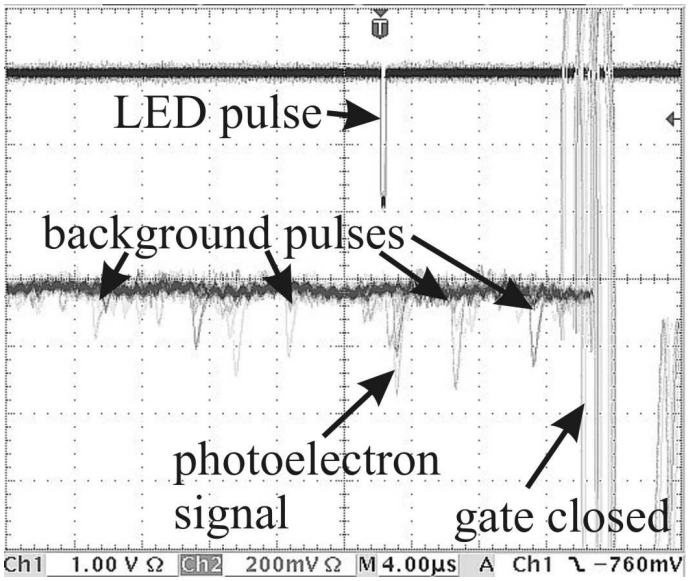

Fig. 8.14: Single-electron background pulses, most likely due to thermionic emission from the photocathode. The top channel shows the voltage pulse applied to the LED.

8.5 Thermionic emission

At gains above 10^5, sufficiently high for single electron detection, single-electron background was observed. These pulses appeared randomly at kHz rates during the open gate. In Fig. 8.14 these pulses can be clearly seen in an oscilloscope image obtained by sampling over ∼100 trigger signals from the UV-LED (top signal). The background pulses disappeared while applying a small reversed drift field (+10 V) on the photocathode. This implies that the single electron background originates from the photocathode. The most likely explanation of the observed background pulses is thermionic emission from the photocathode. As was discussed in Sec. 2.1 and shown in Fig. 2.2, K–Cs–Sb photocathodes exhibit a thermionic emission current of $\sim 10^{-17} A/cm^2$ at room temperature [6, 7]. For our 50 mm diameter K–Cs–Sb photocathodes, the resulting rate of emitted single photoelectrons responsible for the thermionic current would amount to ∼1 kHz; this is in good agreement with the observed background rate. In applications of single electron counting, the thermionic emission will contribute a temperature-depended background of single-electrons.

8.6 Summary and discussion on visible-sensitive gated GPMs

We designed, assembled and successfully operated for the first time a gaseous photomultiplier having a visible-light sensitive photocathode that operates reliably up to gains of $\sim 10^6$. For the experiment's duration of over 3 days, the K–Cs–Sb photocathode's QE did not deteriorate under gas multiplication. Its relatively low vacuum quantum efficiency of 8% at 400 nm was due to problems during the photocathode manufacturing process and is further reduced by photoelectron backscattering in gas to QE_{eff} ≈6%.

Stable single-photon sensitivity was reached in a gated mode. This achievement can be considered a breakthrough in the field of gaseous photomultipliers, paving the way towards

further developments; among them sealed, large-area visible-sensitive GPMs with position sensitivity.

Despite the success of our gated ion back-flow suppression, ion feedback remains the prime challenge in future developments of GPMs. In the experiment described above, the gate was triggered by the UV-LED pulse and opened only for a very short time ($\sim$120 μs) during which the photoelectron signal was recorded on the anode. It is not possible to use the photoelectron signal recorded on the anode to trigger the gate closing in the current system. The problem is due to the high ion-feedback probability $\gamma_+ \approx 4 \cdot 10^{-2}$ (see Sec. 5) and the large ion back-flow $\epsilon_{bf} \approx 0.1$ for an open gate (see Sec. 6). If a single-electron anode signal is not detected and does not trigger the closing of the gate, the corresponding avalanche ions will hit the photocathode and initiate secondary electron emission. When working at gains of 10^6, consequently $\sim 4 \cdot 10^{-2} \cdot 0.1 \cdot 10^6 = 4 \cdot 10^3$ secondary electrons will be generated on the photocathode, experiencing the same amplification of 10^6; the resulting avalanches will considerably exceed the Raether limit [68] of $10^7 - 10^8$ electrons, leading to a discharge [79, 151]. Lower gain operation would ease the problem somewhat, but if the avalanche ions are not stopped at the gate, even a single undetected event may result in detector breakdown. Thermionic emission events and some other sources of background will closes the gate, introducing often unacceptable dead-time. Therefore, currently the only possible operation is with an external trigger to open the gate for a short time, sufficient for photoelectron multiplication – as done above.

For most practical applications, ways must be found for reducing the ion back-flow down to levels that would permit DC operation. Some progress in this direction was discussed in Sec. 6.5; more recent work, beyond the scope of this thesis work, provided very encouraging results, namely ion back-flow values in the 10^{-3} range [145, 146]. The reduction of ion back-flow to the photocathode remains the most challenging task in the field of visible-sensitive GPMs.

9. IMAGING WITH THE MULTI-GEM

9.1 Introduction

GEM detectors are known to have very good imaging and tracking capabilities [101, 102, 103, 152], yielding a position resolution around 50 μm for charged particles and X-rays. As in GEM detectors the readout element is decoupled from the high voltage of the multiplying stages, one is essentially free in the choice of segmented anodes for two-dimensional position encoding. Pixelized anodes with small pads and individual read-out electronics offer the highest rate capability, even of simultaneous multiple events, and best multi-track resolution. But as a large number of readout electronics channels is required, it is often not the preferred method when large-area coverage is requested. A more economic approach is the use of two layers of perpendicular strips [102] or interconnected pads [110, 106], showing very good position resolution of 50 μm and better and at the same time drastically reducing the number of required electronic read-out channels. Recently, a 2D readout for GEM detectors having the individual strips of a crossed-strip-anode connected to a discrete delay-line was successfully tested, reducing the number of readout electronics channels to four [103, 96].

For evaluating the feasibility and properties of an imaging GPM, sensitive to single photons, we decided to incorporate a Wedge and Strip Anode (WSA) [153] as the readout stage of a multi-GEM detector. WSAs are commonly employed for the readout of Micro Channel Plates (MCPs) [154] suited for the use in sealed visible-sensitive GPMs: they are made of metal patterns on glass or ceramic and are very compact – with three readout channels only.

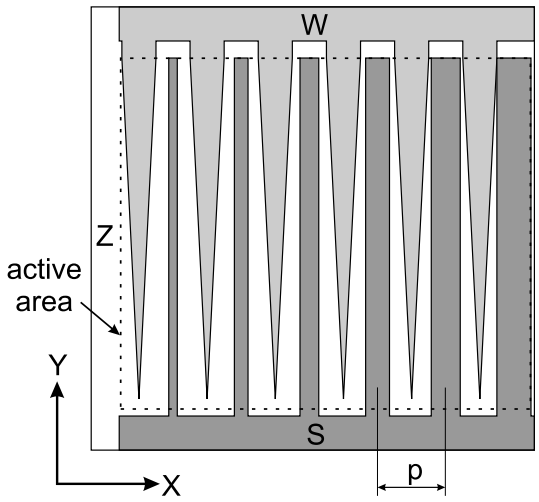

Fig. 9.1: The schematics of the WSA readout with the wedge (W), strip (S) and zigzag (Z) electrodes. The pitch (p) designates the distance between two strips, while the dashed line indicates the active area of the WSA.

The layout of a WSA is schematically illustrated in Fig. 9.1a. The WSA is patterned with wedge (W), strip (S) and zigzag (Z) electrodes, separated by a thin insulating gap. The width of the strips increases linearly along one direction of the anode (defined as the *X-coordinate*), while the width of the wedge increases linearly in the orthogonal direction (*Y-coordinate*). In such an arrangement the fractional area coverage of the wedge and the strip electrodes encodes the position of a collected charge cloud. From the charge fraction recorded on each of the three electrodes the centroid position of the charge cloud can be obtained using the following formulae:

$$X = c_1 \frac{Q_S}{Q_S + Q_W + Q_W} \tag{9.1}$$

and

$$Y = c_2 \frac{Q_W}{Q_S + Q_W + Q_Z} \tag{9.2}$$

where Q_S, Q_W and Q_Z is the charge measured on the strip, wedge and zigzag electrodes respectively; c_1 and c_2 are calibration factors.

Eqs. 9.1 and 9.2 are only valid if the following requirements are fulfilled:

- The spread of the avalanche charge on the anode has to be larger than the pitch p. Otherwise an *interpolation* over the discrete anode pattern is not ensured, resulting in a non-linear position encoding known as *modulation* [154, 155].
- The charge cloud has to be confined within the active area of the WSA. If a fraction of the avalanche charge is collected outside of the active area, the proportionality of collected charge and position no longer holds, leading to another form of distortion, the *S distortion* [153, 155].

A more detailed discussion on WSAs, image distortions and possible ways to correct for them can be found in [153].

For typical WSA dimensions and pitches ($\sim$1 mm) these conditions are not easily satisfied when using cascaded GEM detectors. The charge spread due to electron diffusion in the gas is typically a few 100 μm FWHM only. It has to be deliberately enlarged by using gas mixtures having high transversal diffusion coefficients and by using detector geometries with long electron drift distances [96]. This of course will result in deterioration of the timing properties of the detector.

Alternatively, a thin resistive layer for charge collection can be placed above the structured readout element to achieve the required charge spread on the WSA [156]. The avalanche charge arriving from the electron multiplier is collected on the resistive layer and induces a signal on the anode below. If the layer thickness and resistance are optimized, the capacitive-coupled signal can be measured on the anode without losses [157]. The spatial charge distribution on the anode is similar to the distance between the resistive layer and the readout structure [157] and is therefore easily adapted to the experimental requirements.

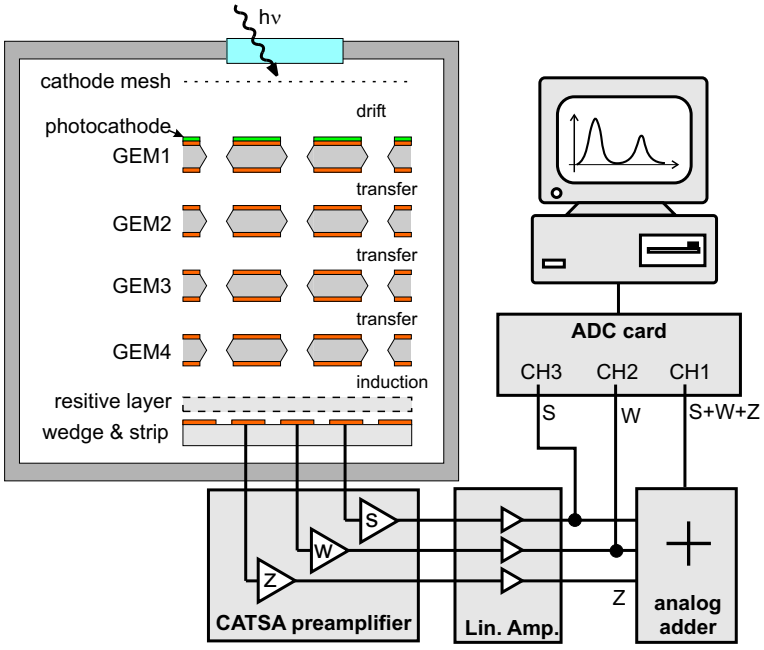

Fig. 9.2: Experimental setup for position measurements with a wedge and strip anode. A GEM having one face covered with a CsI photocathode was added on top for UV-photon imaging. A restive layer could be placed below the last GEM for broadening the charge spread on the WSA.

Furthermore, the decoupling of the segmented readout structure from the charge collection element, allows to conceive detectors having intricate readout schemes placed *outside* the detector volume [156]. Such an approach would considerably relax the requirements on electronic feedthroughs and cleanliness of the readout structure. On the other hand, the use of resistive layers implies reduced rate capabilities of the detector due to the slower charge collection from the layer.

We tested the imaging capabilities of a multi-GEM detector employing a WSA readout with and without resistive layer. The primary charges were either induced by X-rays converting in the drift region above the first GEM in a cascade or by single UV-photons on a reflective photocathode deposited on the topmost GEM.

9.2 Experimental Setup and Methodology

The test detector consisted of 3 or 4 standard GEMs mounted on G10 frames for X-ray and single-photon imaging, respectively. In the latter case, the top GEM was coated with a reflective CsI photocathode for photoconversion, as described in Sec. 4. The avalanche charge extracted from the last GEM was either collected directly on the WSA element or on a resistive layer element above the WSA. The drift and transfer gaps were 3.2 mm and 1.6 mm respectively, while the induction gap was varied between the measurements; its value is provided below together with the respective results. The experimental setup is shown schematically in Fig. 9.2.

For our studies we used a WSA readout that was fabricated with a standard photo-lithographic

printed circuit technology on a 1.6 mm thick G10 frame. It had an active area of 20×20 mm^2 with a pitch of p=1.5 mm (see Fig. 9.1). Surrounding the active area was a grounded electrode, preventing up-charging. The resistive layer was chosen from several samples of Ge-film deposited by thermal vacuum deposition of Ge from W-boats. Layers with thickness ranging from 30–160 nm on a 1.6 mm thick G10 substrate were tested, having respective surface resistivities between 370–30 MΩ/□. In preliminary tests, the 160 nm Ge layer with 30 Ω/□ surface resistivity yielded full signal transmission to the WSA and was subsequently employed in the detector [106]. A spacer fixed the distance between resistive layer and WSA to 1.9 mm, ensuring a sufficiently broad signal induction (∼2 mm) on the WSA.

The detector was mounted in a testing vessel and operated under continuous flow of atmospheric Ar/CH_4 (95:5), known to generate a rather broad charge distribution on the anode due to its high diffusion [103]. The detector electrodes were powered by a resistor network, designed to yield electric fields of 1 kV/cm in the drift region, 2 kV/cm in the transfer region and 3 kV/cm in the induction region for ΔV_{GEM}=300 V[1]. In the case of single-photon imaging, the cathode mesh and the photocathode on the topmost GEM electrode were interconnected ($E_{drift} = 0$) and a higher induction field E_{ind}=4 kV/cm was used.

All three WSA electrodes were connected to identical electronic readout circuits, each consisting of a charge sensitive pre-amplifier[2] and linear amplifier[3], as indicated in Fig. 9.2. The amplified signals were simultaneously digitized in a PC-born ADC[4]. The sum of all three WSA signals was obtained in an analog adder[5] and provided the trigger of the ADC. The digitized waveforms were analyzed by a dedicated software[6]; it allowed for a flexible data manipulation, pulse-height analysis and calculation of the centroid position of the signal recorded on the WSA according to Eqs. 9.1 and 9.2. The processed data could be either stored on hard disc for further analysis or displayed online on the PC screen.

For X-ray imaging, the detector was illuminated with a collimated ^{55}Fe source emitting 5.9 keV photons. To minimize parallax effects, the source was positioned ∼ 30 cm away from the detector. For single-photoelectron imaging experiments a UV-transparent quartz window replaced the mylar foil of the X-rays detection setup and a collimated Hg(Ar)-lamp was used for detector illumination. The light intensity could be controlled by optical absorbers, down to the level of single photons.

Different metallic masks with slits of varying width were placed in front of the detector's window. The obtained images of the slits are a convolution of the slit geometry and the position resolution of the detector. From these images the position resolution of the detector is extracted according to a method described in [158].

As the position resolution is calculated from the charge sharing between the three electrodes of the WSA, it is expected to be dependent on the total charge collected on the anode per event. For X-rays, the total charge is the product of the gain and the number of primary

[1] The resistor values were 10 MΩ for the drift region and the GEM potentials and 13.3 MΩ for the transfer region. The resistor defining the induction field was either 70, 33 or 11 MΩ, depending on the length of the induction gap.
[2] CATSA, Roentdek GmbH, Germany
[3] Model 570, ORTEC
[4] 12-bit, 4-input simultaneous sampling ADC card, PCI-6115 ADC, National Instruments
[5] model 433A, ORTEC
[6] programmed in LAB-VIEW, National Instruments

electrons; for 5.9 keV X-rays in atmospheric Ar/CH_4 (95:5) $\sim$230 electrons are generated in the drift gap per absorbed photons. In contrast, for single-electron detection, the total charge collected on the anode varies considerably from event to event due to the Polya-distributed amplification process.

9.3 Results

9.3.1 X-ray imaging without resistive layer

At first, we evaluated the X-ray imaging capabilities of the WSA and the 3-GEM detector arrangement with a collimated ^{55}Fe source. The avalanche charge extracted from the last GEM was collected directly on the WSA electrodes.

Even when allowing for a large induction gap of 5.5 mm and a relatively weak induction field of 3 kV/cm, a charge cloud width of $\sim$1.5 mm was obtained on the WSA. This was approximately equal to the WSA pitch and consequently an image modulation was observed. The image of Fig. 9.3 obtained by homogeneously illuminating the 15 mm diameter entrance window with X-rays and working with a detector gain of $2 \cdot 10^4$ (total charge $\sim 4 \cdot 10^6$), shows strong modulation in the X-coordinate, along the direction of the strips. No modulation along the Y-axis was observed, as the width of the wedge electrode changes uniformly in the Y-direction. The distance between the *modulation lines* of the image corresponds roughly to the WSA pitch of 1.6 mm. Despite the modulation in X-direction, we evaluated the position resolution along the Y-axis by illuminating the detector through a mask having a 250 μm wide slit oriented parallel to the X-direction. Fig. 9.4 shows the image projection onto the Y-axis of an image obtained at a gas gain of $2 \cdot 10^4$. Deconvolution of the image with the slit width yielded a position resolution of $\sim$ 170 μm FWHM.

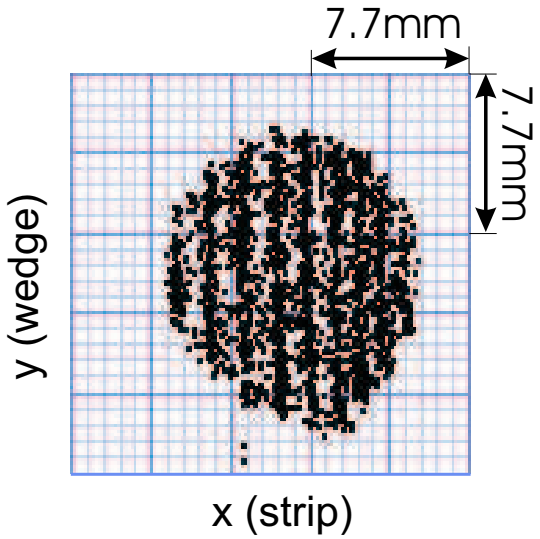

Fig. 9.3: A 2D X-ray image recorded with a 3-GEM detector at a gain of $2 \cdot 10^4$ in atmospheric Ar/CH_4 (95:5). The insufficient charge spread on the WSA caused image modulations. These are mainly along the X-direction (*strip-direction*) for a homogeneously illuminated detector.

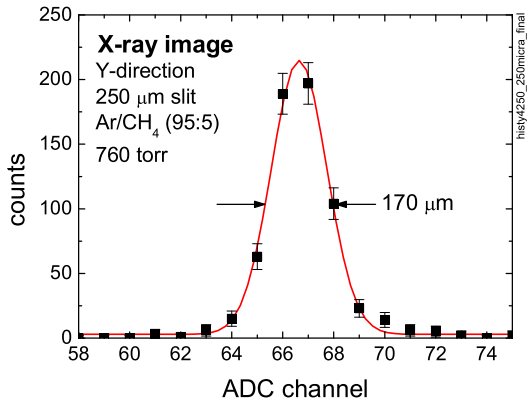

Fig. 9.4: Projection of the X-ray image of a 250 μm wide slit onto the Y-axis. The image was obtained with a 3-GEM detector at a gain of $2 \cdot 10^4$.

To subsequently avoid image modulations, the charge width on the anode had to be increased. This could have been achieved either by working with gas mixtures having higher transversal diffusion or by using larger induction gaps. Both approaches have their drawbacks: The choice of the gas mixture is generally dictated by other considerations like electron backscattering in gas and detector gain, while enlarging the induction gap and keeping the field strength constant would require inconveniently high detector potentials, resulting in possible discharges on the feedthroughs and to the body of the detector package.

Instead, spreading the charge through a resistive layer can solve the problem of modulation if the capacitively-induced signal on the anode is wider than the WSA pitch.

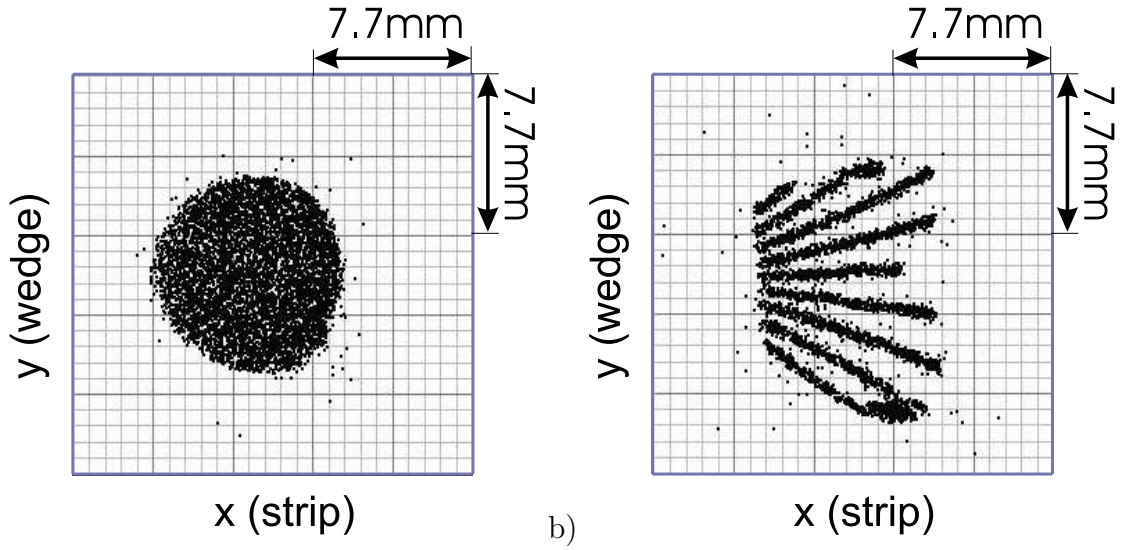

Fig. 9.5: a) Image of the homogeneously illuminated active area of the multi-GEM detector with resistive layer in front of the WSA readout. No image modulation is observed. b) X-ray image of a mask with 400 μm wide slits, 250 μm separated at their closest point.

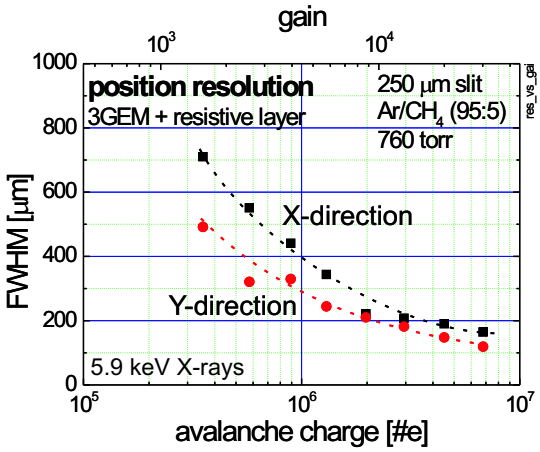

Fig. 9.6: Position resolution of a 3-GEM detector with WSA and resistive layer for charge collection measured with 5.9 keV X-rays. The resolution (full-width-half-maximum) of the X- (squares) and Y-coordinates (circles) is plotted as a function of the total number of electrons per avalanche (bottom X-axis) and of the detector gain (top X-axis).

9.3.2 X-ray imaging with resistive layer

The X-ray imaging experiment was repeated with a reduced induction gap of 2.5 mm and a resistive layer placed 1.9 mm above the WSA. The avalanche charge collected on the resistive layer induced a sufficiently broad charge on the WSA to prevent modulation effects. Fig. 9.5a shows the image of the homogeneously illuminated active area of the detector; no image modulations in either direction were observed. A metal mask with rays of slits, 400 μm wide and having a separation of 250 μm at their closest points, was placed in front of the detector's entrance window. The image of Fig. 9.5b was obtained from this mask at a gas gain of $2{\cdot}10^4$. The individual slits are clearly resolved, even at their closest point.

The position resolution of the detector for X-rays as a function of the detector gain was measured for both coordinates using the single-slit mask of 250 μm oriented in parallel to the respective direction. The results, plotted in Fig. 9.6, show a strong influence of the gain, or the total avalanche charge, on the position resolution of the detector along both coordinates. The position resolution improves considerably for high gains, corresponding to a higher number of electrons per avalanche, and thus an improved signal-to-noise ratio on the individual WSA electrodes. Above a gain of 10^4, the image resolution improves only slowly, reaching 160μm and 120μm FWHM for the X- and the Y-coordinates respectively at a gain of $3.4 \cdot 10^4$. Due to the *discrete* strip pattern, the resolution in X-direction is always slightly worse than the resolution in Y-direction. From Fig. 9.6 it is clear, that even an avalanche of $3{\cdot}10^5$ electrons yields a sub-millimeter position resolution.

9.3.3 Single-photoelectrons imaging

For single-photoelectron imaging the detector and the experimental setup was modified: A fourth GEM was added on top of the three preceding ones, serving also as the substrate for a

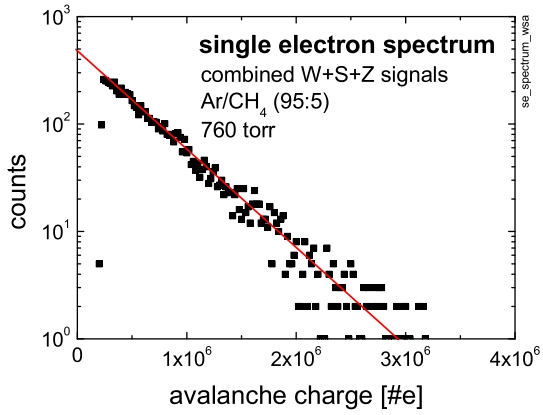

Fig. 9.7: Single-electron spectrum obtained in the 4-GEM GPM, by adding the S,W and Z signals of the WSA (Fig. 9.1) at a detector gain of 10^6.

2500 Å thick CsI photocathode, 15 mm in diameter. The induction gap between GEM4 and the resistive layer was reduced to 0.6 mm to reduce the potential difference in the induction gap. The Ar(Hg) lamp was placed $\sim$ 30 cm away from the entrance window and absorbers reduced the light intensity to achieve a homogeneous illumination with single UV photons.

The detector was operated at gains up to $1.6 \cdot 10^6$, more than sufficient for the detection of single photoelectrons. Single-electron spectra were recorded by adding the digitized signals of the three WSA electrodes. As an example, Fig. 9.7 shows a typical exponential-shaped single-electron spectrum obtained at a detector gain of 10^6.

Resulting from large fluctuations in the total avalanche charge per event, we found a strong dependence of the measured position resolution on the threshold used to discriminate between signal and noise. A higher threshold ensured a higher average avalanche charge and therefore improved the measured position resolution (see Fig. 9.6). Using a rather high threshold of 10^6 electrons per avalanche, a very good position resolution for single photoelectrons of 300μm and 200μm FWHM was measured for the X- and Y-coordinates respectively, but at the cost of a rather small detection efficiency for single electrons. A threshold below $\sim 5 \cdot 10^5$ was found to yield images of very poor quality, and our method of measuring the position resolution by evaluating the image of a single slit mask could no longer be applied in these cases. Figs. 9.8 and 9.9 show examples of single-photon images obtained at a gain of $1.6 \cdot 10^6$ and with a threshold of 10^6. The use of a resistive layer ensured that the signals induced on the WSA are sufficiently broad to avoid image modulations.

The image of Fig. 9.9a was obtained illuminating the mask of Fig. 9.9b, having letters of 2 mm length and 120 μm width. The image distortions towards the bottom of the image are attributed to *s-distortions* (see Sec. 9.1) at the border of the active area of the WSA readout.

9.4 Discussion and conclusions

The readout of multi-GEM detector coupled to a wedge and strip anode showed encouraging results for both X-ray and single photoelectron imaging. A resistive layer above the WSA readout was successfully employed in order to induce sufficiently broad charge signals on the anode and to avoid image modulations. Resistive layers are a very attractive choice as charge collecting electrodes in sealed imaging visible-sensitive GPMs. The dielectric substrate of the resistive layer could function as part of the detector enclosure and HV insulator for sealed visible-sensitive GPMs. In such a configuration, the readout can be placed outside of the detector volume, allowing for easily accessible, non-vacuum compatible 2D readout schemes and making the electrical connections much simpler. In addition, the use of a resistive layer allows to tailor the required charge spread on the readout, without limiting the choice of the detector geometry, gas mixture and electric fields.

In a 3-GEM detector with WSA and resistive layer, we measured a position resolution for 5.9 keV X-rays of 160 μm and 120 μm FWHM for the X- and the Y-directions, respectively, at a gain of 3.4×10^4. These results are in good agreement with previously published imaging properties of GEM detectors, despite the differences in readout schemes, detector geometries and operation conditions [101, 102, 103].

In a 4-GEM GPM with reflective photocathode and a WSA readout, we demonstrated for the first time the feasibility of a single-photon imaging GPM with sub-millimeter precision. Unfortunately, in order to reach this resolution, we were compelled to work at conditions with rather low single-photoelectron detection efficiency, namely only events with a total avalanche charge exceeding 10^6 were recorded. These observations are confirmed by others, using WSA readouts in combination with MCPs [153, 159]: they report charge clouds of few times 10^6 and above were required for best imaging performance. In GEM-GPMs these requirements cannot be fulfilled for single photoelectrons, due to the gain fluctuations and the limited total gain of the detector (typically 10^6). While a careful design of the WSA, minimizing its capacitance and employing better, low noise charge sensitive pre-amplifiers [160] could improve the situation to some extent, WSA readouts are certainly not suited for conceiving imaging GPMs with high single-photon detection efficiency. Other readout schemes, sharing the charge between fewer electrodes, like single pads, individual strips on two layers [102] or a delay line readout [103] might provide better results. Yet, in most applications, the imaging of *multi-photon* events is demanded, and the total avalanche charge required for a WSA readout is more easily achieved in these cases.

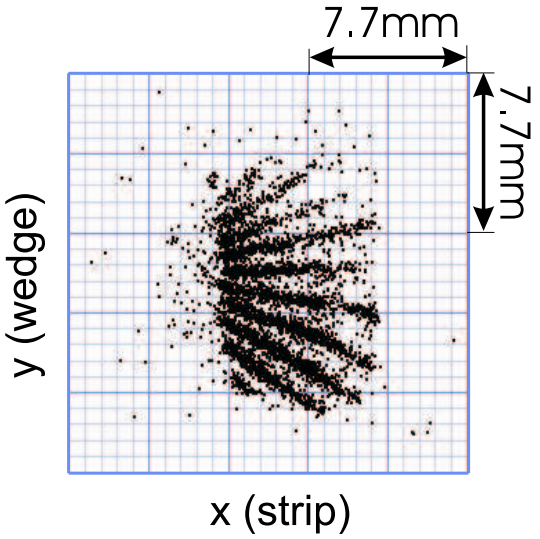

Fig. 9.8: Single-photon image of a mask with 400 μm wide slits, 250 μm separated at their closest point.

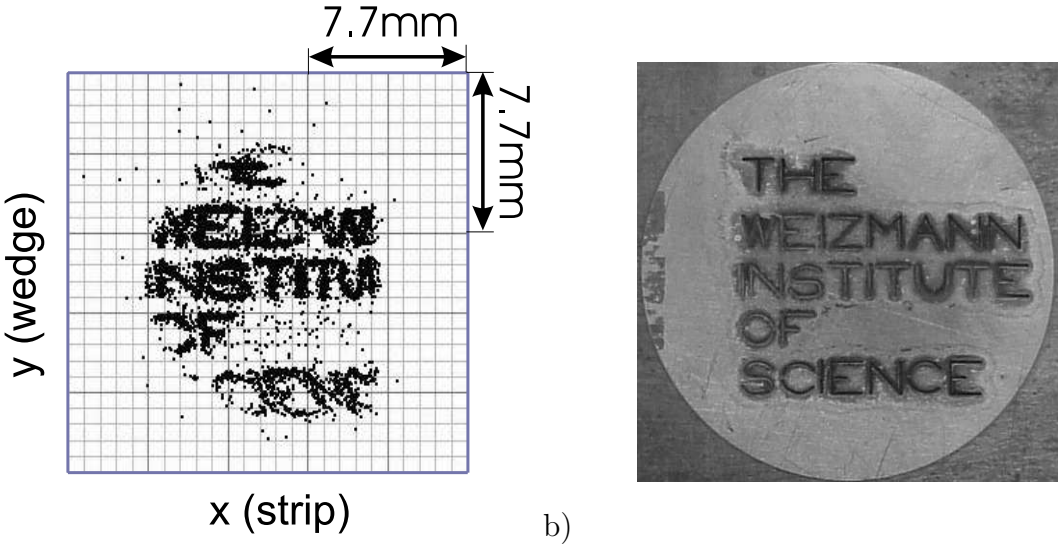

a) b)

Fig. 9.9: a) The image resulting from illuminating a b) metal mask with the institute's name with single UV-photons. The letters etched in the mask have 2 mm height and 0.12 mm width.

10. CONCLUSION AND SUGGESTIONS FOR FURTHER WORK

In this thesis work we aimed at developing novel large-area *gaseous photomultipliers* (GPMs) for the UV and the visible spectral range; they combine thin-film photocathodes coupled to cascaded Gas Electron Multipliers (GEM), operated at atmospheric pressure. These novel fast photon imaging detectors, with single-photon sensitivity, have the potential to compete with vacuum photon detectors in many fields of application, such as in imaging Cherenkov light in particle physics and astrophysics, recording scintillation information in particle physics and medical imaging, etc. They may compete with solid state detectors in size and in single-photon sensitivity.

We have brought in this work the UV-sensitive GPMs to an operational stage; they have become a **mature tool**, already employed in physics experiments. This work proves for the first time, that such sealed detectors with visible-sensitive bi-alkali photocathodes can be successfully operated in an ion-gated mode, at gains suitable for single-photon imaging. This achievement can be considered a **major breakthrough** in the field of photon detectors.

For reasons of convenience, the detailed discussion of the research results is provided for each topic separately within the thesis; only a more general summary and discussion are provided here.

Present-day UV-sensitive GPMs, employed for single-photon imaging of Cherenkov light, have large-area (square meters) CsI UV-sensitive photocathodes and wire-chamber electron multipliers. In this "open geometry" the avalanche develops at the wire vicinity, at a short distance from the photocathode where all avalanche ions are collected. This results in significant photon- and ion-mediated secondary effects, limiting the detector's gain and its single-photon detection efficiency; they also causing photocathode damage. The ion-induced secondary electron emission effects, particularly important in visible-sensitive photocathodes, prevent the application of wire-chamber GPMs in the visible spectral range. We have therefore suggested developing photon imaging detectors comprising electron multipliers of a "closed geometry"; we have chosen cascaded "hole-multipliers", in which the avalanche that develops in successive GEM multiplication stages is confined within the holes. In this configuration the photocathode is screened from avalanche-induced photons and the ion back-flow to the photocathode could be 10-fold reduced compared to that in wire chambers, as demonstrated in this work.

In this work we have investigated the mechanism of operation and physical properties of cascaded-GEM GPMs. We studied photoelectron extraction, transport and multiplication as well as the ion back-flow to the photocathode; both configurations were investigated: detectors with semi-transparent photocathodes (*semi-transparent-GPMs*) and, for the first time, detectors with reflective photocathodes deposited on the top surface of the first GEM in the cascade (*reflective-GPMs*).

In addition to the properties mentioned above, our studies revealed that cascaded-GEM

GPMs exhibit many other advantageous features: as the multiplication occurs over tens of micrometers distances, they have a fast avalanche build-up and therefore nanosecond time response for single photons; they permit reaching multiplication factors exceeding 10^6 in a variety of gases, including noble-gas mixtures and CF4, and therefore high sensitivity to single photons; they are capable of operating at very high photon flux. The imaging capabilities of multi-GEM detectors were investigated with Wedge & Strip Anode (WSA) readout elements, as function of different detector's parameters; single-photon resolutions of 100-200 micrometers (RMS) were reached.

Our preferable detector configuration is the "reflective-GPM"; the reflective photocathodes exhibit higher QE values, are easier to manufacture and more robust compared to semi-transparent ones. The properties and operation characteristics of these GPMs were studied in detail and conditions were found in which all emitted photoelectrons are collected into the detector's multiplying stages and subsequently recorded on the readout anode. Furthermore, this GPM design permits to considerably reduce the sensitivity to ionizing radiation background by operating with a slightly reversed drift field above the photocathode surface, while retaining a high sensitivity to photons. Based on our results, such GPMs are currently under development by other colleagues (Weizmann Institute/BNL/SUNY) for a Hadron-blind Cherenkov detector of the PHENIX relativistic heavy-ion experiment at RHIC (BNL); similar detectors are investigated by Sauli et al. at CERN for Cherenkov Ring Imaging.

A more challenging task has been the extension of the spectral sensitivity of GPMs towards the visible spectral range, where most applications exist, by employing photocathodes with lower photoemission thresholds. Such photocathodes are generally restricted to operation in ultra high vacuum environment; e.g. bi-alkali photocathodes decay promptly upon exposure to minute amounts of oxygen or moisture and can only be operated in sealed conditions with electron multipliers made of ultra-high vacuum compatible materials. Furthermore, their low electron emission threshold makes them very prone to ion feedback. A major part of the thesis work was devoted to the investigations of methods and concepts for producing, investigating and sealing in pure gases GPMs with bi-alkali photocathodes. Despite our success in reducing the avalanche ion back-flow to the photocathode in cascaded GEMs by approximately an order of magnitude, ion feedback was found to severely limit the operation of GPMs with K-Cs-Sb photocathodes; the multiplication factors in such detectors were limited at best to 10^3, which is far below the values needed for single-photon detection. The probability of ion-induced secondary electron emission on K-Cs-Sb photocathodes was studied for in several gas mixtures. The experiments revealed that the ion-feedback probability depends only on the gas component with the lowest ionization potential; e.g. even a small fraction CH4 gas in Argon was found to lower it to a few percent. Other gases may therefore further reduce these effects; however, the ion feedback must be reduced by orders of magnitude, down to levels of 10^{-4}, to permit a stable DC-mode operation of visible-sensitive GPMs. The introduction of an ion-gating electrode, pulsed in synchronism with the transit of the avalanche ions, allowed to reduce the ion back-flow by more than a factor of 10^4. This mode of operation permitted to operate the cascaded GEM multiplier at a gain of $\sim 10^6$ with a K-Cs-Sb photocathode. **This is the first time a visible-sensitive GPM with single-photon sensitivity was realized; this result is an important milestone in the development of gaseous photomultipliers.**

The gating method of ion back-flow reduction introduces a relatively large dead time, requires an external trigger signal and is often cumbersome to use. A major task for future research

will therefore be to conceive electron multipliers which permit a more efficient avalanche-ion blocking. Detectors combining cascaded Microhole & Strip Plates (MHSP) and GEMs are a very attractive approach and are currently under investigation within a cooperation between the Radiation Detection Physics Group of the Weizmann Institute and the Physics Department at the University of Coimbra. Very recent results indicate upon ion back-flow values as low as 10^{-3}, namely two orders of magnitude lower than in cascaded-GEM GPMs [161]. This should already allow operating GPMs with visible-sensitive photocathodes at gains approaching 10^5 in a DC mode; better methods are foreseen. These recent studies indicate that the aging of bi-alkali photocathodes under gas multiplication are similar to that of thin alkali-halide UV photocathodes. The lifetime of visible-sensitive GPMs operated at a gain of 10^5, with a photon flux of 1 kHz/mm^2, is estimated to be >10 years with the recently demonstrated ion back-flow of 10^{-3}.

We are confident that visible-sensitive GPMs are at a reach. The extension of the small-area prototype to large-area devices can be considered a mainly technological challenge, especially in respect to large-area photocathode production and detector sealing, for which technologies exist. Multipliers of other ultra-high vacuum compatible materials are under investigations at the Weizmann Institute group; they should provide a more appropriate solution for sealed GPMs. Other, simpler Thick GEM-like (THGEM) multipliers should provide a simple solution for large-area detectors [88, 89].

APPENDIX

A. ELECTRON MULTIPLIER PREPARATION FOR VISIBLE-SENSITIVE GPMS

We prepared electron multipliers for coupling to K–Cs–Sb photocathodes in two types of packages. The GPMs were operated in a sealed mode in type A packages; more advanced GPMs were prepared for type B packages, which were not yet complete and could not be sealed. Their multipliers were operated in an unsealed mode.

A.1 GPM preparation in type A detector package

Fig. A.1 shows photographs of packages of type A; they have a height of 25 mm and a diameter of 68 mm. The package body is made of Kovar-metal, having the same thermal expansion coefficient as the photocathode glass substrate. For electrical contact, 16 Kovar pins of 1 mm diameter are glass-sealed into the package base. The package body and the pins are electro-plated with 10 μm electroless Ni alloy (92–95% Ni, 8–5%P). A 1 mm deep and 2 mm wide groove around the circumference of the package opening allows to place In/Bi solder for sealing with a photocathode, as described in App. B. Before their first use, new packages are cleaned in an ultrasonic bath in 20% HCl for 2 min, followed by DECONEX 15 PF (10% in double-distilled water), double-distilled water and finally absolute ethanol (30 min each); they are blown dry with nitrogen and stored under vacuum. Already used packages are cleaned in ethyl alcohol for 30 min in an ultrasonic bath.

The detector elements are mounted inside the package by stacking them on the feedthrough

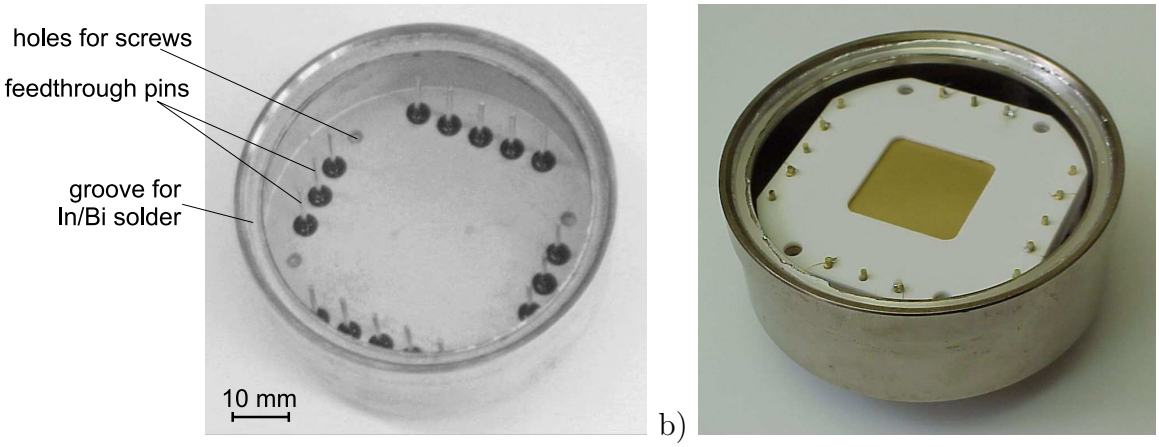

Fig. A.1: Photographs of a type A detector package: a) empty and b) with a multi-GEM electron multiplier assembled inside. The top-most ceramic frame to cover the feedthrough pins and the solderings on top is not shown.

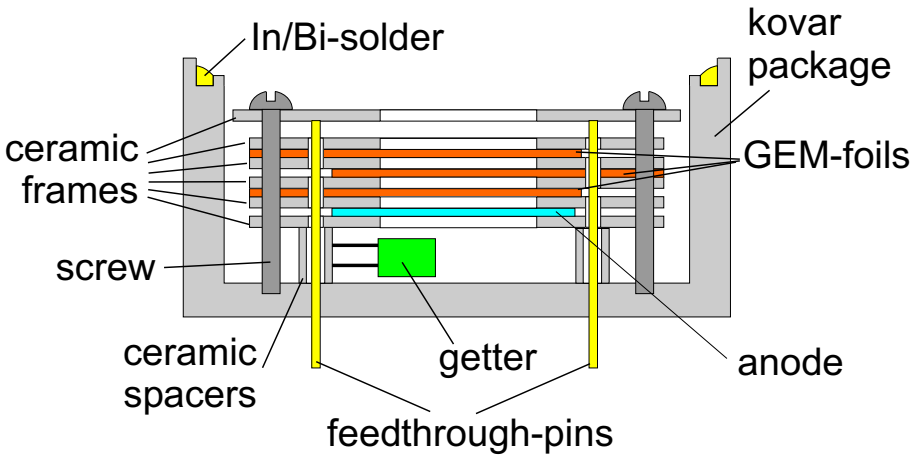

Fig. A.2: Arrangement of the detector elements inside the type A detector package.

pins; 1 mm thick ceramic spacer frames separate consecutive elements. Their 20×20 mm^2 central opening defines the active area of the GPM. Before their use, the ceramic frames are cleaned in DECONEX 15 PF (10% in double-distilled water) in an ultrasonic bath (for 6 hours) and baked in air for 6 hours at 700°C. The readout anode is made of a 30×30 mm^2, 0.5 mm thick pieces of stainless steel; it is carefully polished to avoid high voltage discharges from sharp edges when operated in gas. A 70 μm in diameter Au-coated Be/Cu wire is soldered to the anode with pure Sn and HCl-based flux. The anode is thoroughly cleaned in petroleum ether, followed by pure acetone and ethanol in an ultrasonic bath for 10 min each prior to mounting. The same wire is soldered to the contact pads of the GEM-foils with pure Sn and minimal amounts of $ZnCl_2$-based flux.

As schematically shown in Fig. A.2, the detector elements are sandwiched between the 1 mm thick ceramic frames and fixed to the package body by two stainless steel screws. The contact wires from the individual elements are soldered to the top of the feedthrough pins with pure Sn; excess wire is cut behind the solder point. The photograph of Fig. A.1b shows a package with a multi-GEM electron multiplier prepared inside. An additional ceramic frame is placed on top of the assembly and fixed to the package body by another pair of stainless steel screws; it covers the top of the feedthrough pins and the solder points, preventing high voltage discharges to a photocathode substrate sealed to the package. The distance between the first GEM and a photocathode substrate is approximately 5.5 mm. For K–Cs–Sb photocathode sealing, a low temperature activated getter[1] is mounted in the bottom of the package before assembly of the detector elements (Fig. A.2). It is activated just prior to the sealing process, as described in App. B.

Occasional HV breakdowns between the feedthrough pins and the package body limited detector voltages to ∼1500 V, severely restricting the operation of sealed GPMs. Furthermore, the small depth of the type A detector packages did not permit to accommodate additional detector elements like a structured readout anode or an ion-gate. Also the assembly of the detector elements inside the package without access from the sides and soldering the thin contact wires to the top of feedthrough pins were very intricate and delicate tasks. These difficulties necessitated the design of an improved detector package.

[1] Type 172, SAES Getters, Italy

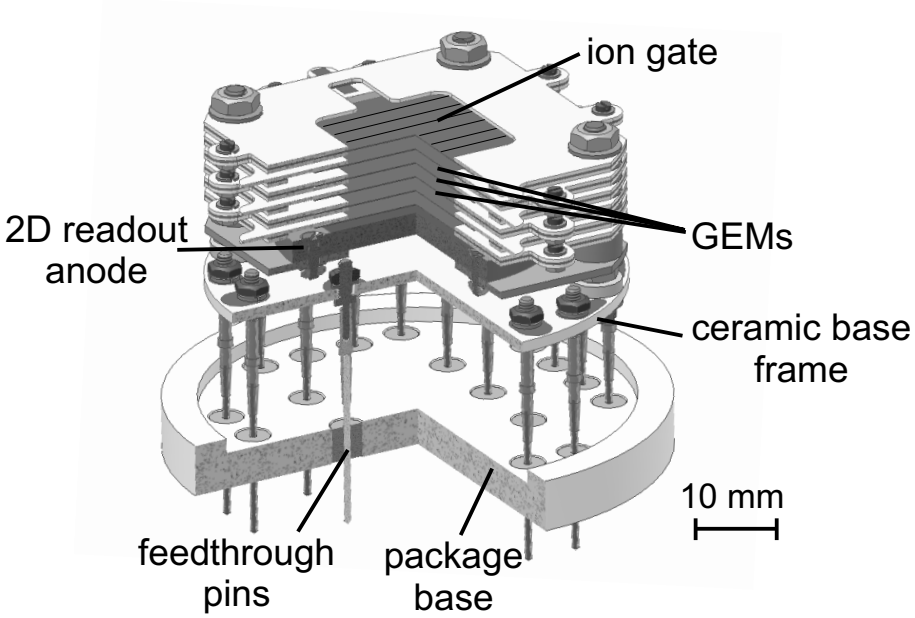

Fig. A.3: Schematic illustration of an electron multiplier assembled on the base plate of the "new" detector package.

A.2 GPM preparation in the type B detector package

The detector packages of type B design feature the same 68 mm diameter Kovar body, but have an increased height of 60 mm. To prevent HV discharges to the feedthrough pins, the package base is made from alumina, "brazed" to the Kovar body. 22 feedthrough pins are glass-sealed to the package base: 16 at the circumference for contacting the GEM and ion-gate electrodes and 6 in the center for getter and readout anode contacts. Unfortunately, at the time of writing the thesis, only the inner elements and the package base were available for experiments; but not the Kovar body. Therefore the type B packages could not be sealed to photocathode substrates. The detector elements were nevertheless assembled and successfully operated in an unsealed-mode inside the vacuum chamber of the K–Cs–Sb setup (see Sec. 8).

In the new modular electron multiplier assembly the detector elements are mounted on a base ceramic frame as shown in Fig. A.3. The base frame with the electron multiplier assembly is simply "plugged" onto the feedthrough pins of the package base. As an additional benefit, the detector functionality can be tested independently from the package body; this is of an advantage when package sealing is foreseen and the exposure of the In/Bi solder to ambient air has to be minimized (see App. B).

The GEMs and the anode are prepared identically as for electron multipliers assembled in package type A, using Au-coated Be/Cu wires soldered with pure Sn to the elements. The ion-gate is prepared on a dedicated ceramic frame, having Pd/Ag solder pads. The Pd/Ag pads are pre-wetted with pure Sn solder by heating the frame to 200°C and placing chips of Sn with a soldering iron. A set of 1 mm spaced parallel wires is stretched on a large 100×100 mm^2 frame; we used 50 μm diameter tungsten wires with a 2 μm thick Ni coating for better soldering. The large wire frame is placed on the ceramic frame and

aligned to the solder pads. To assist the soldering of the wires to the Pd/Ag pads, the ceramic frame is heated to ∼180°C from below with a hot plate. After the frame is cooled to room temperature, the wires are cut behind the soldering points. Additionally, two 70 μm in diameter Au-coated Be/Cu wires are soldered to the ion-gate frame for contacting. The photograph of such an ion gate on a ceramic frame is shown in Fig. A.4a.

The ceramic base frame, shown in Fig. A.4b, has 22 Pd/Ag pads with a central hole, one pad for each feedthrough pin. The base frame is heated to 200°C on a hot plate and the pads that will contact detector elements are pre-wetted with pure Sn. Subsequently, a small connector is placed in the pad holes and fastened from the backside with a washer and nut. When plugged to the package base plate, theses connectors will establish electrical contact to the detector elements in the assembled electron multiplier.

The detector elements are stacked on four M3 screws in the corners of the base frame; metal spacer tubes placed on the screws below the first ceramic frame (Fig. A.5a) allow to adjust the height of the electron multiplier. On the first ceramic frame the anode is placed and covered by a 1 mm thick ceramic frame (Fig. A.5b). Alternating, 4 GEM foils and ceramic frames are stacked on the screws (Fig. A.5c) followed by the ion-gate element. The assembly is finished by fastening the frames on the screws with nuts. As the last step in the electron multiplier preparation, the contact wires of the individual detector elements are soldered to their respective contact pads on the ceramic base frame. The soldering is assisted by locally heating the ceramic base frame with hot air (∼200°C) from a hot gun. Subsequently, all wires are carefully cut behind the soldering points. Fig. A.5d shows a photograph of the finished electron multiplier assembly, it can now be placed inside the sealing chamber of the bi-alkali setup.

a) 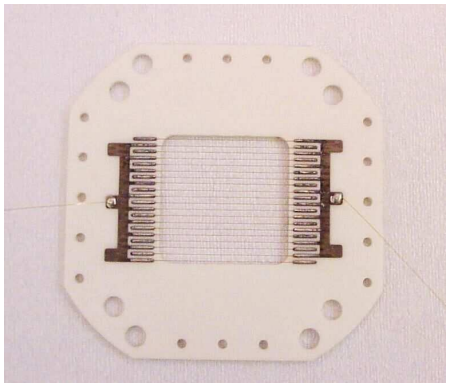 b) 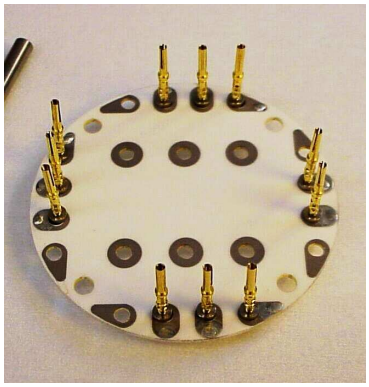

Fig. A.4: a) An ion gate prepared on a ceramic frame. b) The ceramic base frame has its Pd/Ag pads pre-wetted with pure Sn solder and connector plugs fastened.

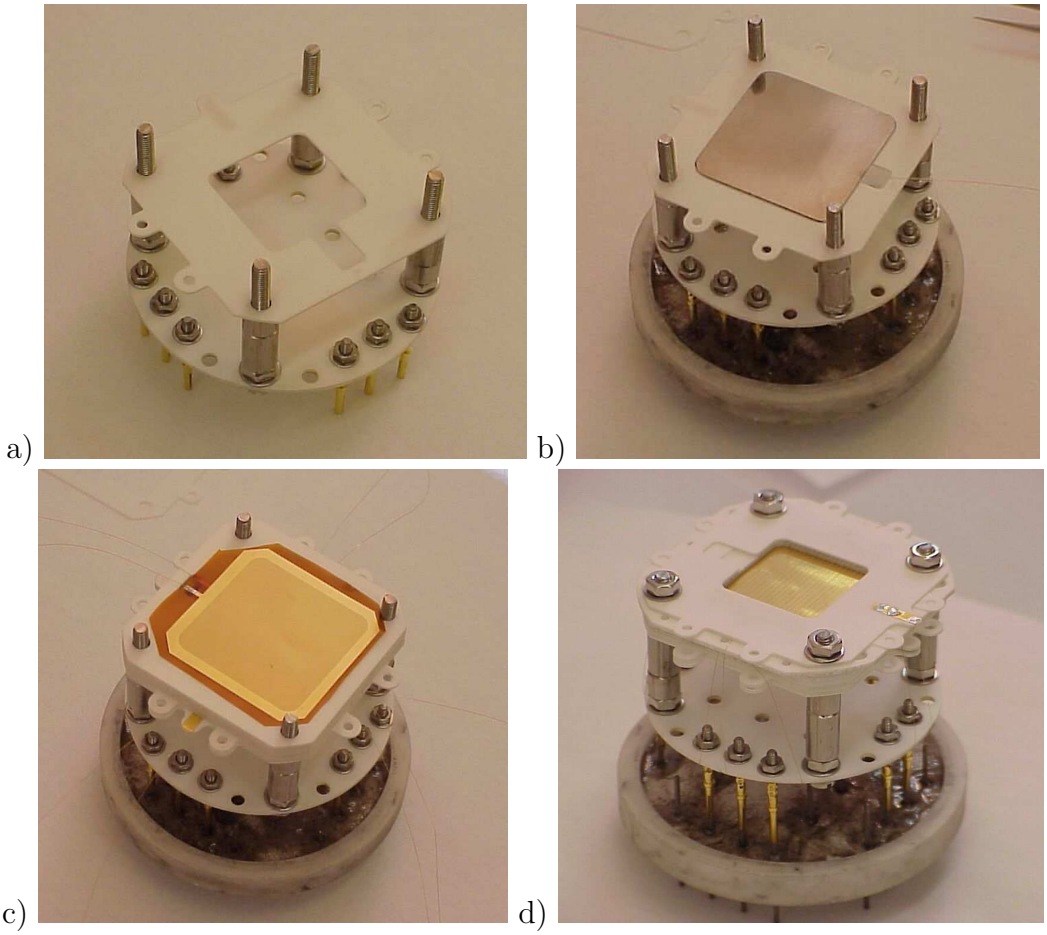

Fig. A.5: a) The first ceramic frame placed on the 4 screws. b) The anode is placed on a ceramic frame and c) GEM foils are added. d) The finished assembly of the electron multiplier.

B. SEALING OF GPMS

Sealed GPMs are prepared by sealing an electron multiplier inside a detector package to a photocathode on a glass substrate using the hot-sealing technique. To achieve a leak-free sealing, various combinations of sealing solders, metal coatings on the sealing surfaces and sealing procedures were systematically investigated. Moreover, the photocathode's QE can degrade during the sealing process, depending on the sealing temperature and duration [122]. The best results were achieved with Ni-coated packages sealed at ∼120°C to copper-coated photocathode substrate windows. A detailed description of the materials and methods of sealing visible-sensitive GPMs is provided below.

B.1 Solder preparation in the detector package

For sealing we use In/Bi eutectic solder (66.3:33.7, melting point 72°C), which replaced the previously used In/Sn solder (52:48, melting point 118°C). In/Bi wire, 1 mm in diameter, is cleaned first with acetone followed by a one minute bath in 10% HCl; it is subsequently rinsed in flowing double deionized water and blown dry with N_2. Four rings of cleaned wire are placed in the groove of the Ni-plated package. New packages are reduced and the wire rings in the groove are melted in a hydrogen oven at 600 °C for 15 minutes. The high-temperature baking in hydrogen atmosphere ensures a good bonding of the In/Bi-solder to the Ni coating of the package. Packages can be reused by removing old In/Bi solder with a desoldering iron and placing new wire in the package groove. As a good bonding between the In/Bi solder and the package's Ni coating already exists, it is sufficient to melt and out-gas the wire in the load-lock chamber of the bi-alkali setup (see Sec. 3.1.2) at approximately 200°C and a vacuum of 10^{-8} torr.

The previously used Au-coating of packages and photocathode substrates did not provide satisfactory sealing results and was therefore abandoned: the thin gold layer formed a brittle intermetalic compound with the Indium, resulting in micro-leaks.

The correct amount of solder in the package groove is critical for the a successful sealing: while an excess of solder can spill and damage the detector elements, an insufficient amount does not allow for a leak-free sealing. For this reason and to remove surface pollutants, the In/Bi solder in the package groove is machined with a lathe, leaving only an excess of 0.25 mm in height and from the package sides (see Fig. B.1). To prevent oxidization of the freshly machined solder surface, its exposure to ambient air should be minimal. Therefore, the electron multiplier is assembled inside the package already before machining, and it is placed into the package holder of the sealing chamber of the bi-alkali setup (see Sec. 3.1.4) immediately after the machining. The package in the holder is carefully adjusted to a level position to avoid spills of the hot In/Bi solder during bake-out and sealing. The holder, containing the package, is attached to a manipulator that allows to rotate the package

during sealing; the holder also establishes electrical contact to the top GEM electrodes and the getter. The chamber is subsequently pumped and the package baked for 2 days at 150°C at a pressure of 10^{-8} torr.

The preparation of photocathode substrate windows to be sealed to the package and the bi-alkali photocathode fabrication procedure is described in detail in Sec. 3.2.

B.2 Sealing procedure

Both, the sealing chamber containing the detector package and the activation chamber with the K–Cs–Sb photocathode are heated to 150°C, sufficient for melting the In/Bi solder in the package groove. The getter inside the detector package is activated by resistive heating to 450°C for 10 minutes before the gate valves to the turbo-molecular pumps of both chambers are closed. The gate valve separating the sealing and activation chambers is opened and the chambers are filled with a Ar and CH_4 gas mixture; the gases are introduced through a GateKeeper 35K filters from Aeronex Inc, purifying noble gases and CH_4 to the 1 ppb level.

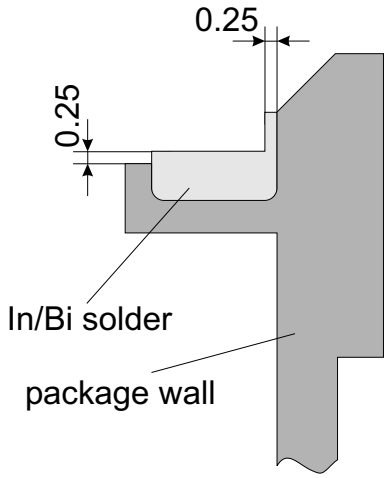

Fig. B.1: The package groove with the melted and machined In/Bi solder. An excess of 0.25 mm remains after machining.

a)  b) 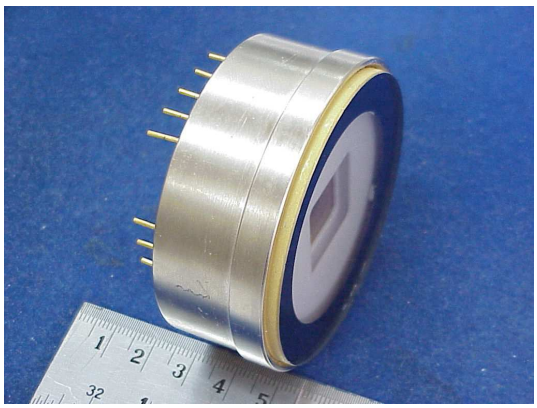

Fig. B.2: A multi-GEM GPM with semi-transparent K–Cs–Sb photocathode sealed in the type A package.

Mass flow controllers allow to control the mixture ratio and limit the flow rate to 1 slm, the recommended maximum flow through the filter. The gas flow is stopped, when a pressure of 740 torr is reached, during the gas filling the temperature drops to 125–120°C. At this point, the photocathode that was retained in the activation chamber during gas filling, is transferred to the sealing chamber. With a vertical manipulator it is slowly lowered onto the package. To ensure a good bonding of the In/Bi solder with the window metalization and to break a superficial oxide layer, the package is rotated slightly a few times before the heating is switched off. After cooling down to room temperature, a pressure of 680–700 torr is typically measured inside the chamber, and the sealed GPM can be extracted. Fig. B.2 shows photographs of the sealed GPMs.

B.3 Sealing results

For verification of the sealing quality and for optimization of the sealing procedure, we repeatedly sealed photocathode substrates to "fake" packages: these do not contain an electron multiplier and instead of feedthrough pins they have a tube outlet for connection of a leak detector. With the sealing procedure described above, we consistingly sealed packages with leak rates below the detection threshold of the He leak detector of $5 \cdot 10^{-12}$ mbar l/s.

Imperfectly sealed packages have their photocathode decaying relatively quickly, while well sealed photocathodes retain their QE for extended periods of time. This is demonstrated in Fig. B.3 for a gaseous photodiode with a K–Cs–Sb photocathode sealed in 680 torr of pure Ar: it was monitored for more than half a year and no deterioration of its QE was observed. The low QE values are due to a high photoelectron backscattering in pure Ar (see Fig. 2.7) and sealing temperatures exceeding 150°C(with In/Sn solder), permanently damaging the photocathode surface. The best QE of a sealed K–Cs–Sb photocathode was measured with a GPM consisting of 2 GEMs and a stainless steel anode (Fig. B.4) sealed in 700 torr of Ar/CH_4 (95:5): it peaks at 400 nm with a QE of 13%. Unfortunately, ion feedback limited the operation of this GPM to a gain of $\sim 10^3$.

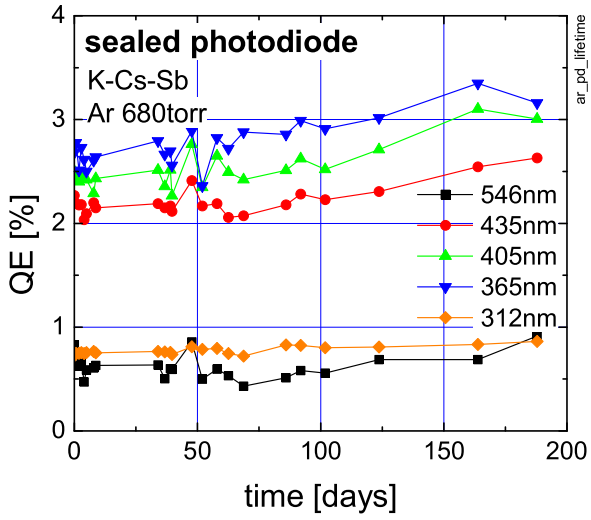

Fig. B.3: Stability in time of the QE of a gaseous photodiode with K–Cs–Sb photocathode, sealed in 680 torr of Ar.

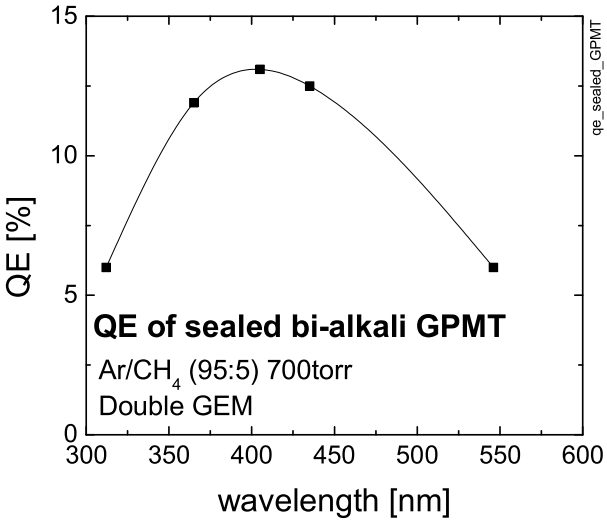

Fig. B.4: QE of a sealed double-GEM GPM with a K–Cs–Sb photocathode.

BIBLIOGRAPHY

[1] "www-sk.icrr.u-tokyo.ac.jp/doc/sk/."

[2] J. Va'vra, "Photon detectors," *Nucl. Instr. and Meth. A*, vol. 371, p. 33, 1996.

[3] J. Va'vra *et al.*, "Study of CsI photocathodes: volume resistivity and aging," *Nucl. Instr. and Meth. A*, vol. 387, p. 154, 1997.

[4] F. Sauli, "GEM: A new concept for electron amplification in gas detectors," *Nucl. Instr. and Meth. A*, vol. 386, p. 531, 1997.

[5] W. Spicer *et al.*, "Modern theory and applications of photocathodes," *SLAC-PUB-6306*, 1993. presented at SPIE's 1993 International Symposium on Optics, Imaging and Instrumentation, San Diego, CA.

[6] A. Sommer, *Photoemissive materials*. Robert E. Krieger Publishing, New York, 1980.

[7] R. Engstrom, *RCA Photomultiplier Handbook*. RCA Corporation, USA, 1980.

[8] M. Cardona and L. Ley, eds., *Photoemission in Solids I*. Springer Verlag, Berlin, Heidelberg, New York, 1978.

[9] K. Arisaka, "New trends in vacuum-based photon detectors," *Nucl. Instr. and Meth. A*, vol. 442, p. 80, 2000.

[10] A. Boutboul *et al.*, "Escape length of UV-induced photoelectrons in alkali iodide and CsBr evaporated films," *J. Appl. Phys.*, vol. 84, p. 2890, 1998.

[11] A. Boutboul *et al.*, "An improved model for UV- and X-ray-induced electron emission from CsI," *J. Appl. Phys.*, vol. 86, p. 5841, 1999.

[12] G. Knoll, *Radiation detection and measurement*. New York: John Wiley & Sons, 2nd ed., 1989.

[13] S. M. Bradbury *et al.*, "Test of the new hybrid INTEVAC intensified photocell for the use in air Cherenkov telescopes," *Nucl. Instr. and Meth. A*, vol. 387, p. 45, 1997.

[14] R. Mirzoyan *et al.*, "An evaluation of the new compact hybrid photodiodes R7110U-07/40 from Hamamatsu in high-speed light detection mode," *Nucl. Instr. and Meth. A*, vol. 442, p. 140, 2000.

[15] D. G. Fisher *et al.*, "Negative electron affinity materials for imaging devices," *Advances in Image Pickup and Display*, vol. 1, p. 71, 1974.

[16] A. Bett *et al.*, "III-V compounds for solar cell applications," *Appl. Phys. A*, vol. 69, p. 119, 1999.

[17] A. Breskin, "CsI UV photocathodes: history and mystery," *Nucl. Instr. and Meth. A*, vol. 371, p. 116, 1996.

[18] J. Almeida *et al.*, "Microanalysis surface studies and photoemission properties of CsI photocathodes," *Nucl. Instr. and Meth. A*, vol. 367, p. 337, 1995.

[19] F. Piuz, "CsI-photocathode and RICH detector," *Nucl. Instr. and Meth. A*, vol. 371, p. 96, 1996.

[20] F. Piuz *et al.*, "Final tests of the CsI-based ring imaging detector for the ALICE experiment," *Nucl. Instr. and Meth. A*, vol. 433, p. 178, 1999.

[21] E. Nappi, "Trends in the development of large area photon detectors for Cherenkov light imaging applications," *Nucl. Instr. and Meth. A*, vol. 504, p. 70, 2003.

[22] A. Braem *et al.*, "Development, fabrication and test of a highly segmented hybrid photodiode," *Nucl. Instr. and Meth. A*, vol. 478, p. 400, 2002.

[23] E. Shefer *et al.*, "Laboratory production of efficient alkali-antimonide photocathodes," *Nucl. Instr. and Meth. A*, vol. 411, p. 383, 1998.

[24] A. Braem *et al.*, "Highly segmented large-area hybrid photodiodes with bialkali photocathodes and enclosed VLSI readout electronics," *Nucl. Instr. and Meth. A*, vol. 442, p. 128, 2000.

[25] E. Shefer *et al.*, "Coated photocathodes for visible photon imaging with gaseous photomultipliers," *Nucl. Instr. and Meth. A*, vol. 433, p. 502, 1999.

[26] A. Buzulutskov *et al.*, "Protection of cesium-antimony photocathodes," *Nucl. Instr. and Meth. A*, vol. 387, p. 176, 1997.

[27] G. Charpak *et al.*, "The gas photodiode as a possible large-area photon detector," *IEEE Trans. Nucl. Sci.*, vol. 30, p. 134, 1983.

[28] J. Edmends *et al.*, "Investigation of prototype gas-filled photomultipliers," *Nucl. Instr. and Meth. A*, vol. 273, p. 145, 1988.

[29] V. Peskov *et al.*, "Cs based photocathodes for gaseous detectors," *Nucl. Instr. and Meth. A*, vol. 348, p. 269, 1994.

[30] A. Breskin *et al.*, "Evidence for thin-film protection of visible photocathodes," *Appl. Phys. Lett.*, vol. 69, p. 1008, 1996.

[31] A. Buzulutskov *et al.*, "The protection of K-Cs-Sb photocathodes with CsBr films," *Nucl. Instr. and Meth. A*, vol. 400, p. 173, 1997.

[32] E. Shefer *et al.*, "Composite photocathodes for visible photon imaging with gaseous photomultipliers," *Nucl. Instr. and Meth. A*, vol. 419, p. 612, 1998.

[33] E. Shefer, *Study of novel stable photocathode materials for gaseous photon detectors in the near-UV to visible spectral range.* PhD thesis, Feinberg Graduate School of the Weizmann Institute of Science, 2000.

[34] Y. Kubota *et al.*, "The CLEO II detector," *Nucl. Instr. and Meth. A*, vol. 320, p. 66, 1992.

[35] BaBar collaboration, "BaBar Technical Design Report,"

[36] "www.theta-systems.com."

[37] J. Pansart, "Avalanche photodiodes for particle detection," *Nucl. Instr. and Meth. A*, vol. 387, p. 186, 1997.

[38] J. Bähr *et al.*, "Investigation of silicon avalanche photodiodes for use in scintillating fiber trackers," *Nucl. Instr. and Meth. A*, vol. 442, p. 203, 2000.

[39] E. Lorenz *et al.*, "Test of a scintillating fibre readout with avalanche photodiodes," *Nucl. Instr. and Meth. A*, vol. 504, p. 154, 2003.

[40] D. Bailleux *et al.*, "Hamamatsu APD for CMS ECAL: quality insurance," *Nucl. Instr. and Meth. A*, vol. 518, p. 622, 2004.

[41] M. Moszyński *et al.*, "Large area avalanche photodiodes in scintillation and X-ray detection," *Nucl. Instr. and Meth. A*, vol. 485, p. 5048, 2002.

[42] A. Mykulyak *et al.*, "Readout of plastic scintillators with cooled large-area avalanche photodiodes," *Nucl. Instr. and Meth. A*, vol. 523, p. 425, 2004.

[43] M. Kapusta *et al.*, "Hamamatsu S8550 APD arrays for high-resolution scintillator matrices readout," *Nucl. Instr. and Meth. A*, vol. 504, p. 139, 2003.

[44] B. Pichler *et al.*, "Studies with a prototype high resolution PET scanner based on LSO-APD modules," *IEEE Trans. Nucl. Sci.*, vol. 45, p. 1298, 1999.

[45] M. Petroff *et al.*, "High energy particle tracking using scintillating fibers and solid state photomultipliers," *IEEE Trans. Nucl. Sci.*, vol. 36, p. 163, 1989.

[46] M. Petroff *et al.*, "Photon-counting solid-state photomultiplier," *IEEE Trans. Nucl. Sci.*, vol. 36, p. 158, 1989.

[47] M. Wayne *et al.*, "Visible light photon counters and the DΦ scintillating fiber tracker," *Nucl. Instr. and Meth. A*, vol. 387, p. 278, 1997.

[48] M. Petroff *et al.*, "Detection of individual 0.4-28μm wavelength photons via impurity-impact," *Appl. Phys. Lett.*, vol. 51, p. 406, 1987.

[49] DΦ collaboration, "DΦ Fibre Tracker Technical Design Report,"

[50] P. Buzhan *et al.*, "An advanced study of silicon photomultiplier," Proceedings of the international conference "Advanced Technology and Particle Physics", (Como, Italy), October 2001.

[51] P. Buzhan *et al.*, "Silicon photomultiplier and its possible applications," *Nucl. Instr. and Meth. A*, vol. 504, p. 48, 2003.

[52] T. Iijima *et al.*, "Aerogel Cherenkov counter for the BELLE experiment," *Nucl. Instr. and Meth. A*, vol. 379, p. 457, 1996.

[53] "www.burle.com."

[54] P. Hink *et al.*, "Characterization of 18mm round and 50mm square MCP-PMTs." Presentation at the 3rd Beaune Conference on New Developments in Photodetection, june 18, 2002.

[55] R. D. Salvo *et al.*, "First results on the hybrid photodiode tube," *Nucl. Instr. and Meth. A*, vol. 315, p. 375, 1992.

[56] N. Kanaya *et al.*, "Test results on hybrid photodiodes," *Nucl. Instr. and Meth. A*, vol. 421, p. 512, 1999.

[57] C. Damiani *et al.*, "Magnetic field effects on Hybrid PhotoDiode single electron response," *Nucl. Instr. and Meth. A*, vol. 442, p. 136, 2000.

[58] A. Braem *et al.*, "Development of a 10-inch HPD with integrated readout electronics," *Nucl. Instr. and Meth. A*, vol. 504, p. 19, 2003.

[59] F. Sauli, "Principles of operation of multiwire proportional and drift chambers." CERN, yellow report 77-09, 1977.

[60] F. Sauli, "Gas detectors: Achievements and trends," *Nucl. Instr. and Meth. A*, vol. 461, p. 47, 2001.

[61] J. Seguinot *et al.*, "A historical survey of ring imaging Cherenkov counters," *Nucl. Instr. and Meth. A*, vol. 343, p. 1, 1996.

[62] A. Breskin *et al.*, "Field-dependent photoelectron extraction from CsI in different gases," *Nucl. Instr. and Meth. A*, vol. 367, p. 342, 1995.

[63] A. Di Mauro *et al.*, "Photoelectron backscattering effects in photoemission from CsI into gas media," *Nucl. Instr. and Meth. A*, vol. 371, p. 137, 1996.

[64] T. Dias *et al.*, "The transmission of photoelectrons emittet from CsI photocathodes into Xe, Ar, Ne and their mixtures: a Monte-Carlo study of the dependence on E/N and incident VUV photon energy," *J. Phys. D: Appl. Phys*, vol. 37, p. 540, 2004.

[65] A. Breskin *et al.*, "GEM photomultiplier operation in CF_4," *Nucl. Instr. and Meth. A*, vol. 483, p. 670, 2002.

[66] B. K. Singh *et al.*, "CsBr and CsI UV photocathodes: new results on quantum efficiency and aging," *Nucl. Instr. and Meth. A*, vol. 454, p. 364, 2000.

[67] A. Breskin *et al.*, "Sealed GEM photomultiplier with a CsI photocathode: ion feedback and ageing," *Nucl. Instr. and Meth. A*, vol. 478, p. 225, 2002.

[68] H. Raether, *Electron avalanches and breakdown in gases.* Butterworths, London, 1964.

[69] G. Charpak *et al.*, "The use of mutiwire proportional counters to select and localize charged particles," *Nucl. Instr. and Meth.*, vol. 62, p. 262, 1968.

[70] M. Artuso, "The ring imaging detector for CLEO III," *Nucl. Instr. and Meth. A*, vol. 371, p. 324, 1996.

[71] "ALICE: Technical design report of the high momentum particle identification detector." CERN/LHCC 98-19.

[72] F. Piuz, "Ring Imaging CHerenkov systems based on gaseous photo-detectors: trends and limits around particle accelerators," *Nucl. Instr. and Meth. A*, vol. 502, p. 76, 2003.

[73] Y. Giomataris *et al.*, "MICROMEGAS: a high-granularity position-sensitive gaseous detector for high particle-flux environments," *Nucl. Instr. and Meth. A*, vol. 376, p. 29, 1996.

[74] J. Derré *et al.*, "Fast signals and single electron detection with a MICROMEGAS photodetector," *Nucl. Instr. and Meth. A*, vol. 449, p. 314, 2000.

[75] J. Derré *et al.*, "Recent experimental results with MICROMEGAS," *Nucl. Instr. and Meth. A*, vol. 477, p. 23, 2002.

[76] A. Delbart *et al.*, "New developments of Micromegas detector," *Nucl. Instr. and Meth. A*, vol. 461, p. 84, 2001.

[77] A. Oed, "Position-sensitive detector with microstrip anode for electron multiplication with gases," *Nucl. Instr. and Meth. A*, vol. 263, p. 351, 1988.

[78] R. Bellazzini *et al.*, "The micro-groove detector," *Nucl. Instr. and Meth. A*, vol. 424, p. 444, 1999.

[79] A. Bressan *et al.*, "High rate behaviour and discharge limits in micro-pattern detectors," *Nucl. Instr. and Meth. A*, vol. 424, p. 321, 1998.

[80] M. Ageron *et al.*, "Experimental and simulation study of the behaviour and operation modes of MSGC+GEM detectors," *Nucl. Instr. and Meth. A*, vol. 489, p. 121, 2002.

[81] W. Gradl, "The inner tracker of HERA-B experiment," *Nucl. Instr. and Meth. A*, vol. 461, p. 80, 2001.

[82] R. Bellazzini *et al.*, "A two-stage, high gain micro-strip detector," *Nucl. Instr. and Meth. A*, vol. 425, p. 218, 1999.

[83] J. Benlloch *et al.*, "Further developments and beam tests of the gas electron multiplier (GEM)," *Nucl. Instr. and Meth. A*, vol. 419, p. 410, 1998.

[84] S. Bachmann *et al.*, "Charge amplification and transfer processes in the gas electron multiplier," *Nucl. Instr. and Meth. A*, vol. 438, p. 376, 1999.

[85] W. Pitts *et al.*, "Experience with laser microfabricated detectors at the University of Louisville," *Nucl. Instr. and Meth. A*, vol. 471, p. 268, 2001.

[86] H. Kim *et al.*, "Application of the LIGA process for fabrication of gas avalanche devices," *IEEE Trans. Nucl. Sci.*, vol. 47, p. 923, 2000.

[87] S. K. Ahn *et al.*, "GEM-type detectors using LIGA and etchable glass technologies," *IEEE Trans. Nucl. Sci.*, vol. 49, no. 3, p. 870, 2002.

[88] R. Chechik *et al.*, "Thick GEM-like hole multipliers: properties and possible applications," *Nucl. Instr. and Meth. A*, vol. 535, p. 303, 2004.

[89] R. Chechik *et al.*, "Thick GEM-like multipliers – a simple solution for large area UV-RICH detectors," *to be published in Nucl. Instr. and Methods A*, 2004. Presented at the RICH 04 workshop, Mexico, Dec. 2004.

[90] V. Peskov *et al.*, "Advances in capillary-based gaseous UV detectors," *to be published in Nucl. Instr. and Methods A*, 2004.

[91] C. Shalem *et al.*, "Advances in Thick GEM-like electron multipliers, part I: atmospheric pressure," *to be submitted to Nucl. Instr. and Meth. A*, 2005.

[92] C. Shalem *et al.*, "Advances in Thick GEM-like electron multipliers, part I: low pressure," *to be submitted to Nucl. Instr. and Meth. A*, 2005.

[93] C. Richter *et al.*, "Absolute electron transfer efficiency of GEM," *Nucl. Instr. and Meth. A*, vol. 461, p. 38, 2001.

[94] C. Richter *et al.*, "On the efficient electron transfer through GEM," *Nucl. Instr. and Meth. A*, vol. 478, p. 538, 2002.

[95] A. Sharma, "3D simulation of charge transfer in a gas electron multiplier (GEM) and comparison to experiment," *Nucl. Instr. and Meth. A*, vol. 454, p. 267, 2000.

[96] G. Guedes *et al.*, "Effects of the induction-gap parameters on the signal in a double-GEM detector," *Nucl. Instr. and Meth. A*, vol. 497, p. 305, 2003.

[97] A. Kozlov *et al.*, "Development of a triple GEM UV-detector operated in pure CF_4 for the PHENIX experiment," *physics/0309013*, 2003.

[98] S. Bachmann *et al.*, "Discharge studies and prevention in the gas electron multiplier (GEM)," *Nucl. Instr. and Meth. A*, vol. 479, p. 294, 2002.

[99] A. Bondar *et al.*, "Study of ion feedback in multi-GEM structures," *Nucl. Instr. and Meth. A*, vol. 496, p. 325, 2003.

[100] A. Bouclier *et al.*, "New observations with the Gas Electron Multiplier (GEM)," *Nucl. Instr. and Meth. A*, vol. 396, p. 50, 1997.

[101] A. Bressan *et al.*, "Beam tests of the gas electron multiplier," *Nucl. Instr. and Meth. A*, vol. 425, p. 262, 1999.

[102] A. Bressan *et al.*, "Two-dimensional readout of GEM detectors," *Nucl. Instr. and Meth. A*, vol. 425, p. 254, 1999.

[103] G. Guedes *et al.*, "Two-dimensional GEM imaging detector with delay-line readout," *Nucl. Instr. and Meth. A*, vol. 513, p. 473, 2003.

[104] C. Altunbas *et al.*, "Construction test and comissioning of the Tripple-GEM tracking detector for COMPASS," *Nucl. Instr. and Meth. A*, vol. 490, p. 177, 2002.

[105] F. Fraga *et al.*, "CCD readout of GEM-based neutron detectors," *Nucl. Instr. and Meth. A*, vol. 478, p. 357, 2002.

[106] V. Dangendorf *et al.*, "Development of a fast-neutron imaging detector with triple-GEM readout." in preparation, 2004.

[107] T. Behnke *et al.*, "A detector for TESLA," *TESLA technical design report, part IV*, 2001.

[108] S. Kappler *et al.*, "A GEM-TPC prototype with low-noise highly integrated front-end electronics for linear collider studies," *to be published in IEEE Trans. Nucl. Sci.*, 2003.

[109] D. Pacella *et al.*, "Ultrafast soft x-ray two-dimensional plasma imaging system based on the Gas Electron Multiplier detector with pixel readout," *Rev. Scient. Instrum.*, vol. 72, p. 1372, 2001.

[110] S. Bachmann *et al.*, "High rate x-ray imaging using multi-GEM detectors with a novel readout design," *Nucl. Instr. and Meth. A*, vol. 478, p. 104, 2002.

[111] A. Brahme *et al.*, "Evaluation of a GEM and CAT-based detector for radiation therapy beam monitoring," *Nucl. Instr. and Meth. A*, vol. 454, p. 136, 2000.

[112] A. Buzulutskov *et al.*, "Further studies of the GEM photomultiplier," *Nucl. Instr. and Meth. A*, vol. 442, p. 68, 2000.

[113] D. Mörmann *et al.*, "Operation principles and properties of the muli-GEM gaseous photomultiplier with reflective photocathode.," *Nucl. Instr. and Meth. A*, vol. 530, p. 258, 2004.

[114] A. Buzulutskov *et al.*, "GEM operation in pure noble gases and the avalanche confinement," *Nucl. Instr. and Meth. A*, vol. 433, p. 471, 1999.

[115] A. Bondar *et al.*, "High pressure operation of the triple-GEM detector in pure Ne, Ar and Xe," *Nucl. Instr. and Meth. A*, vol. 481, p. 200, 2002.

[116] R. Chechik *et al.*, "Progress in GEM-based gaseous photomultipliers," *Nucl. Instr. and Meth. A*, vol. 502, p. 195, 2003.

[117] J. Veloso *et al.*, "A proposed new microstructure for gas radiation detectors: the microhole and strip plate," *Rev. Sci. Instr.*, vol. 71, no. 6, p. 2371, 2000.

[118] J. M. Maia *et al.*, "Advances in the Micro Hole & Strip Plate gaseous detector," *Nucl. Instr. and Meth. A*, vol. 504, p. 364, 2003.

[119] J. Maia *et al.*, "Progress in MHSP electron multiplier operation," *to be published in IEEE Trans. Nucl. Sci.*, 2003.

[120] J. M. Maia *et al.*, "Avalanche-ion back-flow reduction in gaseous GEM/MHSP electron multipliers," *to be published in Nucl. Instr. and Methods A*, 2003.

[121] J. Veloso *et al.*, "MHSP reverse-mode operation for ion blocking in gas-avalanche multipliers," in preparation.

[122] M. Balcerzyk *et al.*, "Methods of preparation and performance of sealed gas photomultipliers for visible light," *IEEE Trans. Nucl. Sci.*, vol. 50, no. 4, p. 847, 2003.

[123] A. Braem *et al.*, "Technology of photocathode production," *Nucl. Instr. and Meth. A*, vol. 502, p. 205, 2003.

[124] A. Buzulutskov *et al.*, "The GEM photomultiplier operated with noble gas mixtures," *Nucl. Instr. and Meth. A*, vol. 443, p. 164, 2000.

[125] *MAXWELL 3D, commercial finite element computation package, ANSOFT, Anaheim, USA.*

[126] R. Veenhof, "Garfield, recent developments," *Nucl. Instr. and Meth. A*, vol. 419, p. 726, 1998.

[127] F. Sauli *et al.*, "Electron collection and ion feedback in GEM-based detectors," *IEEE Trans. Nucl. Sci.*, vol. 50, p. 803, 2003.

[128] A. Bouclier *et al.*, "The Gas Electron Multiplier (GEM)," *IEEE Trans. Nucl. Sci.*, vol. 44, no. 3, p. 646, 1997.

[129] J. Lopes *et al.*, "A new integrated photosensor for gas proportional scintillation counters based on the gas electron multiplier," *Nucl. Instr. and Meth. A*, vol. 426, p. 469, 1999.

[130] A. Breskin *et al.*, "Recent advances in gaseous imaging photomultipliers," *Nucl. Instr. and Meth. A*, vol. 513, p. 250, 2003.

[131] A. Peisert and F. Sauli, "Drift and diffusion of electrons in gases: a compilation." CERN, yellow report 84-08, 1984.

[132] Z. Fraenkel *et al.*, "A hadron blind detector for PHENIX experiment at RHIC," *to be published in Nucl. Instr. and Methods A*, 2005. physics/0502008.

[133] "Hamamatsu PMT handbook." http://www.hamamatsu.com.

[134] D. Mörmann *et al.*, "Evaluation and reduction of ion-backflow in multi-GEM detectors," *Nucl. Instr. and Meth. A*, vol. 516, p. 315, 2004.

[135] M. Kaminsky, *Atomic and ionic impact phenomena on metal surfaces.* Springer Verlag, 1965.

[136] O. Allkofer, *Spark chambers.* Thiemig, München, 1969.

[137] R. Weast, ed., *Handbook of Chemistry and Physics.* CRC-Press, Cleveland, Ohio, 53rd ed., 1973.

[138] E. Shefer *et al.*, "Photoelectron transport in CsI and CsBr coating films of alkali antimonide and CsI photocathodes," *J. Appl. Phys.*, vol. 92, p. 4758, 2002.

[139] V. Biteman *et al.*, "Position senstive gaseous photomultipliers," *Nucl. Instr. and Meth. A*, vol. 471, p. 205, 2001.

[140] F. Sauli, ed., *Instrumentation in high energy physics*, vol. 9. World Scientific, Singapore, 1992.

[141] O. Bunemann *et al.*, "Design of grid ionization chambers," *Can. J. of Res.*, vol. 27A, p. 191, 1949.

[142] J. Edmends *et al.*, "Studies of a gas-filled ultraviolet detector with a semitransparent photocathode," *Nucl. Instr. and Meth. A*, vol. 258, p. 185, 1988.

[143] O. Bouianov, "The ion trap: a new approach to gaseous microstructure detectors," *Nucl. Instr. and Meth. A*, vol. 526, p. 413, 2004.

[144] S. Roth, "Charge transfer of GEM structures in high magnetic fields," *to be published in Nucl. Instr. and Methods A*, 2004.

[145] J. Veloso *et al.*, "Recent advances in x-ray detetion with micro-file and strip plate detector," *to be published in Nucl. Instr. and Methods A*, 2004.

[146] A. V. Lyashenko *et al.*, "Ion back-flow reduction in multi-MHSP/GEM structures," in preparation.

[147] A. Breskin *et al.*, "High flux operation of the gated multistep avalanche chamber," *Nucl. Instr. and Meth.*, vol. 178, p. 11, 1980.

[148] P. Némethy *et al.*, "Gated time projection chamber," *Nucl. Instr. and Meth. A*, vol. 212, p. 273, 1983.

[149] "ALICE: technical design report: http://alice.web.cern.ch/Alice/TDR/."

[150] G. Garty *et al.*, "Single photoelectron detection with a low-pressure gas electron multiplier coupled to a csi photocathode," *Nucl. Instr. and Meth. A*, vol. 433, p. 476, 1999.

[151] S. Bachmann *et al.*, "Development and applications of the gas electron multiplier," *Nucl. Instr. and Meth. A*, vol. 471, p. 115, 2001.

[152] T. Barvich *et al.*, "Construction and performance of a micro-pattern stereo detector with two gas electron multipliers," *Nucl. Instr. and Meth. A*, vol. 458, p. 477, 2002.

[153] O. H. W. Siegmund *et al.*, "Application of the wedge and strip anode to position sensing with microchannel plates and proportional counters," *IEEE Trans. Nucl. Sci.*, vol. 30, no. 1, p. 503, 1983.

[154] O. Siegmund *et al.*, "Operational characteristics of wedge and strip image readout systems," *IEEE Trans. Nucl. Sci.*, vol. 33, no. 1, p. 724, 1986.

[155] A. Smith *et al.*, "Modulation effects in wedge and strip anodes," *Rev. Sci. Instrum.*, vol. 60, no. 11, p. 3509, 1989.

[156] O. Jagutzki *et al.*, "Postion sensitive anodes for MCP read-out using induced charge measurement," *Nucl. Instr. and Meth. A*, vol. 477, p. 256, 2002.

[157] G. Battistoni *et al.*, "Resistive cathode transparency," *Nucl. Instr. and Meth.*, vol. 202, p. 459, 1982.

[158] H. Klein *et al.*, "Energy and angle straggling effects in a D(d,n)^{3}He neutron source using a gas target," *Nucl. Instr. and Meth.*, vol. 193, p. 635, 1982.

[159] M. Edgar *et al.*, "Spatial charge cloud distribution of microchannel plates," *Rev. Sci. Instrum.*, vol. 60, no. 12, 1989.

[160] P. Weilhammer, "Front-end electronics for RICH detectors," *Nucl. Instr. and Meth. A*, vol. 433, p. 413, 1999.

[161] A. Breskin *et al.*, "Ion-induced effects in GEM & GEM/MHSP gaseous photomultipliers for the UV and the visible spectral range," *to be published in Nucl. Instr. and Methods A*, 2005. physics/0502132.

LIST OF PUBLICATIONS

On the efficient operation of CsI-coated GEM photon detector
D. Mörmann, A. Breskin, R. Chechik, B.K. Singh
Nucl. Instr. and Meth. A 471 (2001) 333.

On the efficient electron transport through GEM
C. Richter, A. Breskin, R. Chechik, D. Mörmann, G. Garty, A. Sharma
Nucl. Instr. and Meth. A 478 (2002) 528.

A gas avalanche multiplier with CsI-coated GEM
D. Mörmann, A. Breskin, R. Chechik, P. Cwetanski, B.K. Singh
Nucl. Instr. and Meth. A 478 (2002) 230.

Effects of the induction-gap parameters on the signal in a double-GEM detector
G. Guedes, A. Breskin, R. Chechik, D. Mörmann
Nucl. Instr. and Meth. A 497 (2003) 305.

GEM-based gaseous photomultiplier for UV and visible photon imaging
D. Mörmann, M. Balcerzyk, A. Breskin, R. Chechik, B.K. Singh, A. Buzulutskov
Nucl. Instr. and Meth. A 504 (2003) 93.

Advances in the Micro Hole & Strip Plate gaseous detector
J.M. Maia, J.F.C.A. Veloso, J.M.F. Dos Santos, A. Breskin, R. Chechik, D. Mörmann
Nucl. Instr. and Meth. A 504 (2003) 364.

Progress in GEM-based gaseous photomultipliers
R. Chechik, M. Balcerzyk, A. Breskin, A. Buzulutskov, G.P. Guedes, D. Mörmann, B.K. Singh
Nucl. Instr. and Meth. A 502 (2003) 195.

Methods of preparation and performance of sealed gas photomultipliers for visible light
M. Balcerzyk, D. Mörmann, A. Breskin, B.K. Singh, E.D.C. Freitas, R. Chechik, M. Klin, M. Rappaport
IEEE transactions on Nuclear Science, 50/4 (2003) 847.

Avalanche-ion back-flow reduction in gaseous GEM/MHSP electron multipliers
J.M. Maia, D. Mörmann, A. Breskin, R. Chechik, J.F.C.A. Veloso, J.M.F. Dos Santos
Nucl. Instr. and Meth. A in press.

Operation principles and properties of the multi-GEM gaseous photomultiplier with reflective photocathode
D. Mörmann, A. Breskin, R. Chechik, C. Shalem
Nucl. Instr. and Meth. A 530 (2004) 258.

Evaluation and reduction of ion-backflow in multi-GEM detectors
D. Mörmann, A. Breskin, R. Chechik
Nucl. Instr. and Meth. A 516 (2004) 315.

Recent investigations of cascaded GEM and MHSP detectors
R. Chechik, A. Breskin, G. P. Guedes, D. Mörmann, J. Maia, V. Dangendorf, D. Vartzky, J.M.F. Dos Santos, J.F.C.A. Veloso
submitted to IEEE transactions on Nuclear Science (2003).

Progress in MHSP electron multiplier operation
J.M. Maia, D. Mörmann, A. Breskin, R. Chechik, J.F.C.A. Veloso, J.M.F. Dos Santos
submitted to IEEE transactions on Nuclear Science (2003).

Advances in capillary-based gaseous UV imaging detectors
V. Peskov , A. Breskin, R. Chechik, M. Danielsson, C. Iacobaeus, T. Francke, D. Mörmann, J.Ostling
submitted to Nucl. Instr. and Meth. A.

Thick GEM-like hole multipliers: properties and possible applications
R. Chechik, A. Breskin, C. Shalem, D. Mörmann
submitted to Nucl. Instr. and Meth. A.

Ion-induced effects in GEM & GEM/MHSP gaseous photomultipliers for the UV and visible spectral range
A. Breskin, D. Mörmann, A. Lyashenko, R. Chechik, F.D. Amaro, J.M. Maia, J.F.C.A. Veloso, J.M.F. Dos Santos
submitted to Nucl. Instr. and Meth. A.

ACKNOWLEDGEMENTS

The years devoted in working towards the Ph. D. degree in the Radiation Detection Physics group at the Weizmann Institute of Science were a most exciting and enriching time for me both professionally and personally. I wish to express my dearest thanks and gratitude to all those who advised, help and supported me to carry out this work.

First of all, my words of acknowledgement go to my supervisor Prof. Amos Breskin for guiding me and helping in many critical moments of this work. Without his vast knowledge and many fruitful discussions, this work would not have been possible.

To Dr. Rachel Chechik for her significant help, always well-considered advise and many helpful discussions.

To Prof. Eilam Gross and Prof. Dan Shahar for their attention to my work and very useful discussions.

To the Minerva Foundation for supporting with a fellowship during a large part of studies.

To Dr. Marcin Balcerzyk and Dr. B.K. Singh for their dedication and help during the common work on the bi-alkali photocathode fabrication and sealing procedures.

To Moshe Klin, Yehuda Asher for their helpful technical support.

My fellow students and colleagues Alexeji, Carola, Elisabete, Germano, Gili, Guy, Jorge for their kind help and contribution.

Thanks to H. Appelshäuser and D. Vranic for valuable discussions on ion gating and providing me with a high-voltage pulser.

To Oved, Nizan, Daniel and Noga, my friends in Israel for the great time we spent together.

And last but not least to my girl friend Yvonne, who supported me during this sometimes critical time with all her love and patience.